

FEDERAL UNIVERSITY OF BAHIA POLITECHNICAL SCHOOL ELECTRICAL ENGINEERING DEPARTMENT GRADUATE SCHOOL OF ELECTRICAL ENGINEERING

TULIO FREITAS SIMÕES DE CASTRO

ALL-DIELECTRIC METASURFACES FOR ANOMALOUS REFRACTION, REFLECTION AND FOCUSING AT INFRARED FREQUENCIES

Salvador 2019/August

TULIO FREITAS SIMÕES DE CASTRO

ALL-DIELECTRIC METASURFACES FOR ANOMALOUS REFRACTION, REFLECTION AND FOCUSING AT INFRARED FREQUENCIES

Master degree dissertation presented to the Post-studies Program in Electrical Engineering of Federal University Federal of Bahia, as part of the requisites for the obtaining of the Master's degree in Electrical Engineering.

Prof. Dr. Vitaly Felix Rodriguez-Esquerre. **Advisor**

Salvador

2019/August

T917

Freitas Simões de Castro, Tulio

All-dielectric metasurfaces for anomalous refraction, reflection and focusing at infrared frequencies / Tulio Freitas Simões de Castro. -- Salvador, 2019.

XX f. : il

Advisor: Prof. Dr. Vitaly Felix Rodriguez-Esquerre.

Dissertation (Master degree - Postgraduate Sutdies in Electrical Engineering Program) - Federal University of Bahia, Universidade Federal da Bahia - Politechnical School, 2019.

1. All-dielectric metasurfaces. 2. Anomalous refraction. 3. Anomalous Reflection. 4. Metalenses. 5. Infrared frequencies. I. Rodriguez-Esquerre, Prof. Dr. Vitaly Felix. II. Title.

TULIO FREITAS SIMÕES DE CASTRO

ALL-DIELECTRIC METASURFACES FOR ANOMALOUS REFRACTION, REFLECTION AND FOCUSING AT INFRARED FREQUENCIES

Dissertation of Master's degree presented as part of the requisites for obtaining the degree of Master in Electrical Engineering from the course of Graduate School of Electrical Engineering of Federal University of Bahia.

Examination Board:

Prof. Dr. Vitaly Felix Rodriguez-Esquerre - Advisor

UFBA

Prof. Dr. Anderson Dourado-Sisnando UFBA

Prof. Dr. Cosme Eustaquio Rubio-Mercedes

Lburado Sissoundo

UEMS

ACKNOWLEDGEMENTS

To God, for bringing back to me a long lost hunger of accomplishing this work and the wish for more yet to come.

To my parents, specially my mother, the best person I've ever knew, who could bring up the best of me with a healthy, tight shake of reality.

To Luci Licia Bacelar, Paulo Petersen da Silva and Caetano Pinto da Silva Neto, who embraced me as family. To my brother Bruno Freitas Simões de Castro, for his support.

To Prof. Ph. D. Vitaly Felix Rodriguez-Esquerre, whose steps I intend to follow, for advising me and believing that I could accomplish this work.

To Rafael Andrade Vieira, for the friendship and the partnership in our three elaborated scientific works (with more to come!) and shared ideas and efforts that help me to accomplish this work.

To my friends Wellington Alves Santana Junior, André "Salada" Cury Lima and Thompson Nery Hora, for sharing information and discussions that made some good difference in the development of this work. To Iago Borba, to Mozart di Nola Cardoso and his family, for providing support to me whenever I ever solicited.

To the colleagues and teachers I had the chance to meet, mostly at the lab, others from graduation course, but also along the university over these last few years: Davi Franco Rêgo, Luana da França Vieira, Gabriel Couto Pereira Santos, Diego Souza Bezerra, Juarez Caetano da Silva, Luiz Henrique Santos Silva, Anderson Dourado Sisnando, Ícaro Almeida Sampaio, Pedro Paulo Matos Barreto, Miriele Carvalho Paim, Igor Leonardo Gomes de Souza, Davi Araújo de Figueiredo, Emanuela Paranhos Lima, João Victor Galvão da Mata, Joaquim Junior Isídio de Lima, Leonardo Pereira Dias and James Neves da Silva.

To the teachers of the post studies program in electrical engineering of UFBA, whose daily efforts towards high quality education make possible for the students, such as myself, to reach a superior academic degree.

To Jaime Rodrigues Neto and Ágatha Sampaio, whose estimated support, good will and good timing with subjects about the Post-studies Program were very useful and appreciated by me.

To estimated friends who have been supported me during many years: Igor Dantas, Leonardo Leão, Fernando Bacelar, Alan Barreto de Andrade, Pedro Thiago Fonseca Albergaria Dultra, Gerardo Andrés Mendel and Emílio Abreu.

To FAPESB (Fundo de Amparo à Pesquisa na Bahia) for the financial support required in order to develop this work with exclusive dedication.

ABSTRACT

When it comes to the metamaterials field, metasurfaces represent their promising two dimensional ramification. Their simplicity and relative ease of building through the use of traditional techniques like lithography, compared to bulk metamaterials. Metasurfaces represent a sudden variation of optical properties when an incident wave interacts with it. Since its surging, its exploration consisted in utilizing, basically, the plasmonic MIM (metal, insulator, metal) construction. These metasurface have developed feats starting with negative refractive index and now perform electromagnetic skills such as polarization control and wavefront shaping. In order to overcome the inconvenient ohmic losses which are intrinsic to the metal parts of plasmonic metasurfaces, the development of all-dielectric metasurfaces has arisen and gained strength over the last few years. This work proposes three models of alldielectric metasurfaces for different applications within the infrared range of optical communications that work by imposing a phase gradient (successive phase jumps) to the incident to a normally incident wave. The first proposed device is an anomalous refractor: it will be shown a designed refraction for a specifically chosen transmission angle for a normally incident wave. The second proposed device is an anomalous reflector, which will cause an angulated reflection for a normally incident wave. The third proposed device is an all-dielectric metalens, which will have analyzed its capacity of focusing the normally incident wave in a focal plane.

Keywords: All-dielectric metasurfaces; Generalized Snell's law; Phase gradient; Anomalous refractor; Anomalous transmitter; Anomalous reflector; Reflective metasurfaces; Metalens; Wavefront shaping; Focusing; Wave propagation.

SUMMARY

1	INTRODUCTION	22
	MOTIVATION	22
	OBJECTIVES	23
	General	23
	ORGANIZATION OF THIS WORK	24
2	2 LITERATURE REVIEW	26
	2.1 METAMATERIALS: A BRIEF INTRODUCTION	26
	2.2 METASURFACES	29
	2.3 GENERALIZED LAWS OF REFRACTION AND REFLECTION AND ITS	CORRESPONDING
	ANOMALOUS PHENOMENA	30
	2.4 WAVEFRONT SHAPING	33
	2.5 ALL-DIELECTRIC METASURFACES	34
3	3 ANOMALOUS REFRACTOR, ANOMALOUS REFLECTOR	AND METALENS -
D	DEVICES AND RESULTS CONSIDERING IDEALLY STRUCT	TURED MODELS
	36	
	3.1 INTRODUCTION	36
	3.1 INTRODUCTION	
		37
	3.2 Anomalous Refractor	37
4	3.2 Anomalous Refractor	
	3.2 Anomalous Refractor	

CONCLUSIONS AND FUTURE WORKS	118
CONCLUSIONS	118
PURPOSES FOR FUTURE WORKS	119
REFERENCES:	120
APPENDIX	124
APPENDIX A – PUBLICATIONS OF ACADEMIC PAPERS	124
A.1 ACADEMIC PAPERS RELATED TO THE PROJECT	124
A.1.1 PUBLICATION IN INTERNATIONAL CONGRESS	124
APPENDIX	126
APPENDIX B – FERMAT'S PRINCIPLE AND THE CLASSIC LAW	S OF
REFRACTION AND REFLECTION	126
B1 CONSEQUENCE OF FERMAT'S PRINCIPLE WHEN THE LIGHT	Γ IS MOVING
THROUGH THE SAME MEDIA [47]	126
B2 FERMAT'S PRINCIPLE ON THE CLASSIC REFLECTION OF LIG	GHT 128
B3 FERMAT'S PRINCIPLE APPLIED TO THE CLASSIC REFRACTI	ON OF LIGHT
131	

LIST OF FIGURES

Figure 1 - Frequency of references cited about the subject related to a specific year23
Figure $2 - a$) electric and magnetic field with the propagation vector \mathbf{k} as a left handed system
b) refraction of EMW through a double negative metamaterial (from [2])28
Figure 3 – Simplistic comparison of classic and anomalous refraction of normally incident
light. a) Classic approach. b) Metasurface approach, in which it acts as an anomalous
refractor
Figure 4 - Simplistic comparison of classic and anomalous reflection of normally incident
light. a) Classic approach. b) Metasurface approach, in which it acts as an anomalous
reflecting mirror
Figure 5 – Schematic view of the unit cell of the metasurface, with its dimensions and
employed materials. In blue, Si. In gray, Air. Dimensions wa and wb vary from 20 up to
230(nm). $h1 = 300(nm)$, $h2 = 250(nm)$ and $d = 50(nm)$. Incident electrical field is polarized in
x direction. The space among the blocks is filled with air
Figure 6 - Absolute value of the transmission coefficient $ au$ of the electric field mapped for
each pair wa , wb varying from 20 to 230 (nm) of the anomalous refractor39
Figure 7 – Phase of the transmission coefficient for the electric field mapped for each pair
wa , wb varying from 20 to 230 (nm)
Figure 8 - Absolute value and phase of the transmission coefficient with angle steps marked
on the maps41
Figure 9 – supercell of the metasurface, which considered dimensions are angle step $\Gamma = 750$
(nm) and total length of $\Lambda = 3750$ (nm). Material distribution is given by Air, in gray, and Si,
in blue. The space among the structures is filled with air. Incident electric field is polarized in
x direction
Figure 10 - Phase profile of the metasurface through the global range from $-\pi$ to π , as a
function of the position \boldsymbol{x} .
Figure $11 - x$ component of the electric field, in V/m. Operation of the anomalous refractor as
a function of the wavelength, $\lambda 0$, without considering errors within the structure43
Figure 12 - Unit cell of the reflector; air gap between resonators in white, distance denoted by
g; dark blue is for Si fulfilling the inside of the blocks; SiO ₂ is in gray, around the Si; The
ground plane substrate, in pale blue is in Ag; Dimensions of the cell are $p = 250$ nm, $g = 100$

nm. Both wa , wb vary from 20 to 230 nm. The incident electric field is polarized in x
direction
Figura 13 - Distribution of the absolute value of the reflection coefficient of the metasurface
tested for wa and wb varying from 20 to 230 nm
Figure 14 - Phase of the reflection coefficient of the electric field for wa and wb varying from
20 to 230 (nm)
Figura 15 - Absolute value and phase of the transmission coefficient with angle steps marked
on the maps47
Figura 16 - Supercell of the metasurface. $\Gamma = 3p = 750$ nm; $\Lambda = 21p = 5250$ nm; The incident
electric field, in V/m is polarized in x direction
Figure 17 - Phase profile of the anomalous reflector, which depends on the position,
periodically repeated, as for its responsible supercells
Figure 18 - Anomalous reflection of the electric field, x component, performed by the
metasurface for wavelengths ranging from 1.4 to 1.7 μm. Errors within the structure are not
being considered50
Figure 19 - Unit cell of the metalens. Employed materials are Air, in gray, and Si, in blue.
External dimensions are $h1 = 300$ nm, $h2 = 250$ nm and $d = 50$ nm. Internal dimensions wa
and \boldsymbol{wb} are swept from 20 up to 230 nm. Incident electrical field is polarized in x direction.
The space among the blocks is filled with air.
Figure 20 - Mirrored structure of the metalens (half of its structure). composed by Si, in blue,
and air, in gray. Basic dimensions are the angle step $\Gamma=750$ nm. The total length is
$\Lambda = 17250 \text{ nm}55$
Figure 21 – Ideal phase profile of the metalens, in red, approximated by 23 angle steps of 3
unit cells each, in blue.
Figure 22 - Power density of the electric field for the wavelength, in $\ensuremath{W/m^2}$, represented by the
normalized Poynting vector of the EMW, varying around 1550 nm, ranging from 1400 to
1700 nm. The focus of the metalens coincides with its focal plane, that has the following
values: a) 6550 nm; b) 6350 nm; c) 5950 nm; d) 5500 nm; e) 5400 nm; f) 5050 nm; g) 4700
nm
Figure 23 - Influence of varied errors on the anomalous refractor for $\lambda 0 = 1.4 \mu m$
Figure 24 - Analysis of the transmission angle θt as geometry errors are inserted in the
supercell for the wavelength of 1.4 μm
Figure 25 - Influence of varied errors on the anomalous refractor for $\lambda 0 = 1.45$ (um)63

Figure 26 – Analysis of the transmission angle θt as geometry errors are inserted in the
supercell for the wavelength of 1.45 μm .
Figure 27 - Influence of varied errors on the anomalous refractor for $\lambda 0 = 1.5 \ \mu m$
Figure 28 - Analysis of the transmission angle θt as geometry errors are inserted in the
supercell for the wavelength of 1.5 µm.
Figure 29 - Influence of varied errors on the anomalous refractor for $\lambda 0 = 1.55 (\mu m) \dots 67$
Figure 30 - Analysis of the transmission angle θt as geometry errors are inserted in the
supercell for the wavelength of 1.55 μm .
Figure 31 - Influence of varied errors on the anomalous refractor for $\lambda 0 = 1.6 \ \mu m$
Figure 32 - Analysis of the transmission angle θt as geometry errors are inserted in the
supercell for the wavelength of 1.60 µm.
Figure 33 - Influence of varied errors on the anomalous refractor for $\lambda 0 = 1.65~\mu m$ 71
Figure 34 - Analysis of the transmission angle θt as geometry errors are inserted in the
supercell for the wavelength of 1.65 µm.
Figure 35 - Influence of varied errors on the anomalous refractor for $\lambda 0 = 1.7 \mu m$
Figure 36 - Analysis of the transmission angle θt as geometry errors are inserted in the
supercell for the wavelength of 1.7 μm
Figure 37 - Influence of varied errors on the anomalous reflector for $\lambda 0 = 1.4 \ \mu m$ 75
Figure 38 - Analysis of the reflection angle θr as geometry errors are inserted in the supercell
for the wavelength of 1.4 µm
Figure 39 - Influence of varied errors on the anomalous reflector for $\lambda 0 = 1.45~\mu m$ 77
Figure 40 - Analysis of the reflection angle θr as geometry errors are inserted in the supercell
for the wavelength of 1.45 μm .
Figure 41 - Influence of varied errors on the anomalous reflector for $\lambda 0 = 1.5 \ \mu m$
Figure 42 - Analysis of the reflection angle θr as geometry errors are inserted in the supercell
for the wavelength of 1.5 μm .
Figure 43 - Influence of varied errors on the anomalous reflector for $\lambda 0 = 1.55~\mu m$
Figure 44 - Analysis of the reflection angle θr as geometry errors are inserted in the supercell
for the wavelength of 1.55 μm .
Figure 45 - Influence of varied errors on the anomalous reflector for $\lambda 0 = 1.6 \ \mu m.$
Figure 46 - Analysis of the reflection angle θr as geometry errors are inserted in the supercell
for the wavelength of 1.6 μm .
Figure 47 - Influence of varied errors on the anomalous reflector for $\lambda 0 = 1.65 \mu m$

Figure 48 - Analysis of the reflection angle θr as geometry errors are inserted in the supercell
for the wavelength of 1.65 μm .
Figure 49 - Influence of varied errors on the anomalous reflector for $\lambda 0 = 1.7~\mu m.$
Figura 50 - Analysis of the reflection angle $\boldsymbol{\theta r}$ as geometry errors are inserted in the supercell
for the wavelength of 1.7 μm .
Figure 51 - Influence of varied errors on the metalens for $\lambda 0 = 1.4 \ \mu m$. The focal plane
position, y in μ m, and the power density of the wave on it, in MW/m ² , are given in pairs y , S
as it follows: a) 5.7584; 0.61499 b) 5.6029; 0.59454 c) 5.6902; 0.58701 d)
5.6662; 0.5542 e) 5.5132; 0.51946 f) 5.4767; 0.48341 g) 5.5450; 0.46426 h)
5.5544; 0.42149 i) 5.4293; 0.3865690
Figure 52 - Influence of varied errors on the metalens for $\lambda 0 = 1.45 \ \mu m$. The focal plane
position, y in μ m, and the power density of the wave on it, in MW/m ² , are given in pairs y, S
as it follows: a) 5.2210; 0.67091 b) 5.1478; 0.65059 c) 5.6902; 0.58701 d)
5.2235; 0.58396 e) 5.3778; 0.55068 f) 5.2421; 0.51319 g) 5.5450; 0.46425 h)
5.5567; 0.43588 i) 5.5567; 0.43588
Figure 53 - Influence of varied errors on the metalens for $\lambda 0 = 1.5 \mu m$. The focal plane
position, y, in μ m, and the power density of the wave on it, in MW/m ² , are given in pairs y, S
as it follows: a) 4.7872; 0.69280 b) 4.4892; 0.66862 c) 5.0734; 0.69189 d)
4.9592; 0.68257 e) 5.1144; 0.67768 f) 4.9180; 0.66198 g) 5.0850; 0.62426 h)
5.1741; 0.58496 i) 5.0028; 0.5343694
Figure 54 - Influence of varied errors on the metalens for $\lambda 0 = 1.55 \mu m$. The focal plane
position, y , in μ m, and the power density of the wave on it, in MW/m^2 , are given in pairs y , S
as it follows: a) 4.4481; 0.65490 b) 4.4892; 0.62586 c) 4.4456; 0.63027 d)
4.5300; 0.64069 e) 4.3404; 0.65677 f) 4.6256; 0.67154 g) 4.6594; 0.65990 h)
4.7515; 0.64987 i) 4.5630; 0.6300896
Figure 55 - Influence of varied errors on the metalens for $\lambda 0 = 1.6 \ \mu m$. The focal plane
position, y , in μ m, and the power density of the wave on it, in MW/m^2 , are given in pairs y , S
as it follows: a) 4.4481; 0.64565 b) 4.4892; 0.66862 c) 4.4456; 0.70051 d)
4.3196; 0.70344 e) 4.3404; 0.70940 f) 4.5019; 0.68495 g) 4.3267; 0.65145 h)
4.4219; 0.58850 i) 4.5630; 0.5342098
Figure 56 - Influence of varied errors on the metalens for $\lambda 0 = 1.65 \ \mu m$. The focal plane
position, y , in μ m, and the power density of the wave on it, in MW/m^2 , are given in pairs y , S
as it follows: a) 4.1191; 0.51865 b) 4.0648; 0.52657 c) 4.1253; 0.54076 d)

3.9957; 0.55116 e) 4.0245; 0.57932 f) 4.1857; 0.61725 g) 4.0018; 0.66539 h)
3.9871; 0.71970 i) 4.1187; 0.75978100
Figure 57 - Influence of varied errors on the metalens for $\lambda 0 = 1.7 \mu m$. The focal plane
position, y, in μ m, and the power density of the wave on it, in MW/m ² , are given in pairs y, S
as it follows: a) 3.6582; 0.51538 b) 3.7319; 0.53078 c) 3.7972; 0.56162 d)
3.6728; 0.56162 e) 3.7135; 0.56839 f) 3.7239; 0.57956 g) 3.5647; 0.58527 h)
3.6523; 0.58430 i) 3.6617; 0.59465102
Figure 58 - Influence of varied errors on the metalens for $\lambda 0 = 1.4 \mu m$. The focal plane
position, y in μ m, and the square electric field of the wave on it, in MV^2/m^2 , are given in pairs
y, E2 as it follows: a) 5.7584; 401.2516 b) 5.6029; 389.6459 c) 5.6902; 353.8914 d)
5.6662; 365.0699 e) 5.5132; 340.6452 f) 5.4767; 315.3953 g) 5.5450; 302.6883 h)
5.5544; 276.6490 i) 5.4293; 250.3519104
Figure 59 - Influence of varied errors on the metalens for $\lambda 0 = 1.45 \ \mu m$. The focal plane
position, y in μ m, and the square electric field of the wave on it, in MV^2/m^2 , are given in pairs
y, E2 as it follows: a) 5.2210; 432.9392 b) 5.1478; 415.5470 c) 5.6902; 353.8914 d)
5.2235; 371.5872 e) 5.3778; 352.4532 f) 5.2421; 324.6345 g) 5.5450; 306.6178 h)
5.5567; 294.7587 i) 5.5567; 272.2729106
Figure 60 - Influence of varied errors on the metalens for $\lambda 0 = 1.50 \ \mu m$. The focal plane
position, y in μ m, and the square electric field of the wave on it, in MV^2/m^2 , are given in pairs
y, E2 as it follows: a) 4.7872; 441.1914 b) 4.4892; 412.9054 c) 5.0734; 441.6080 d)
4.9592; 435.7876 e) 5.1144; 432.6700 f) 4.9180; 422.1848 g) 5.0850; 399.3619 h)
5.1741; 376.0848 i) 5.0028; 341.3763108
Figure 61 - Influence of varied errors on the metalens for $\lambda 0 = 1.55 \mu m$. The focal plane
position, y in μ m, and the square electric field of the wave on it, in MV^2/m^2 , are given in pairs
y, E2 as it follows: a) 4.4481; 408.8204 b) 4.4892; 390.5393 c) 4.4456; 389.1783 d)
4.5300; 399.2400 e) 4.3404; 406.5665 f) 4.6256; 418.2131 g) 4.6594; 411.3966 h)
4.7515; 405.6554 i) 4.5630; 391.0229110
Figure 62 - Influence of varied errors on the metalens for $\lambda 0 = 1.60 \ \mu m$. The focal plane
position, y in μ m, and the square electric field of the wave on it, in MV^2/m^2 , are given in pairs
y, E2 as it follows: a) 4.4481; 410.9337 b) 4.4892; 426.1810 c) 4.4456; 441.9019 d)
4.3196; 443.5039 e) 4.3404; 445.7053 f) 4.5019; 432.3148 g) 4.3267; 405.0702 h)
4.4219: 366.4733 i) 4.5630: 333.4868112

Figure 63 - Influence of varied errors on the metalens for $\lambda 0 = 1.65 \mu m$. The focal plane	
position, y in μ m, and the square electric field of the wave on it, in MV^2/m^2 , are given in pair	rs
y, E2 as it follows: a) 4.1191; 315.9577 b) 4.0648; 319.7048 c) 4.1253; 326.2227 d)	
3.9957; 332.6175 e) 4.0245; 347.9824 f) 4.1857; 376.2801 g) 4.0018; 401.4145 h)	
3.9871; 341.5878 i) 4.1187; 459.317911	4
Figure 64 - Influence of varied errors on the metalens for $\lambda 0 = 1.70 \ \mu m$. The focal plane	
position, y in μ m, and the square electric field of the wave on it, in MV^2/m^2 , are given in pair	rs
y, E2 as it follows: a) 3.6582; 316.3773 b) 3.7319; 327.7093 c) 3.7972; 339.8072 d)	
3.6728; 347.0631 e) 3.3778; 337.764 f) 3.5241; 351.5411 g) 3.5450; 359.6580 h)	
3.5567; 355.5348 i) 3.5567; 354.959711	6

LIST OF TABLES

Table 3.1 - Geometric Parameter values for the pairs wa, wb, in nm, for each angle step
of the supercell of the anomalous refractor
Table 3.2 - Geometric Parameter values for the pairs wa, wb, in nm, for each angle step
of the supercell of the anomalous reflector
Table 3.3 - Geometric Parameter values for the pairs wa, wb, in nm, for each angle step
of the supercell of the metalens
Table 4.1 – Focal plane position and power density of the wave related to each
geometry error of the metalens, considering $\lambda 0 = 1.4 \ \mu m$
Table 4.2 – Focal plane position and power density of the wave related to each
geometry error of the metalens, considering $\lambda 0 = 1.45 \mu m$
Table 4.3 – Focal plane position and power density of the wave related to each
geometry error of the metalens, considering $\lambda 0 = 1.5~\mu m.$
Table 4.4 – Focal plane position and power density of the wave related to each
geometry error of the metalens, considering $\lambda 0 = 1.55~\mu m$
Table 4.5 – Focal plane position and power density of the wave related to each
geometry error of the metalens, considering $\lambda 0 = 1.6 \ \mu m$
Table 4.6 – Focal plane position and power density of the wave related to each
geometry error of the metalens, considering $\lambda 0 = 1.65~\mu m$
Table 4.7 – Focal plane position and power density of the wave related to each
geometry error of the metalens, considering $\lambda 0 = 1.7~\mu m$
Table 4.8 – Focal plane position and square electric field of the wave related to each
geometry error of the metalens, considering $\lambda 0 = 1.4 \ \mu m$
Table 4.9 – Focal plane position and square electric field of the wave related to each
geometry error of the metalens, considering $\lambda 0 = 1.45 \mu m$
Table 4.10 – Focal plane position and square electric field of the wave related to each
geometry error of the metalens, considering $\lambda 0 = 1.50 \ \mu m$
Table 4.11 – Focal plane position and square electric field of the wave related to each
geometry error of the metalens, considering $\lambda 0 = 1.55 \mu m$
Table 4.12 – Focal plane position and square electric field of the wave related to each
geometry error of the metalens, considering $\lambda 0 = 1.60 \mu m$

Table 4.13 – Focal plane position and square electric field of the wave related to each	1
geometry error of the metalens, considering $\lambda 0 = 1.65 \ \mu m$	115
Table 4.14 - Focal plane position and square electric field of the wave related to each	1
geometry error of the metalens, considering $\lambda 0 = 1.70 \ \mu m$	117

LIST OF ABREVIATIONS

EMW: Electromagnetic Wave

DPS: Double Positive Material

RHM: Right Handed Material

LHM: Left Handed Material

DNG: Double Negative Material

ZIM: Zero-Index Medium / Metamaterial

ENG: *Epsilon-Negative Metamaterial*

MNG: *Mu-Negative Metamaterial*

SPP: Surface Plasmon Polariton

TE: Transverse Electric

TM: Transverse Magnetic

SRR: *Split Ring Resonator*

1 INTRODUCTION

MOTIVATION

Metamaterials are causing great impact on microwave frequencies, optical and wireless communications due to their capacity in controlling electromagnetic waves [1]. Their particles are subwavelength-scaled, which causes them to be seen as an effective media as light waves interact with them. Effective medium theory treats them as similar materials those found in nature [2].

These scientific breakthroughs brought to light, through experimentation, physical phenomena that amaze the scientists and researchers, such as negative refraction, invisibility cloak, zero refractive index

Many models of metasurfaces utilize the concept of wavefront shaping [3], in which the metasurface alters the shape of an incident wave by imposing to it a number of successive phase jumps.

The design of metasurfaces that differ from their usual plasmonic MIM (Metal-Insulator-Metal) pattern of composition receives more attention with each day. Through designing metasurfaces that employ only dielectric materials, one can minimize the ohmic losses which are intrinsic of the metal parts.

Some examples of the earliest achievements in all-dielectric metamaterials and metasurfaces come from the proposition of dielectric metamaterials in 2007 [4]. An all-dielectric zero-index medium was proposed in 2011 [5]. The realization of an all-dielectric zero-index metamaterial for optical frequencies [6] occurred in 2013. Wavefront shaping and polarization control through silicon based all-dielectric metasurfaces occurred in 2014 [7].

All-dielectric metasurfaces represent a growing research field within the metamaterial subject. Recent applications include an electrically tunable all-dielectric metasurface [8] for visible light modulation, made of TiO₂ nanodisks immerse in a liquid cristal layer, with transmission modulation over 65%, which represents an interest due to its tuning ability. Another application [9] brings an effective method of controlling sharp Fano resonances in all-dielectric metasurfaces through by breaking

the symmetry of the metasurface in a perpendicular direction one can control the number, frequency and type of high-Q resonances (a resonance that can have greater Q-factor than split-ring-resonators, has its factor attenuated for large asymmetries and appears when metamaterial symmetry is initially broken). And, one more, is the use of this type of metasurfaces for simultaneous wavefront shaping along with polarization rotation of visible light [10].

As the following graphic that relates the utilized referenced to their respective years can show, more works are surging as the years pass:

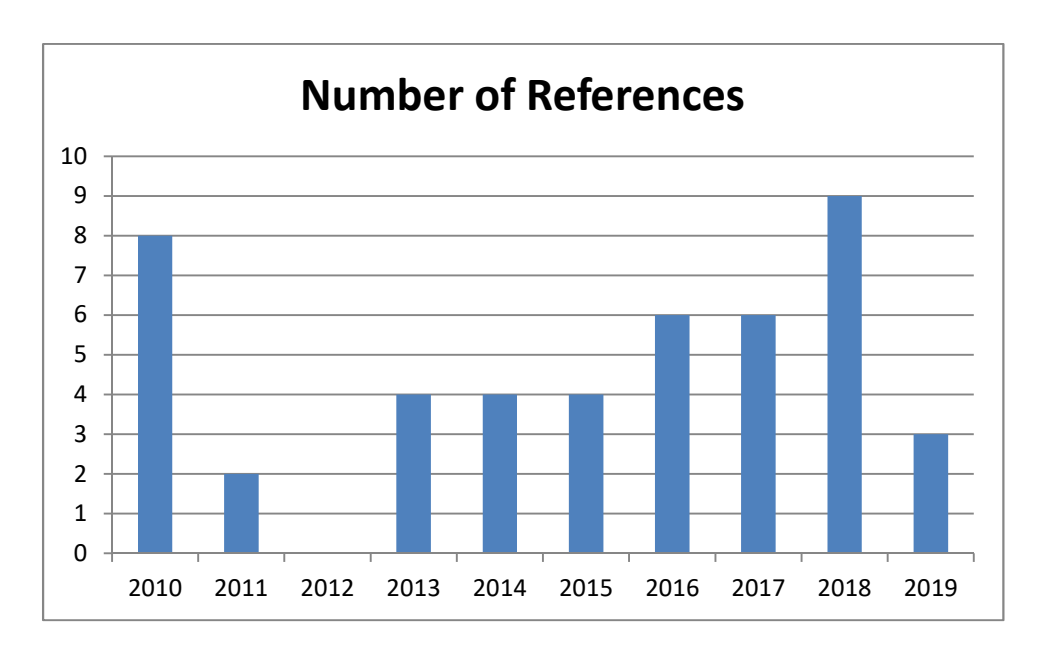


Figure 1 - Frequency of references cited about the subject related to a specific year.

OBJECTIVES

General

All-dielectric metasurfaces are becoming a tendency among the researchers in the field of metamaterials field. Growing efforts are being made in order to present highly efficient metasurfaces, that operate over the global phase range from $-\pi$ to π while develop high absolute values for the refraction and/or reflection coefficients. Multipurpose all-dielectric metasurfaces are also being researched, which will be cited over the text.

This work has the objective of proposing three designs of all-dielectric devices in order to overcome the inconvenience of ohmic losses found in plasmonic metasurfaces through the use of finite elements method modelling software, Comsol Multiphysics 5.2.

To propose all-dielectric structures made of successive squares, by the application of materials with contrasting refractive indexes and test the variations of the dimensions of internal squares (which means to alter the material coverage within the metasurface). To test the basic building block for a wide range of dimensional values that generate the desired conditions for highly efficient devices (global phase control along with elevated transmission/reflection absolute value) [11].

To analyze the performance of the proposed all-dielectric metasurface models considering a perfect geometry.

To analyze the performance of the proposed all-dielectric metasurface models considering a geometry with distributed errors all over its inner squares.

ORGANIZATION OF THIS WORK

Chapter 2 of this work presents the theoretical background of all-dielectric metasurfaces. It starts by presenting the basic concept and nomenclature of metamaterials, their types and applications. Metasurfaces are, then introduced, in terms of their advantages when compared to bulky metamaterials. It is possible, then, to discuss the generalized refraction and reflection equations (see Appendix B for the classic equation according do Fermat's Principle). It is possible, then, to briefly discuss the concept of wavefront shaping. The second chapter ends by introducing all-dielectric metasurfaces.

Chapter 3 presents the three proposed models of all-dielectric metasurfaces. The first model refers to an anomalous refractor. The second model is an anomalous reflector. The third model is a metalens. Their conception is discussed in details: equations that originate each design are shown and how the structures evolve from an unit cell to a supercell, periodic for the refractor and the reflector and aperiodic for the

metalens. Results for the wavelength ranging from 1.4 to 1.7 μm are shown, considering a perfect geometry for the structures.

Chapter 4 introduces the models to a closer approach to the real world through the insertion of geometry errors all over them. Analysis of how their individual performance was altered for punctual values of wavelengths is made.

And, at last, Chapter 5 concludes this work and brings suggestions for future works.

2 LITERATURE REVIEW

2.1 METAMATERIALS: A BRIEF INTRODUCTION

Metamaterials are micro and nano engineered constructions made of "common" materials with complex interaction, capable of exhibiting extraordinary properties as they interact with electromagnetic waves [1]. The structure is a composite of meta-atoms [2, 12] or unit cells: artificial particles smaller than the wavelength, with certain geometries, shapes and materials working as electric and/or magnetic resonators that can be arbitrarily arranged. These work as the building blocks of metamaterials and, for periodic materials, simulations of its interaction with the electromagnetic excitation for a single period describes the whole electromagnetic response of the complete structure.

The name "metamaterial" was created by Walser [13], used to describe the effective behavior of composites. The first unexpected feature of metamaterials is the negative refractive index. Such characteristic was theoretically foreseen by Victor Georgievich Veselago (1929 - 2018) in 1968 [14], who affirmed that there never was an experiment to discover a substance with negative refractive index until then. He also discussed about how to investigate these materials, how it would impact the Doppler Effect and that special lenses could be created based on this trait. It was only in 2000 that Sir John Pendry [15] published a paper that considered negative refractive index, which gave birth to the vision of Veselago and brought a whole new set of possibilities within the metamaterial vast field of research. The same negative refractive index was experimentally verified in 2001 [16].

Metamaterials are also classified according to their resonant state. The resonant type of metamaterials always has narrow bandwidth and heavy losses, but it presents, however, singular values of effective permittivity (and/or permeability). The cited values embrace zero refraction index and negative permittivity (and/or permeability), that creates space for, at least, unusual physical behaviors: tunneling effect, perfect imaging and negative refraction. The nonresonant type of metamaterials, which medium parameters occur over a wideband and have low losses, involves unit-cells far

from the resonance, implying the smooth electromagnetic response that creates its benefits. Their dynamic range of electromagnetic response, however, is small.

Metamaterials are anisotropic in its vast majority. The only cases of isotropic metamaterials occur when it has fully circular symmetry (2D) or spherical (3D).

The analysis of metamaterials requires the use of homogenization laws in order to study their macroscopic properties, since there are heterogenic materials composing the whole set. Unlike the contributions of the isolated materials to the whole structure, the mixing of different materials imply in unexpected properties. A usual criterion for the design is to consider the dimensions of its structure inferior to 0.1 of the operation wavelength, so that the electromagnetic wave propagates through the metamaterial as it would for an homogeneous media. Dimensions are in the order of dozens of nanometers. The form of the internal organization the heterogenic structure is organized, which can be diverse, and the parameters of the base materials, will provide the effective ε_{eff} and μ_{eff} required for the metamaterial to manipulate the EMW as expected.

Homogeneous metamaterials are composed by periodic meta-atoms which dimensions are below the wavelength's. Among their distinct medium possibilities, there are [17] the double positive or right handed materials (DPS or RHM), left handed or double negative materials (LHM or DNG), zero-index medium (ZIM), epsilonnegative (ENG) metamaterials and mu-negative metamaterials (MNG).

The LHM had their existence early foretold by Veselago [11] as he described materials with epsilon and mu both negative, resulting in an unexpected refraction as shown in Figure 2, where the refracted beam doesn't change to the other side of the normal interface line, but is transmitted to the same side where it interacts with the material.

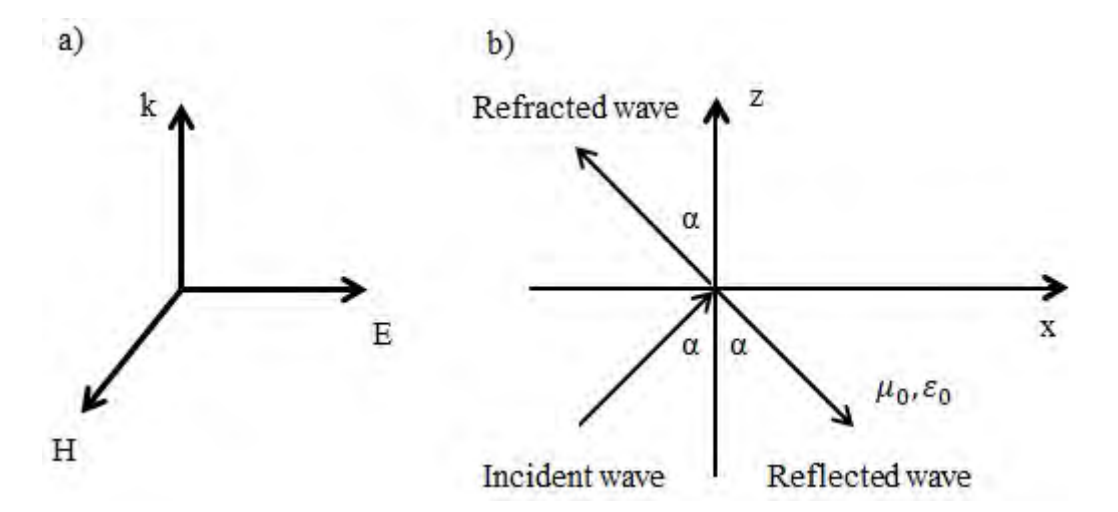


Figure 2 – a) electric and magnetic field with the propagation vector \mathbf{k} as a left handed system b) refraction of EMW through a double negative metamaterial (from [2])

Metamaterials which permittivity or permeability or even both parameters are zero are known as the zero-index metamaterials (ZIM). Such materials can be used to improve the parallel direction of the emitted beam of antennas, for example. When the special case of both permittivity and permeability are zero, electromagnetic waves passing through the metamaterial or metasurface have its direction changed to the normal of the metasurface, which is known as tunneling. As described before, these are resonant metamaterials and their bandwidth, where the zero-index occurs, is expected to be narrow.

Epsilon-negative metamaterials (ENG) are capable of guiding TM mode surface plasmon polaritons (SPP) through the metal-dielectric interface. Such materials are also known as electrical metamaterials. The negative epsilon can be found in materials that occur in nature for certain frequency ranges, such as noble metals as gold when considering optical frequencies, doped semiconductors operating in frequencies that are lower than plasma.

Mu-negative metamaterials (MNG) are capable of working as a slab, guiding TE mode SPPs when interfacing a positive-mu material. These materials do not occur in nature, however there are structures such as the split ring resonator (SRR) that offer this feature and other artificial structures.

2.2 METASURFACES

Metasurfaces are the 2D version of metamaterials, which thickness is smaller than the wavelength [18]. Related to its thickness, its greater ease of construction, if compared to 3D metamaterials, and the lower losses that are expected to occur as the radiation penetrates the depth of the material are initial advantages that motivated more and more studies over the last years.

When conventional optical components are considered, interaction with light occurs as it propagates through the material depth, causing changes in the amplitude, phase and/or polarization state of the wave. Consequently, optical components, such as lenses, refractors, reflectors and other kinds have its design with high considerations about thickness. As optical miniaturization is increasingly spreading through a number of electromagnetic devices, the study field of metasurfaces acquires greater importance, for these nearly plane devices can play their role much more efficiently than conventional components. Besides, metasurfaces can perform more functions over the EMW, such as anomalous refraction and reflection, negative refraction of the light and other effects that are not found in natural materials.

Differently of many metamaterials, which will remain for some time, yet, as not more than simulations, its planar counterpart can be fabricated by lithography or other method like nanoimprints, which already exists. This attractive drives many researchers to move further beyond simulations and turn them into physical components. This ultrathin film can greatly diminish losses, compared to bulky metamaterials, considering the proper structure and materials. Metasurfaces have been attracting overwhelming interest of researchers due to its increasing effectiveness in controlling, which allows them to dismiss bulky metamaterials that could be necessary otherwise.

Since its thickness is subwavelength, metasurfaces can offer critical changes in optical properties of the radiation as it propagates through a thin interface. The design is done through the use of optical scatterers which spacing among each other is smaller than the wavelength and by utilizing different quantities of materials along the structure. The result is a surface that changes the optical properties of the wave depending on which

point of it the incidence is considered (in other words, the optical response varies along the metasurface).

2.3 GENERALIZED LAWS OF REFRACTION AND REFLECTION AND ITS CORRESPONDING ANOMALOUS PHENOMENA

It is well-known among vast classic literature about optical properties that when the radiation interacts with the interface between two homogeneous materials, its initial intensity is split into the transmitted and reflected [19, 20], which are given by the classic Snell's law and Fresnel equations:

$$n_i \sin \theta_i = n_t \sin \theta_t \tag{2.1}$$

$$\theta_i = \theta_t \tag{2.2}$$

Since the treated subject is metasurfaces for purposes that include highly efficient refraction and reflection, absorbed intensity of radiation will not be considered in the present discussion.

It has been previously discussed that the electromagnetic wave suffers reflection and refraction when it reaches a boundary between two homogeneous media. When it comes to metasurfaces, however, this boundary is constituted by a thin array of subwavelength optical scatterers ("optical antennas") that makes them capable of shaping the wavefront and/or converting the polarization of the incident field. Phase changes caused by the metasurface can be contained inside the global range from $-\pi$ to π : this metasurface is said to have been designed to perform global phase control of the incident wave. If the metasurface causes uniform phase change to the wave, it conserves both reflected and refracted directions of the wave (linear phase profile).

Such consideration – linear phase profile – is taken as basis to determine the appropriate model of metasurfaces to develop high efficiency anomalous refraction and reflection, while a quadratic phase profile metasurface is the adequate one for the metasurface operation as a flat lens, focusing incident electric field around a previously designed focal plane. More details are shown in chapter 3.

Fermat's principle is discussed in the Appendix of this work, serving as a background for the classic reflection and transmission. The structure of a metasurface is composed of unit cells (or groups of unit cells) that are organized in a material variation profile that acts by causing the necessary discrete phase jumps on the incident wave.

The groups of cells that work as optical antennas cause the phase jumps in a way that the optical path remains stationary. That guarantees the propagation through the optical path, which yields the generalized laws of refraction and reflection [19, 20] as it follows in equation 2.3 for the transmission and in equation 2.4 for the reflection.

$$\begin{cases} n_t \sin \theta_t - n_i \sin \theta_i = \frac{1}{k_0} \frac{\partial \varphi}{\partial x} \\ \cos \theta_t \sin \theta_t = \frac{1}{n_t k_0} \frac{\partial \varphi}{\partial y} \end{cases}$$
 (2.3)

The free space wave vector is given by k_0 . The phase gradient components on the metasurface are given by $\frac{\partial \varphi}{\partial x}$ and $\frac{\partial \varphi}{\partial y}$. If the phase gradient is not considered, the generalized equation in equation 2.3 becomes the classic Snell's law. The variables n_i , n_t , θ_i , θ_t , φ_t and φ are, respectively, refractive index of the media from where the wave comes, refractive index of the media where the wave is transmitted to, angle of incidence, projection angle of the transmitted beam related to the normal plane, projection angle of the transmitted beam related to the plane of incidence and phase profile.

The reflection equations are given as it follows:

$$\begin{cases} \sin \theta_r - \sin \theta_i = \frac{1}{n_i k_0} \frac{\partial \varphi}{\partial x} \\ \cos \theta_r \sin \theta_r = \frac{1}{n_r k_0} \frac{\partial \varphi}{\partial y} \end{cases}$$
(2.4)

About equation 2.4, n_r is the refractive index of the media where the wave is reflected to. The other variables are already described following equation 2.3.

It can be noticed that the incident angle equals the reflection angle if the phase gradient is not taken into account.

The generalized laws include the phase gradient of the metasurface, which works as a wave vector that is applied to the incoming wave. By controlling the phase gradient through the appropriate design of the metasurface, within a chosen wavelength range, one can redirect the incident wave as desired.

The models shown in this were created by utilizing successive wave scatterers to control the phase of the incident wave within the global range from $-\pi$ to π . These unit cells were positioned one close to the next in an array, as it will be explained in chapter 4. The distance between two scatterers is very inferior compared to the wavelength. According to the Huygen's principle, incident spherical waves can, then, interact with the metasurface and leave it having planar wavefronts.

Experimental demonstration results of the generalized laws of refraction and reflection can be seen in [19], where eight V-shaped gold antennas are in a periodic arrangement. The metallic antennas have subwavelength spacing to generate the proper scattering, but not too small, as it necessary to prevent strong coupling of the near-field among each pair of antennas. Phase gradient is kept constant along the plasmonic interface through the use of periodic supercells (each one compose of the eight rotated V-shaped antennas), though it is not a required condition for the usage of the generalized laws. Such is shown in the results, where both periodic and aperiodic structures are utilized.

Periodic structures are chosen for the refractor and the reflector metasurface models, whiles an aperiodic structure is set for the metalens. The three models presented in this work consist in all-dielectric metasurfaces.

Yet another application of the generalized laws is a plasmonic device interface that creates vortex beams from normally incident light with linear polarization. Vortex beams can be used to rotate particles [21] or to encode information in optical communication systems [22].

2.4 WAVEFRONT SHAPING

Metasurfaces are able to model wavefronts as desired. This trait is required to perform the functions of anomalous refraction, reflection and metalenses (or flat lenses).

It is desirable to elevate the efficiency of the anomalous refractor by totally obliterating the reflection. That can be considering the principles of Huygens' surfaces by causing the following relation [18] among the electric polarization (α_e), magnetic polarization (α_m) and the impedance of the surrounding media (η_0):

$$\sqrt{\frac{\alpha_e}{\alpha_m}} = \eta_0 \tag{2.5}$$

The transmission coefficient, t, is given by:

$$t = \tau e^{j\varphi_t} \tag{2.6}$$

The absolute value of t is given by τ , while its phase is represented as φ_t .

Global phase control implies that the wave will be able to obtain phase jumps from $-\pi$ to π . To reach such condition, α_e and α_m can be adjusted over the metasurface, through its geometry, spacing and applied materials, satisfying equation 2.6.

A device that works according to wavefront shaping is the Metalens, which can convert, for certain wavelengths, planar wavefronts that incide normally over it to spherical wavefront. In order to develop a model of metalens, one must consider the following quadratic phase profile in equation 2.7:

$$\varphi_L(x,y) = \frac{2\pi}{\lambda} \left(\sqrt{x^2 + y^2 + f^2} - f \right)$$
 (2.7)

Where *f* is the focal distance from the metalens.

2.5 ALL-DIELECTRIC METASURFACES

Plasmonic metasurfaces have already achieved a long range of applications and represent a widely studied field within the metamaterial the metamaterial subject. When it comes to efficiency, however, its metallic parts come with the inconvenience of ohmic losses. These are more expressive in the optical domain. In the recent years, in order to overcome such issue, research on metasurfaces that uniquely employ dielectric materials with high refractive index, which represent negligible losses, thus solving the efficiency problem.

All-dielectric metasurfaces are built, as the name suggests, by dielectric resonators. The resonators have their size d considerably diminished as the electric permittivity, given by ϵ , grows due to the approximate proportionality relation that follows:

$$d \sim \frac{\lambda_0}{\sqrt{\epsilon}} \tag{2.8}$$

The reason for choosing materials with high refractive index can be understood by observing the relation [23] among the refractive index n, the relative magnetic permeability μ_r and the relative electric permittivity ϵ_r :

$$n = \sqrt{\mu_r \epsilon_r} \tag{2.9}$$

Since the magnetic permeability μ for dielectric materials is approximately equal to the vacuum permeability $(4\pi.\,10^{-7}$ H/m), it occurs that $\mu_r = {}^{\mu}/{\mu_0}$ is about the unity and equation 2.7 can be rewritten as it follows:

$$n = \sqrt{\epsilon_r} \tag{2.10}$$

Equation 2.8 implies that the refractive index approximation for dielectric materials solely depends on the relative electric permittivity $\epsilon_r = \epsilon/\epsilon_0$, where $\epsilon_0 = 8.85 * 10^{-12} \, F/m$ is the vacuum electric permittivity. This explains how the dimension d of the dielectric resonators decreases through the use of high refractive index materials over the geometry of the metasurface.

When designing all-dielectric metasurfaces, though materials with higher ϵ values can miniaturize the size of their composing resonators, there are two tendencies for the permittivity that has to be considered: the greater the ϵ is, the narrower bandwidth is supposed to be, as well as for the radiation frequency, which also decreases with higher values of ϵ . This last tendency can be dealt with by utilizing a metallic ground plane as a base for the placing of the resonators.

In order for the amount of dielectric resonators to work as an all-dielectric metasurface, it is necessary to cause a magnetic response over them [24], so that it, may express the uncommon properties of metamaterials/metasurfaces, such as the negative refractive index (see section 2.1).

As written in section 2.3, global phase control represents the phase jumps from $-\pi$ to π enables the metasurface to perform wavefront shaping (which is done by the proposed devices) and polarization conversion. This whole range can be distributed successfully over the dielectric metasurface by changing the geometric parameters of the unit cells.

3 ANOMALOUS REFRACTOR, ANOMALOUS REFLECTOR AND METALENS – DEVICES AND RESULTS CONSIDERING IDEALLY STRUCTURED MODELS

3.1 INTRODUCTION

This chapter is dedicated to introduce the three proposed devices of this work [25 - 27]. In order to do so, it gathers the theory of the dispositives, explanations about how the proposed models were designed and state of the art models so far. Results for the ideal models and practical models which include more real world approximations through introduction of errors will be left for chapter 4, specifically about results.

Before the advent of metamaterials, classic Snell's law foresaw how a beam of light was supposed to bend when it crossed from one homogeneous transparent media to another. Additionally, if normal incidence of light occurred over the interface between the two media, normal transmission was totally expected to occur. Metamaterials and, mostly, metasurfaces, however, have tremendous potential for achieving previously unforeseen electromagnetic phenomena, such as the anomalous transmission of light [25, 26], anomalous reflection and high resolution metalensing [15, 27]. A simplistic illustration of this idea is shown in Figure 3:

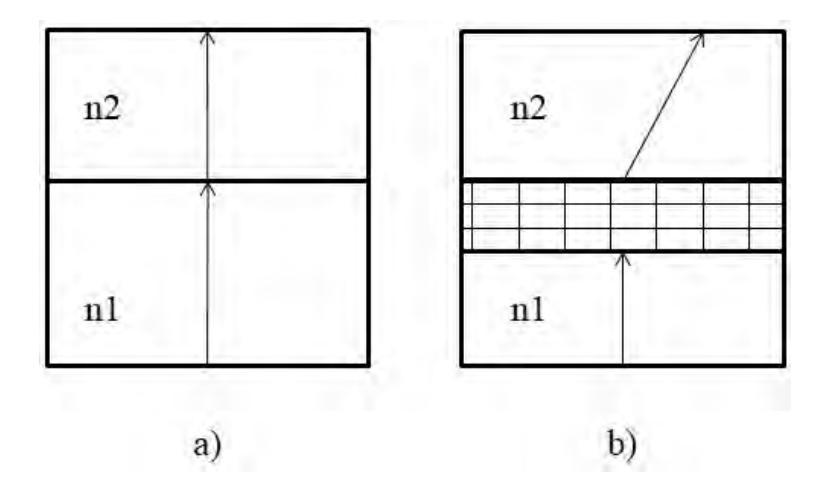


Figure 3 – Simplistic comparison of classic and anomalous refraction of normally incident light. a) Classic approach. b) Metasurface approach, in which it acts as an anomalous refractor.

Fresnel equations demonstrate how the light is reflected when it interacts with a perfect mirror. A special case is the one of normal incidence, in which case the beam of

light is reflected in the same direction of where it came from. When it comes to metasurfaces, it is possible to perform the anomalous reflection of light. For the same cited special case, the anomalous reflection caused by the metasurface imposes the normal beam of light to reflect in a bent direction. Again, for an initial idea, a simplistic illustration of the idea is shown in Figure 4:

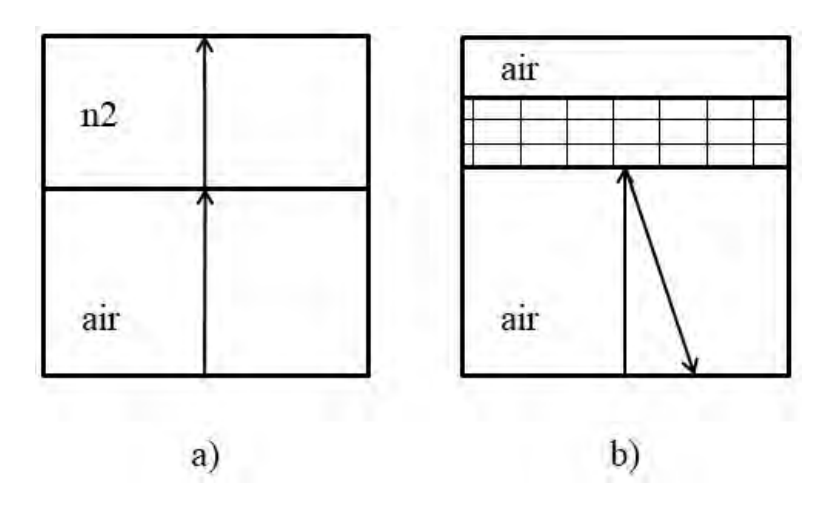


Figure 4 - Simplistic comparison of classic and anomalous reflection of normally incident light. a) Classic approach. b) Metasurface approach, in which it acts as an anomalous reflecting mirror.

For a description about how the classic refraction and reflection equations can be derived from Fermat's principle, see Appendix B. Generalized equations explaining the anomalous phenomena are set in section 2.3.

3.2 ANOMALOUS REFRACTOR

The design of the anomalous refractor begins with its unit cell pattern, shown in Figure 5. Unit cell is the basic block of the metasurface. The proposed model for the anomalous refractor starts from ABA type of unit cell, which is composed of three squares, where the first is just like the third one. This, together with the proper variation of the dimensions w_a and w_b along the metasurface, is enough to ensure that the transmission is maintained over 90% while the metasurfaces also performs global phase control.

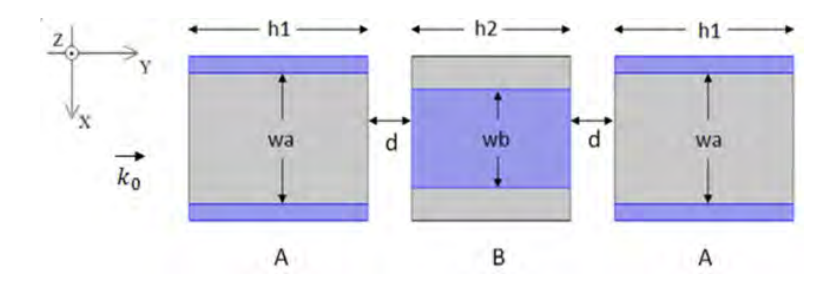


Figure 5 – Schematic view of the unit cell of the metasurface, with its dimensions and employed materials. In blue, Si. In gray, Air. Dimensions \mathbf{w}_a and \mathbf{w}_b vary from 20 up to 230(nm). h1 = 300(nm), h2 = 250(nm) and d = 50(nm). Incident electrical field is polarized in x direction. The space among the blocks is filled with air.

The employed materials for the unit cell have refractive index of 3.4757 for Si and 1 for air. Operation wavelength is 1.55 μ m because of the low losses in silica fiber optic. For the proposed model, the phase of the normal electric field gains increments, phase jumps, only through the x direction. This means that there is no phase gradient in y direction, $\frac{\partial \varphi}{\partial y}$. Thus, the second equation of equation 2.3 and equation 2.4 are equal to zero for the proposed model. The necessary linear phase profile $\varphi(x)$ that turns the metasurface into an anomalous refractor (or transmitter) consists, ideally, of a straight line, denoted by equation 3.1. The dependence of $\varphi(x)$ with respect to the transmission angle θ_t comes along with the α parameter [28], which is specifically shown in equation 3.2:

$$\varphi(x) = \alpha x \tag{3.1}$$

$$\alpha = -k_0 \sin(\theta_t) \tag{3.2}$$

About equations 3.1 and 3.2, the α parameter is a function of the chosen transmission angle. Ultimately, having chosen the transmission angle, $\varphi(x)$ in equation 3.1 can be solely considered as a function of the position x.

The design of this model considered as pre-requisites that the metasurface should be able to perform global phase control, besides achieving a transmission coefficient, τ , as close to 1 as possible. In other words, the model intends to bend and transmit about the whole incident electric field. In an ideal case, the absolute value of the transmission coefficient, $\tau=1$ would occur for any phase φ ranging from $-\pi$ to π . The transmission coefficient is given by $t=\tau e^{j\varphi_t}$ (equation 2.6).

Other designs might consider a different goal for the metasurface. In [29] a metasurface is shown as a versatile, multifunctional device working times as an anomalous refractor, times as a reflecting mirror or a beam splitter, according to the incidence angle.

The transmission coefficient t is then tested for a variety of w_a , w_b dimensions, both swept from 20 to 230 nm. The result is the absolute value of transmission, mapped as the regions of higher and a few lower transmission areas. Figure 6 shows a widespread zone of elevated absolute value of the transmission coefficient, τ , way over 90%. This means that the incident electrical field is transmitted at its almost full intensity.

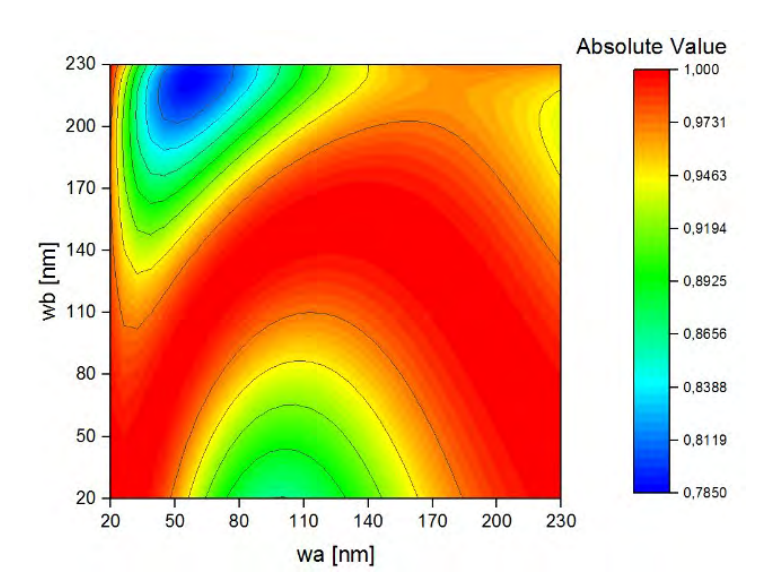


Figure 6 - Absolute value of the transmission coefficient τ of the electric field mapped for each pair (w_a, w_b) varying from 20 to 230 (nm) of the anomalous refractor.

The phase of the transmission coefficient is also verified for the same (w_a, w_b) pairs, resulting in the phase map shown in Figure 7. Phase shifts all around the range from $-\pi$ to π are shown. This implies that the metasurface is able to perform global phase control, a necessary condition to work as the anomalous refractor.

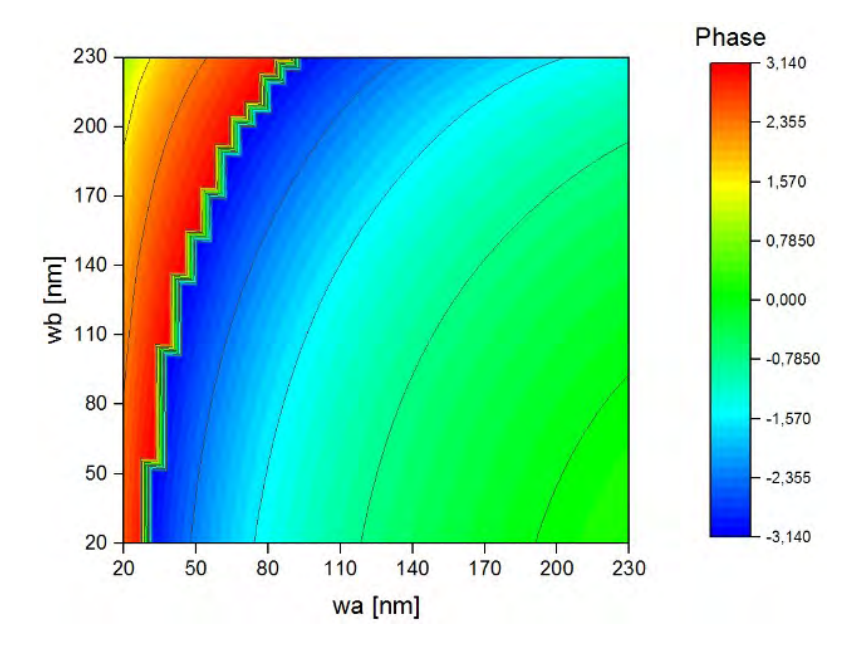


Figure 7 – Phase of the transmission coefficient for the electric field mapped for each pair (w_a, w_b) varying from 20 to 230 (nm).

The next step is to choose a curve of (w_a, w_b) pairs that is simultaneously common to Figures 6 and 7 that represents the phase shifts on the global range from $-\pi$ to π while the absolute value of the transmission coefficient is kept high, over 0.9.

A corresponding table of values, which generated Figures 6 and 7, was obtained and those pair of values w_a , w_b found to be more adequate for the unit cells to attend to global phase control along with high transmission. The smallest number of different pair values that sufficed the aforementioned conditions was 5, which stands for 5 different unit cells. These values are enlisted in Table 3.1, as it follows:

Table 3.1 GEOMETRIC PARAMETERS OF THE UNIT CELL				
Cell / Param.	w_a	w_b		
1	52.308	84.615		
2	73.846	46.923		
3	230	63.077		
4	219.23	30.769		
5	30.769	230		

Table 3.1 - Geometric Parameter values for the pairs (w_a, w_b) , in nm, for each angle step of the supercell of the anomalous refractor.

Table 3.1 might be understood as indicating the points of the same curve that will traverse both absolute value and phase for the maps of Figures 6 and 7, posted as it follows, now marked in Figure 8, for a simpler observation:

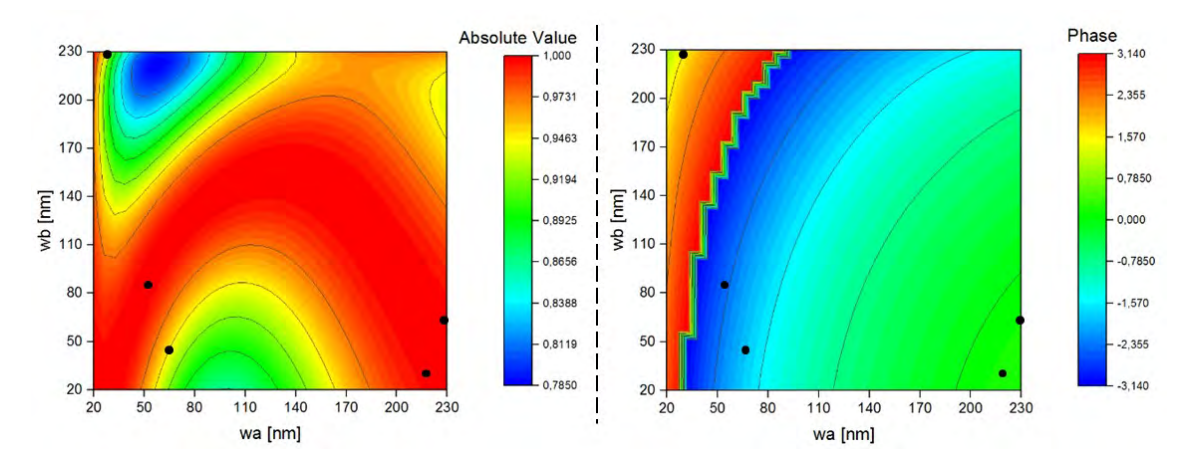


Figure 8 - Absolute value and phase of the transmission coefficient with angle steps marked on the maps.

In order to reproduce the approximate necessary linear phase profile, the five points of Table I were taken as five angle steps. Each angle step consists in 3 side-by-side unit cells. These represent the successive phase jumps that the metasurface adds to the electric field as it is crossed. While in simulations, the use of two adjacent unit cells could even strengthen the absolute value of the transmission coefficient, however the global phase control would be compromised. This explains the use of three adjacent unit cells for the model.

By stacking together 5 angle steps of three unit cells each one, the supercell of the anomalous refractor was then defined. The angle step has $\Gamma=750$ nm, thus the length of the 5 angle steps that compose the whole structure is $\Lambda=3750$ nm. The wave vector in free space, k_0 , implies that the electromagnetic wave propagates normally to the metasurface, along the y direction. The supercell is designed to periodically repeat itself to the left and to the right considering Floquet periodicity. The structure is shown in Figure 9.

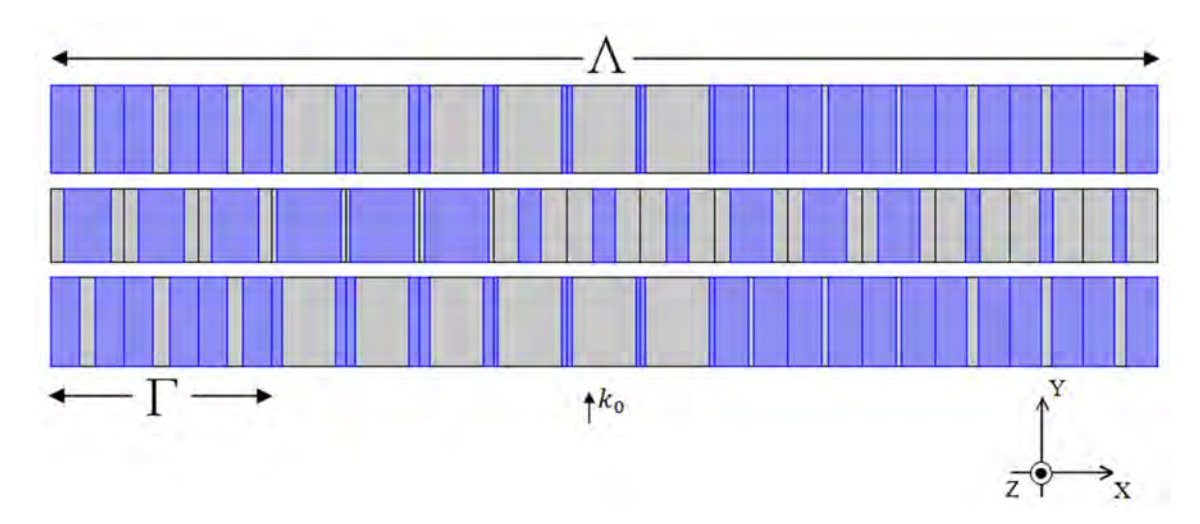


Figure 9 – supercell of the metasurface, which considered dimensions are angle step $\Gamma = 750$ (nm) and total length of $\Lambda = 3750$ (nm). Material distribution is given by Air, in gray, and Si, in blue. The space among the structures is filled with air. Incident electric field is polarized in x direction.

The chosen transmission angle for the refractor was 25°, though the obtained one, in practice, was 24.17°. Substituting in equation 3.2 yields $\alpha = 1.67$, thus equation 3.1 of the linear phase profile becomes $\varphi(x) = 1,67x$. As the supercell is periodically repeated to the sides, so is the phase profile produced by them. Global phase range is represented in Figure 10 in multiples of π rad along the position x, same as the polarization of the electric field.

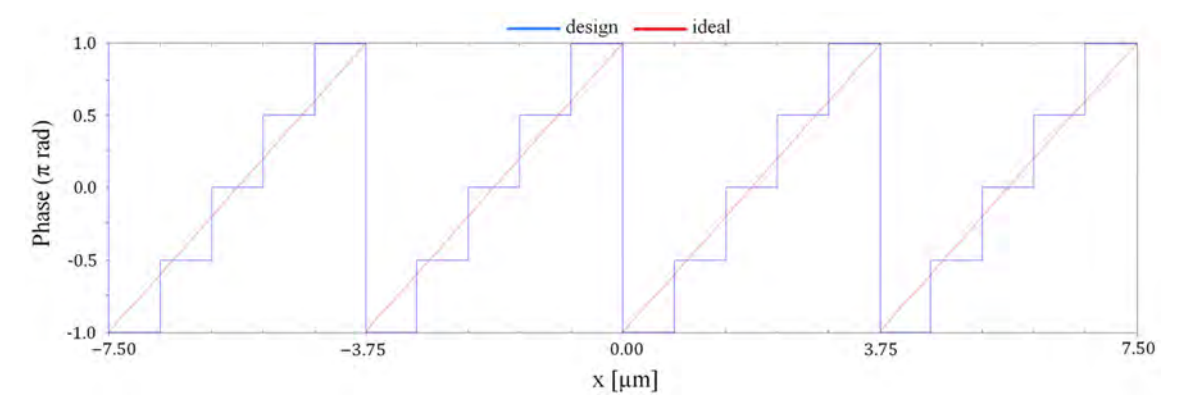


Figure 10 - Phase profile of the metasurface through the global range from $-\pi$ to π , as a function of the position x.

Each supercell has a length of $3.75~\mu m$. In Figure 10, the first one is within the interval from 0 to $3.75~\mu m$. Since the design of the metasurface considers Floquet periodicity, it repeats to left and right sides, yielding the repeated phase profile to the sides, as shown in Figure 10. Results considering the operation of the ideally built anomalous refractor, without any errors in its metastructure are shown in Figure 11.

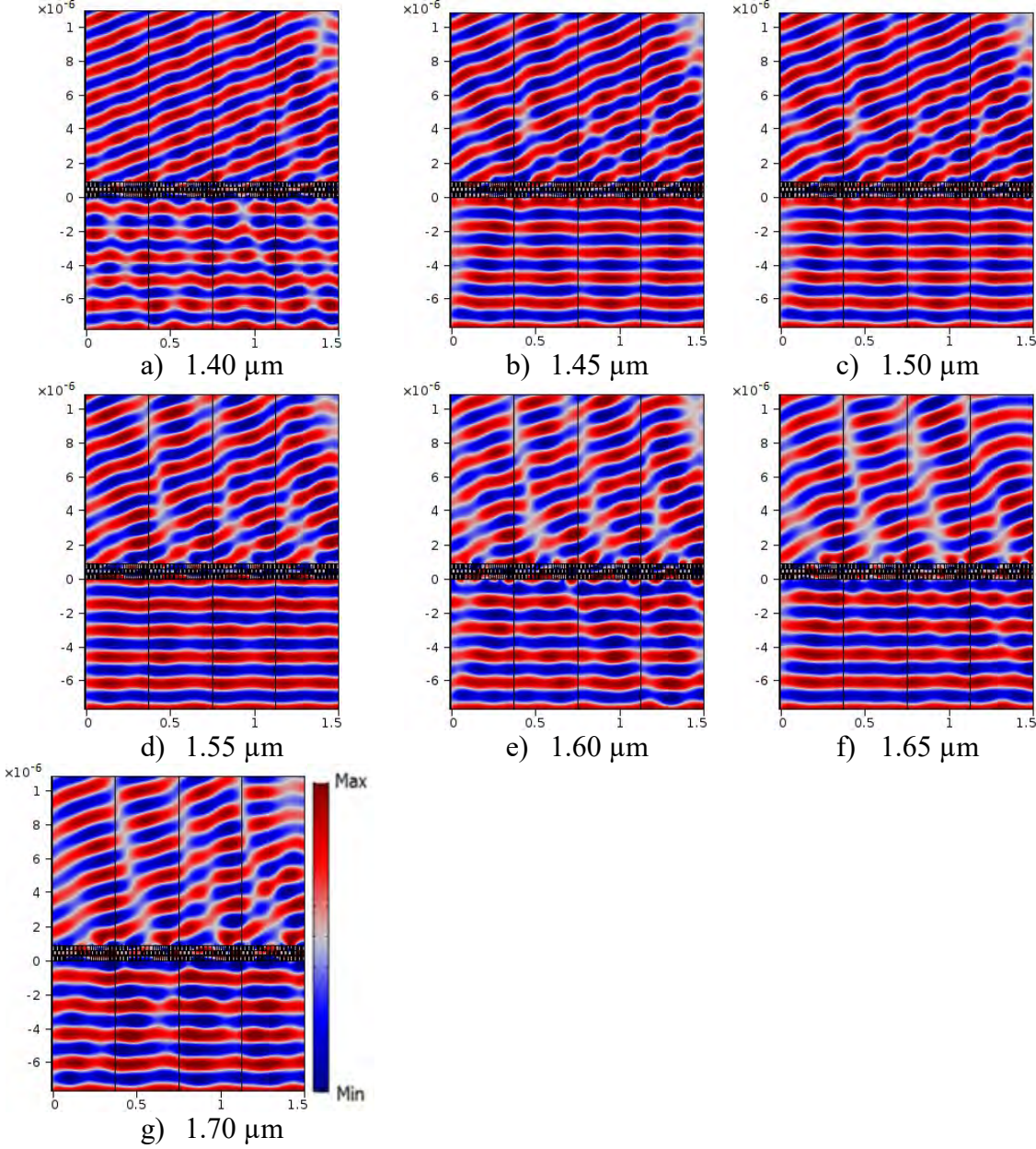


Figure 11 - x component of the electric field, in V/m. Operation of the anomalous refractor as a function of the wavelength, λ_0 , without considering errors within the structure.

Figure 11 shows, within the simulated operation of the proposed model, the influence of the wavelength over the device. Equation 3.2 directly depends on the wavelength λ_0 , which affects the wave vector, k_0 and, consequently, the α parameter. The α parameter is what defines how the phase profile $\varphi(x)$ will cause the successive phase jumps over the crossing electric field. This explains why the transmission angle can be visualized changing as the wavelength grows from 1.4 μ m to 1.7 μ m in steps of 0.05 μ m.

The analysis of the devices considering possible errors in the supercell structure that may occur during its fabrication were left for chapter 4, in which a comparison is made to the ideal case shown here.

The concept of the proposed model may permit designs for many applications such as ultrathin gratings, cloaking, lenses within the range of infrared and visible spectra for wireless optical communications.

3.3 ANOMALOUS REFLECTOR

Previously, the construction of a model of an anomalous refractor was shown based on satisfying the generalized Snell Laws where global phase control and high transmission were determinant to succeed with the modelling. Now, similar principles are followed to obtain the model of the proposed anomalous reflector. A basic idea of what the phenomena was shown in section 3.1. This section concerns with the step-by-step modelling of the device. In order to do so, it is a prime rule to obtain global phase control for the reflected electric field and, as close as possible, to nullify any transmitted electric field through the device. The reflection coefficient, r, is expressed by:

$$r = |r|e^{j\varphi_r} \tag{3.3}$$

The reflector requires the attendance of the set of equations 2.4. Since the structure of the metasurface has a design in which the electric field is polarized only in the x direction, the y component of the phase gradient is null. This means that only the first equation of the referred set is considered.

The design starts with the model of the unit cell of square blocks, which employs two square blocks backed up by a silver (Ag) substrate, shown in Figure 12. The Ag substrate is used for the rough reflection of the incident wave, without implying losses, which ensures the all-dielectric characteristic of the proposed device. The unit cell is composed by the following materials: Si, in dark blue; SiO₂, in gray; and Ag in pale blue and Air, making a gap distance between the two first blocks to the left of Figure 11. The three square blocks all have equal outer lengths p = 250 nm.

The employed materials for the unit cell have refractive index of 3.4757 for Si, 1.4440 for SiO_2 and 1 for Air. Operation wavelength is 1.55 μ m.

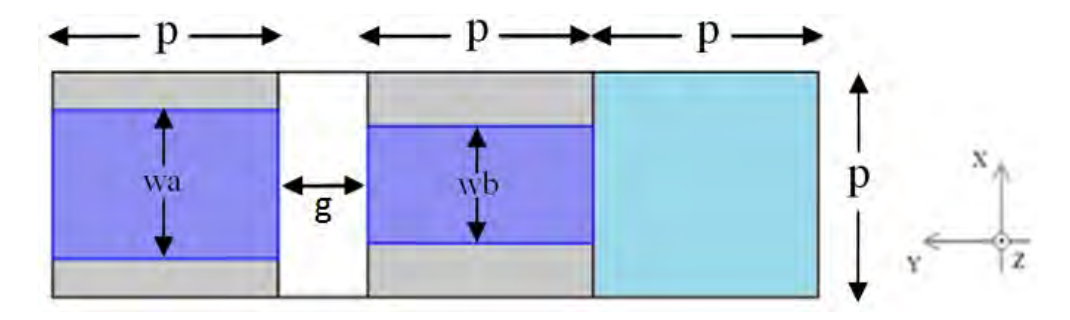


Figure 12 - Unit cell of the reflector; air gap between resonators in white, distance denoted by g; dark blue is for Si fulfilling the inside of the blocks; SiO_2 is in gray, around the Si; The ground plane substrate, in pale blue is in Ag; Dimensions of the cell are p = 250 nm, g = 100 nm. Both w_a , w_b vary from 20 to 230 nm. The incident electric field is polarized in x direction.

The inner lengths w_a and w_b are swept from 20 to 230 nm in order to generate the maps with the distributions of absolute value |r| and phase φ_r that compose the reflection coefficient r, of equation 3.3. These are exhibited in Figures 13 and 14, respectively:

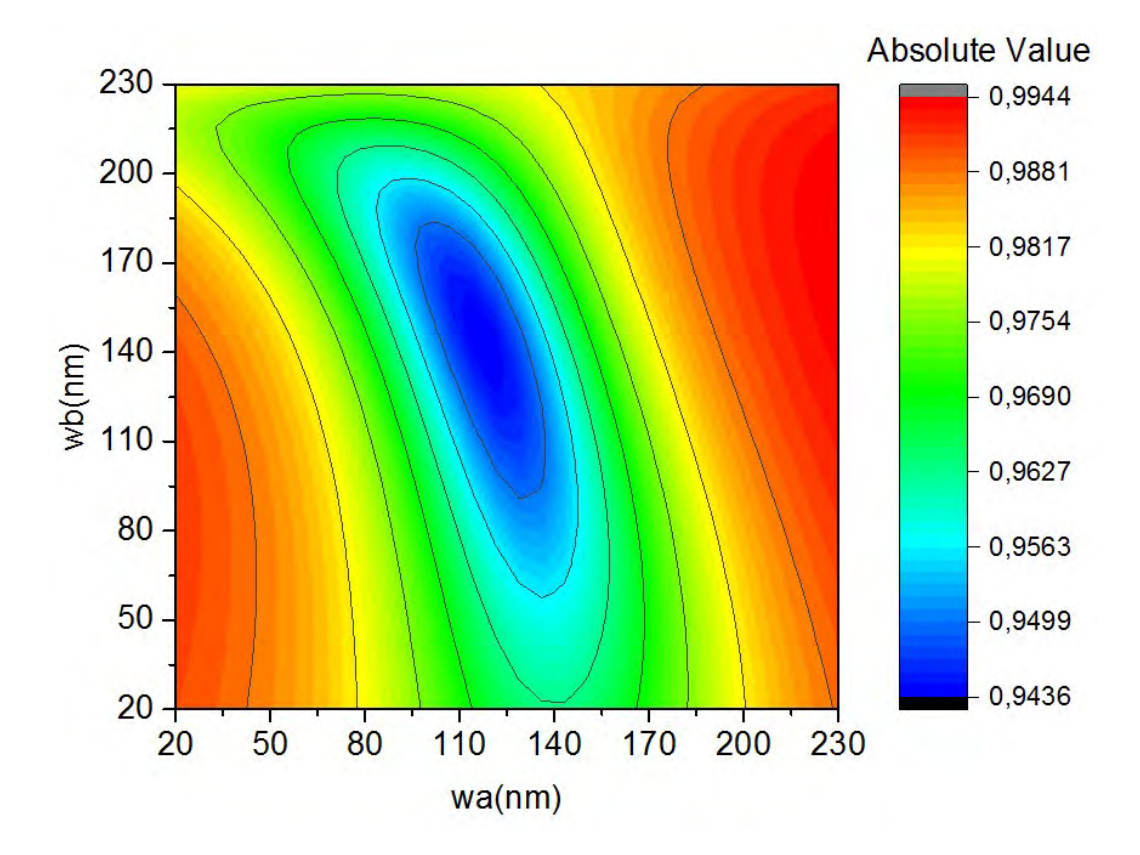


Figura 13 - Distribution of the absolute value of the reflection coefficient of the metasurface tested for w_a and w_b varying from 20 to 230 nm.

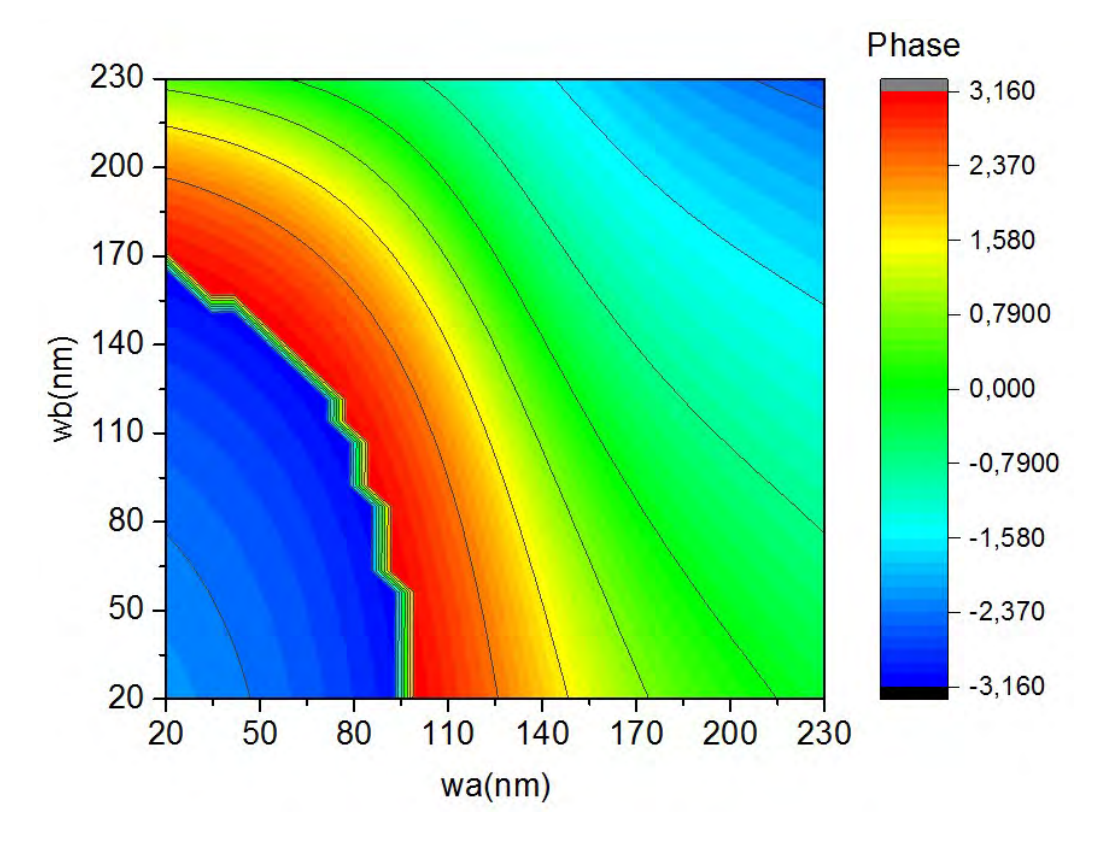


Figure 14 - Phase of the reflection coefficient of the electric field for w_a and w_b varying from 20 to 230 (nm).

Once obtained the maps, the next step is to choose a set of (w_a, w_b) pairs that imply a curve that is simultaneously common to Figures 13 and 14 that represents the phase shifts on the global range from $-\pi$ to π while the absolute value of the reflection coefficient is kept high, over 0.9.

A corresponding table of values, which came from Figures 13 and 14, was obtained considering those pairs of values for w_a , w_b that were found to be more adequate for the unit cells to attend to global phase control along with high reflection. The smallest number of different pair values that sufficed the aforementioned conditions was 7, which stands for 7 differently fulfilled terms of unit cells – the angle steps of the discretized phase profile that cause the phase shifts on the electric field as it traverses the metasurface. These values are enlisted in Table 3.2:

TABLE 3.2 GEOMETRIC PARAMETERS OF THE UNIT CELL			
Cell / Param.	w_a	w_b	
1	164.83	20	
2	208.28	215.52	
3	99.655	230	
4	230	56.207	
5	222.76	20	
6	193.79	48.966	
7	157.59	34.483	

Table 3.2 - Geometric Parameter values for the pairs (w_a, w_b) , in nm, for each angle step of the supercell of the anomalous reflector.

Table 3.2 might be understood as indicating the points of the same curve that will traverse both absolute value and phase for the maps of Figures 13 and 14, posted as it follows, now marked in Figure 15, for a simpler observation:

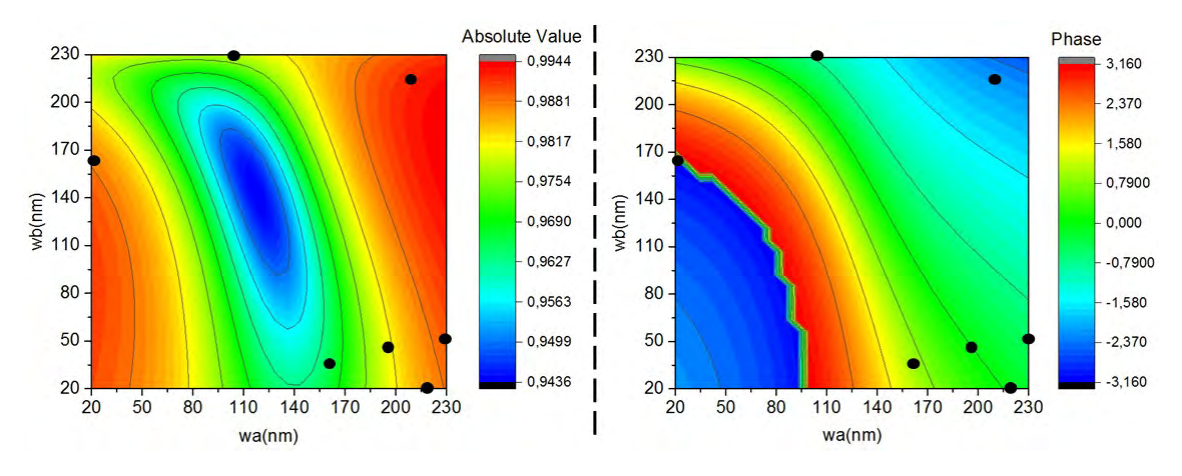


Figura 15 - Absolute value and phase of the transmission coefficient with angle steps marked on the maps.

These seven angle steps that discretize the phase profile are shown as the supercell of the metasurface, in Figure 16. It has two major dimensions: the length Γ of the angle step and the total length Λ . Each angle step is a ternary of three equal and

adjacent unit cells, which makes its length $\Gamma = 750$ nm. The seven angle steps that form the supercell imply, then, the total length of $\Lambda = 5250$ nm. Same as for the previous proposed model, the supercell is designed to periodically repeat itself to the left and to the right considering Floquet periodicity and the wave vector in free space, k_0 , implies that the electromagnetic wave propagates normally to the metasurface, along the y direction.

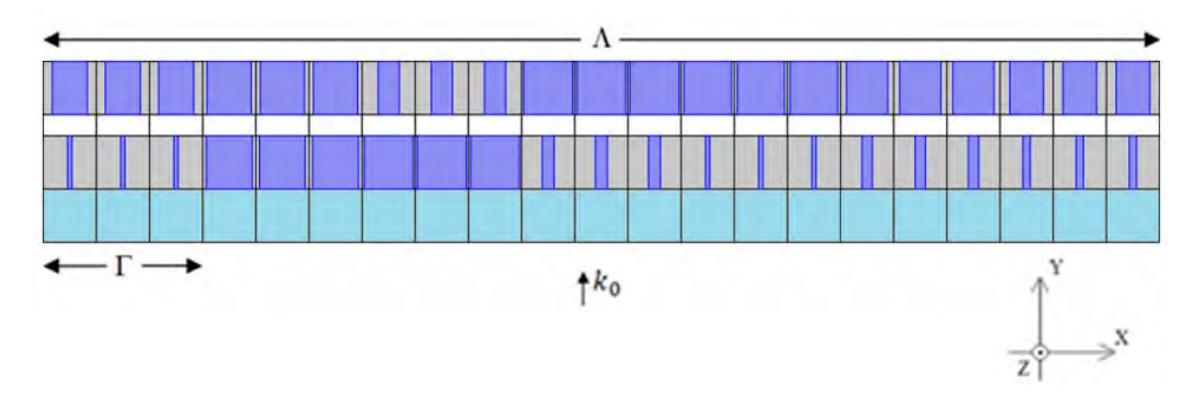


Figura 16 - Supercell of the metasurface. $\Gamma = 3p = 750$ nm; $\Lambda = 21p = 5250$ nm; The incident electric field, in V/m is polarized in x direction.

The phase profile for the reflector is given by equation 3.4:

$$\varphi(x) = -\alpha x \tag{3.4}$$

Since the treated phenomena is reflection, the α parameter is obtained by the same way described for the refractor, however the phase profile has changed signal, which implies in a decreasing straight line for the phase profile.

The chosen reflection angle for the proposed model was 17.17°. Substituting in equation 3.2 yields $\alpha = -1.19$, thus equation 3.5 of the linear phase profile becomes $\varphi(x) = 1{,}19x$. As the supercell is periodically repeated to the sides – due to Floquet periodicity applied to its sides – the phase profile produced by them is as well. Global phase range of $-\pi$ to π is represented in Figure 17, in multiples of π rad, along the position x, same as the polarization of the electric field.

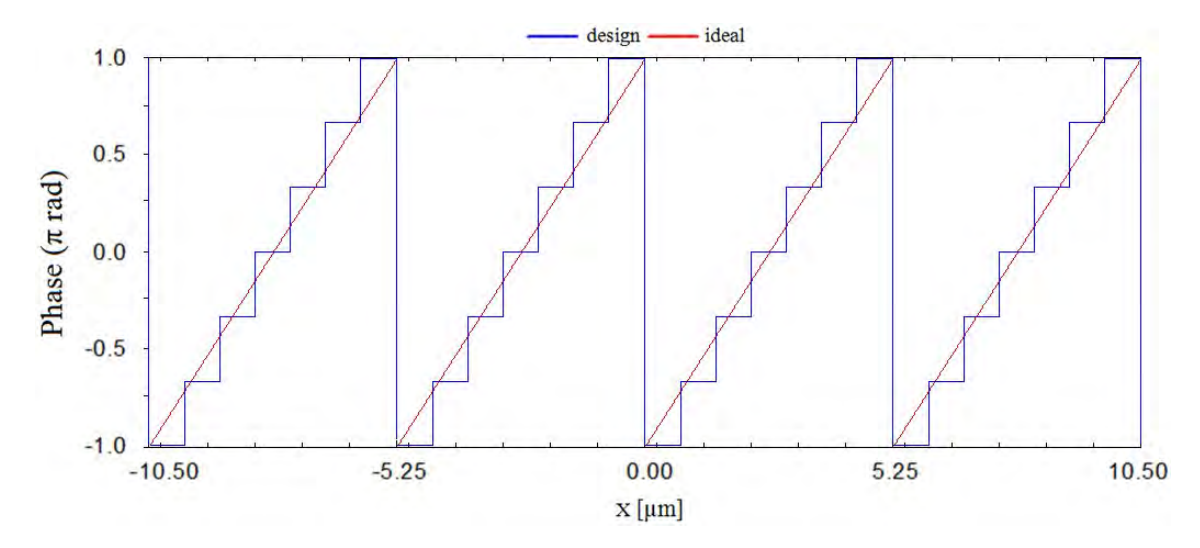


Figure 17 - Phase profile of the anomalous reflector, which depends on the position, periodically repeated, as for its responsible supercells.

Results about the performance of the metasurface can be seen in Figure 18. Since the incident wavelength, in practice, might not be exactly 1.55 μ m, it has been taken as interest to show the performance for a range of wavelengths varying from 1.4 to 1.7 μ m in steps of 0.05 μ m. As occurred for the refractor, slightly differences in the wavelength of the incident field will yield different phase profiles, due to the dependence of the α parameter with respect to λ_0 . That will impact in the reflection angle. Results for the metasurface containing structural errors, for the same wavelengths, can be seen in Chapter 4.

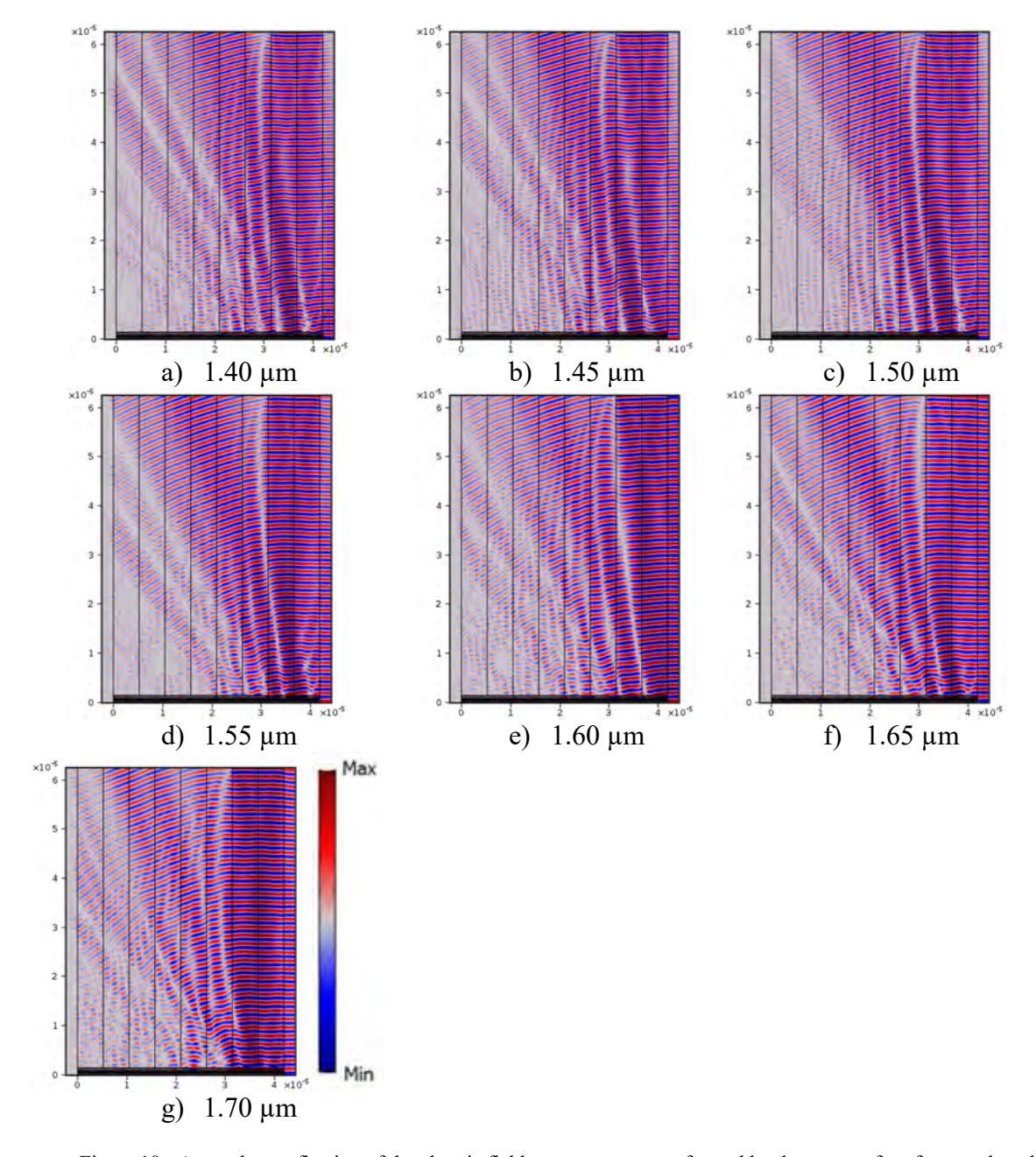


Figure 18 - Anomalous reflection of the electric field, x component, performed by the metasurface for wavelengths ranging from 1.4 to 1.7 μ m. Errors within the structure are not being considered.

The proposed model for anomalous reflector presented results greater than 0.94 of absolute value for the global phase range from $-\pi$ to π . Its level of reflection exceeds the one of metals. The model developed a reflection angle of 17.62° and successfully worked as an all-dielectric perfect mirror, due to the very high level of reflection.

Many efforts have been developed by the researchers since 2013 to develop and improve all-dielectric metasurface as anomalous reflectors [30 - 39].

In [30] it was developed a perfect dielectric metamaterial mirror based on silicon cubes mounted on SiO_2 substrate, with a thickness of 0.45 μ m through utilizing Mie resonances in dielectric particles. The metamaterial presented reflectivity over 99.999% and absorptivity smaller than 0.001% at 1.5 μ m. Conditions for permittivity and permeability are discussed to create the perfect reflector.

The perfect reflector based in [30] is, then, fabricated in [31], also based on Mie resonances, however utilizing cilindrical silicon resonators (instead of cubes) mounted on insulator substrate, as a wafer, following the conditions physical presented in [30]. The cylinders have height of 500 nm, diameter of 400 nm (yielding an aspect ratio of 1.25), periodicity of 660 nm. Possibilities of fabrication methods are discussed (nanosphere lithography).

In [32], large-scale metamaterials which idea was brought in [30, 31] to work as perfect mirrors are used for telecommunications band, fabricated in centimeter size. The utilized fabrication technique is nanosphere lithography and the built metamaterial is construction is highly tolerant to disorder. Results show maximum reflectance of 99.7% at 1530 nm. Silicon cylinder resonators are mounted on a SiO₂ layer of 2 µm, which is on a semi-infinite silicon substrate.

In [33], grating arrays of amorphous titanium dioxide (αTiO_2), mounted on glass ground plane, are utilized as high refractive index material for visible spectra, between 2.34 and 2.63. Perfect reflection occurs at 573 nm, 692 nm and 800 nm. The thickness of the ground plane is 400 nm. The αTiO_2 resonators have height of 180 nm, width of 280 nm and period of 560 nm.

Another perfect mirror for visible spectra is shown in [34], as a metasurface composed of TiO₂ cylinders array embedded in air, which dimensions can be adjusted to control the position of the perfect reflection band across the visible frequencies. Radius and height of the cylinders are, respectively, 100 and 150 nm. Lattice constant is 360 nm.

[35] shows the first demonstration of an optical magnetic mirror, in 2007, which required the use of metals. When an electromagnetic wave incides on the magnetic mirror, it transmits the electrical field, while it reverses the magnetic field. It works as a superconductor for optical frequencies.

In 2014 there was a substantial advance within magnetic mirrors: the experimental demonstration of the first all-dielectric magnetic mirror for optical frequencies [36]. Tellurium (Te) was employed as the resonator material, with high refractive index and low loss at infrared frequencies. Cubic-like tellurium dielectric resonators were used in two dimensional array mounted on a BaF₂ substrate (n \sim 1.4). The height of the resonators is 1.7 μ m and the base is 1.5 μ m x 1.5 μ m. Fabrication technique was e-beam lithography.

A multi-purpose terahertz all-dielectric metasurface is shown in [37]. Cubic silicon resonators are mounted on a SiO₂. The resonators can support both electric and magnetic Mie resonances and the tailoring of the interference between the two modes allows the control of the amplitude and phase of the reflected wave. Reflected beams include Bessel beams and vortex. This metasurface also works as a magnetic mirror in terahertz band. The fabrication process is described for the silicon magnetic mirror.

A tunable all-dielectric metasurface capable of switching between a high transmitter and a high reflector device through changing the linear polarization of the excitation is shown in [38]. The metasurface consists in Si nanodimers disks on sapphire substrate. Fabrication required the use of electron beam lithography and reactive ion etching. The Si disks have diameter of 652 nm and height of 314 nm. Periodicity along the dimer axis is 1544 nm and 852 nm perpendicular to the axis. Results for $\lambda = 1688$ nm include transmission of 99% and reflection of 95% when polarization state is changed from TM to TE. For $\lambda = 1718$ nm the results were transmission of 86% and reflection of 77%.

Another tunable all-dielectric nanograting metasurface is shown in [39]. The change between transmitter and reflector occurs laser-induced structural transitions for the visible and near infrared spectra. Amorphous germanium antimony telluride is mounted on silica substrate.

3.4 METALENS

The next proposed model is an all-dielectric metalens [27] which, such as the anomalous refractor and reflector, was designed utilizing square blocks with contrasting refractive indexes materials. It has been planned to perform focusing of infrared waves, 1550 nm. As a kind of metasurface, metalenses are also built with phase shifting elements which spacing is smaller than the wavelength's [40], necessary to overcome thin-film and diffractive optics.

Differently of the previous models, in which the wavefront shaping bended the incident planar wave into another planar wave, now the incident planar wave is shaped into spherical. The considered focal distance for the metalens, f, is a multiple of the operation wavelength, chosen to be 3.5 times the operation wavelength. For $\lambda_0 = 1550$ nm, the desired focal distance is 5425 nm.

The phase profile φ_L is now quadratic, function of x and y according to $\varphi_L(x,y) = \frac{2\pi}{\lambda} \left(\sqrt{x^2 + y^2 + f^2} - f \right)$, equation (2.7).

The same pattern of ABA type of unit cell employed for the anomalous refractor is used for the metalens, shown in Figure 19. The refractive index of the employed materials, considering the wavelength of 1550 nm, is 3.4757 for Si and 1 for air.

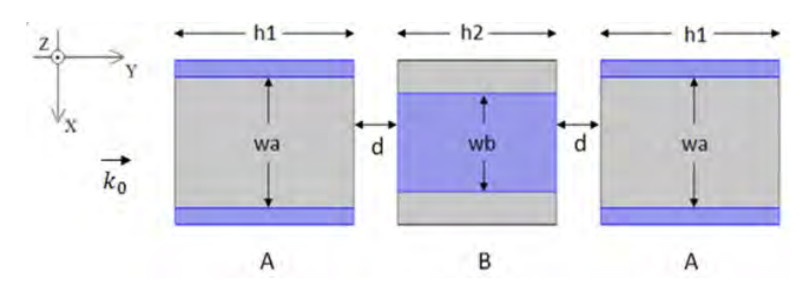


Figure 19 - Unit cell of the metalens. Employed materials are Air, in gray, and Si, in blue. External dimensions are h1 = 300 nm, h2 = 250 nm and d = 50 nm. Internal dimensions w_a and w_b are swept from 20 up to 230 nm. Incident electrical field is polarized in x direction. The space among the blocks is filled with air.

From the unit cell, the absolute value and phase maps for the transmission coefficient are generated. These are the same maps the created for the anomalous refractor, which is expected, due to using the same unit cell of it. Consult Figures 6 and 7.

A corresponding table of values, which came from Figures 6 and 7, was obtained considering those pairs of values for w_a , w_b that were found to be more adequate for the unit cells to attend to global phase control along with high transmission that followed the quadratic phase profile planned for the metasurface. The smallest number of different pair values that sufficed the aforementioned conditions was 11, which stands for 11 differently fulfilled terms of unit cells – the angle steps of the discretized phase profile that cause the phase shifts on the electric field as it traverses the metasurface. These values are enlisted in Table 3.3:

TABLE 3.3 GEOMETRIC PARAMETERS OF THE UNIT CELL				
Cell / Param.	w_a	w_b		
1	211.47	50.88		
2	20	230		
3	20	143.53		
4	50.88	149.71		
5	174.41	211.47		
6	20	217.65		
7	32.35	69.41		
8	186.76	192.94		
9	20	168.24		
10	118.82	211.47		
11	217.65	75.58		

Table 3.3 - Geometric Parameter values for the pairs (w_a, w_b) , in nm, for each angle step of the supercell of the metalens.

It is already known from the refractor that high transmission values and global phase control were successfully obtained and that occurs to the metalens, as well. The determinant difference is in the quadratic phase profile that the metalens has to pursue, which is aperiodic.

Since the structure of the metalens is symmetric with respect to its center and it is very long, one half of it is shown in Figure 20, with a mirror mark.

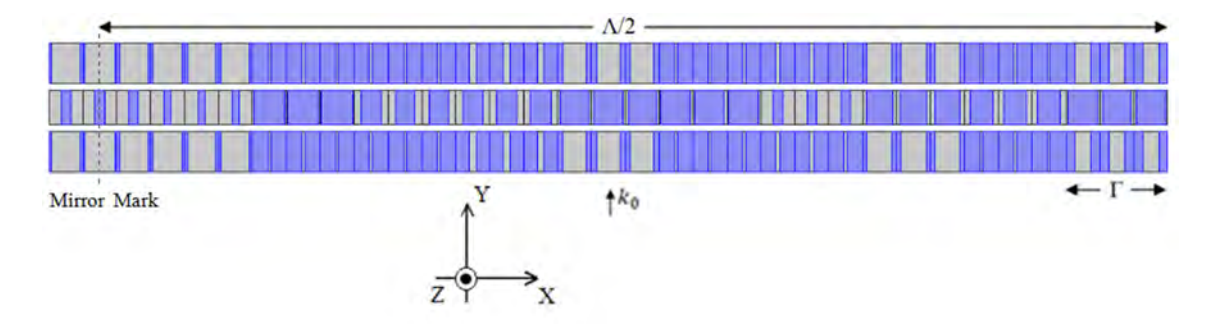


Figure 20 - Mirrored structure of the metalens (half of its structure). composed by Si, in blue, and air, in gray. Basic dimensions are the angle step $\Gamma=750\,$ nm. The total length is $\Lambda=17250\,$ nm.

The phase profile, function of the position x, infinitely extends to the sides, as shown in Figure 21 in red. It was necessary, then, to simulate the structure for a number of angle steps that would properly discretize the ideal profile of the model. That implied in 23 angle steps, shown in blue, which makes 69 unit cells. As the profile extends to the sides, it only gets narrower, making it more difficult to reproduce it due to the angle step dimension of 750 nm. For convenience, Figure 21 shows the center of the phase profile as zero, while its position x varies negatively to the left and positively to the right.

Figure 21 shows the phase profile of the metalens, ideally considered to be a quadratic function of the position, x, of the structure. It has been designed approximately as successive angle steps that approximate the ideal quadratic function that is continuously shown in the Figure 21, in red, making it possible to concentrate the incident field in the designed focal plane of 3.5 times lambda, 5425 nm, of distance to the point where the wave starts interacting with the metasurface.

It can be noticed in Figure 21 that, unlike the previous structures, since the phase profile is no longer periodic, the structure will not be as well. The phase profile has an infinite quadratic form, so it is necessary to choose how far the structure will reproduce it, in fact. This choice is bounded by the width of angle steps because the real angle steps have non null width, which is 750 nm, and it gets more and more difficult to reproduce the phase profile as x increases, due to the corresponding fast growing increments in its phase, which leads to a poor discretization of the phase profile while x increases. According to these conditions, the maximum value of x was

chosen to be 8625 nm, which means the whole structure has 17250 nm or 69 unit cells or 23 angle steps.

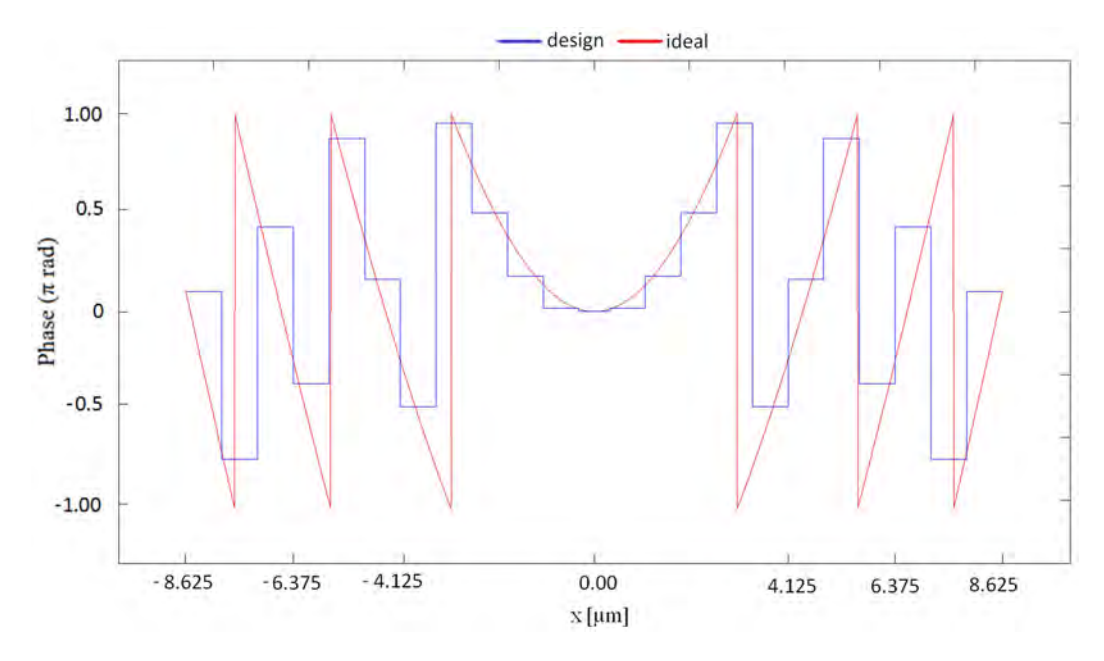


Figure 21 – Ideal phase profile of the metalens, in red, approximated by 23 angle steps of 3 unit cells each, in blue.

The built structure was, then simulated for the power density of the electromagnetic wave, given by the normalized Poynting vector, over the range from 1.4 to 1.7 μm , shown in Figure 22:

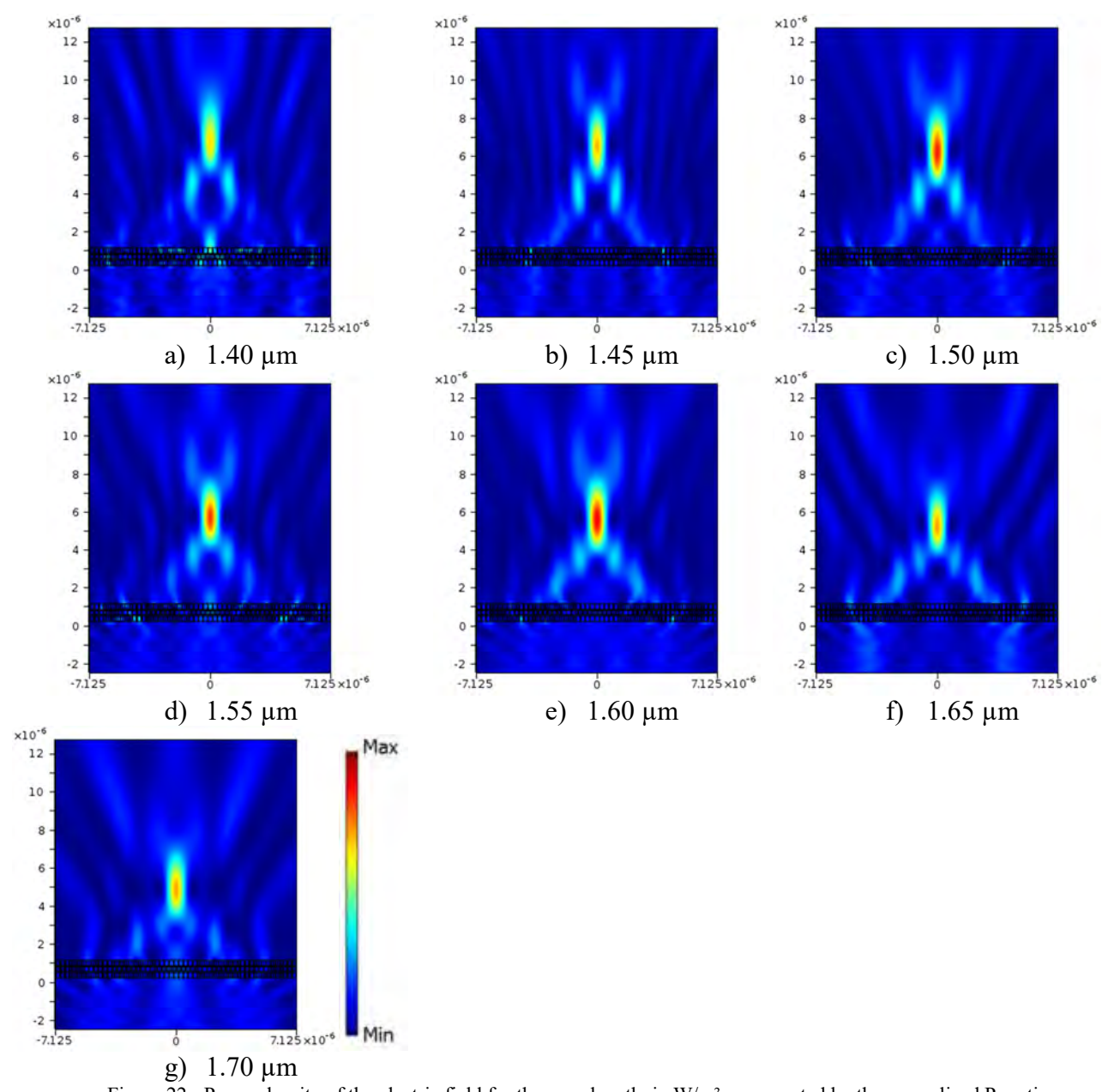


Figure 22 - Power density of the electric field for the wavelength, in W/m², represented by the normalized Poynting vector of the EMW, varying around 1550 nm, ranging from 1400 to 1700 nm. The focus of the metalens coincides with its focal plane, that has the following values: a) 6550 nm; b) 6350 nm; c) 5950 nm; d) 5500 nm; e) 5400 nm; f) 5050 nm; g) 4700 nm.

Figure 22 illustrates the capacity of concentrating the electric field as close as possible to the focal plane by showing the power density of the field. For the operation wavelength of 1550 nm, a small divergence of (1.37%) was found through the comparison with the desired focal plane of 5425 nm. The highest positive (above the desired focal plane) deviation found was 1125 nm, 20.7%, which occurred for the

wavelength of 1600 nm. The highest negative deviation to the designed focal plane was -725 nm, 13.4%, occurred at the wavelength of 1700 nm.

Efforts towards the proposal, design, manufacturing and testing of all-dielectric metalenses have been made in [41]. Examples on the development of these very low-loss lenses can be seen in [41 - 45].

Chapter 4 includes simulations that consider geometry errors within the structure for a more practical approach.

4 PERFORMANCE ANALYSIS OF THE DEVICES CONSIDERING GEOMETRY ERRORS

4.1 INTRODUCTION

In order to approximate the models to the real world performance, a primary step is to consider the insertion of geometry errors all over it. These geometry errors [46] mean how each part of the structure was built thinner or larger than the expected. The chosen philosophy to do so implies the inclusion of an error parameter, in length, that makes larger or thinner each inner square of the structure, depending on negative or positive errors, respectively. This was done over the structure of the models, by modifying the parameters w_a and w_b .

Ten structures were supposed to be generated for each proposed model, according to each error value in the set: $\{-10, -8, -6, -4, -2, 2, 4, 6, 8, 10\}$. Since both w_a , w_b start from 20 nm, the software didn't allow to diminish more than 8 nm from the inner squares and the set was, then, diminished to be eight structural errors, in nm, $\{-8, -6, -4, -2, 2, 4, 6, 8\}$.

For each considered wavelength in the range from 1.4 to 1.7 μ m, in steps of 0.05 μ m, the performance for the eight considered errors is shown next. Negative values of geometry errors cause the dimensions w_a and w_b to become thinner and positive values yield these dimensions to become wider.

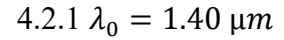
Even though, in reality, a different error would occur for each square, the chosen method was considered to be accurate enough due to the many error possibilities that it brings to the structure. A real world structure, when simulated, can be considered as having and effective error, which will be, approximately, the closest as possible to one of the simulated errors within the set.

The transmission and the reflection angle were obtained from the calculation of the Poynting vector angle using the x and y components of the vector to calculate its arctangent and then subtracting pi/2 rad (so that the angle would be referenced to the normal line to the metasurface), yielding:

$$\theta = \tan^{-1} \frac{S_y}{S_x} - \frac{\pi}{2} \tag{4.1}$$

4.2 EFFECTS OF GEOMETRY ERRORS IN THE ANOMALOUS REFRACTOR

The effect of geometry errors all over the structure of the anomalous refractor is expected to deviate the transmission angle from the ideal, which performance can be seen at the end of section 3.1. Sub-sections 4.2.1 to 4.2.7 show the performance of the device as its structure is afflicted by errors within each considered wavelength.



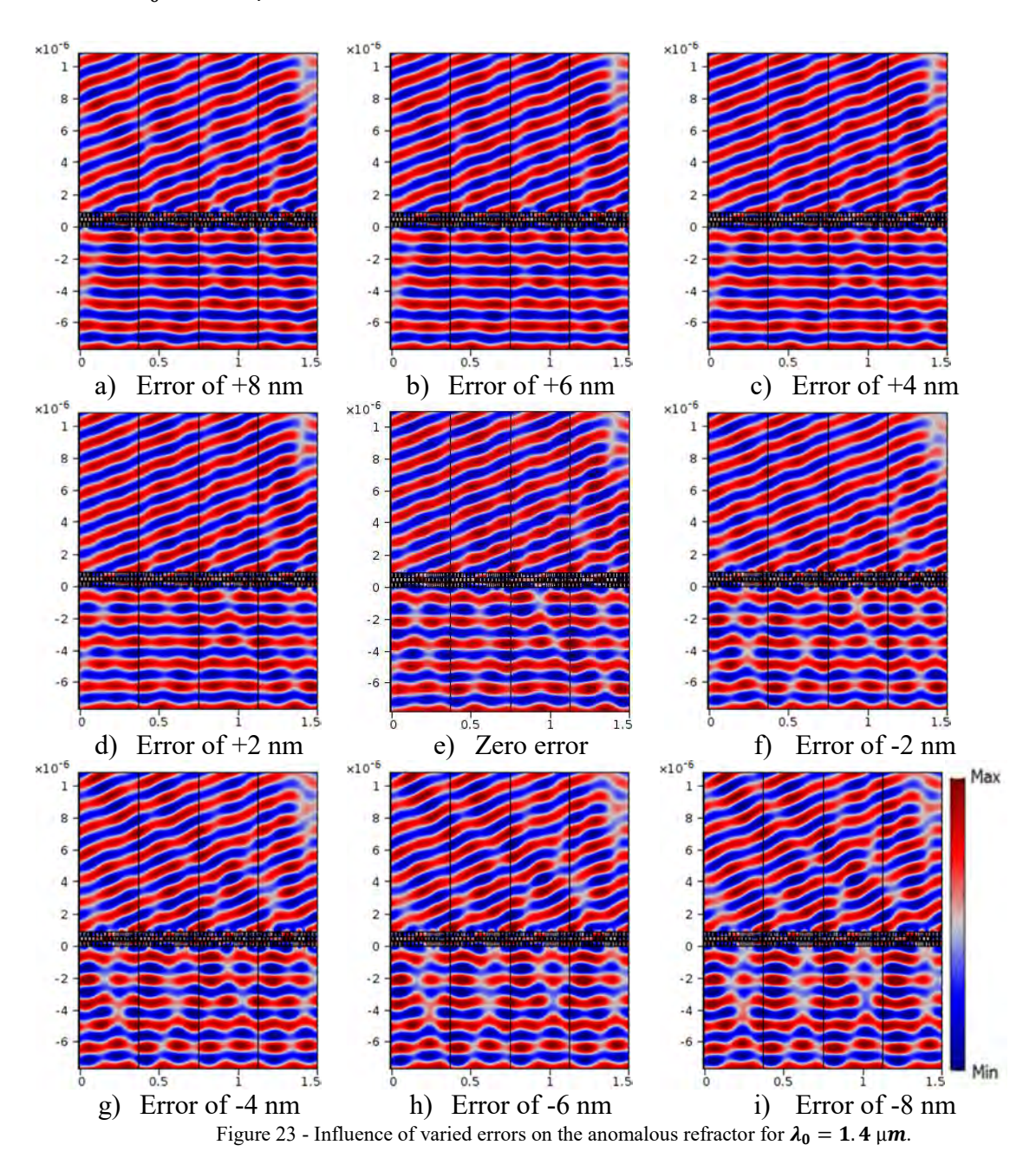


Figure 23 shows, in a qualitative form, the refraction occurring for the wavelength of 1.4 μ m, considering the geometry error range in the pair (w_a, w_b) from - 8 to 8 nm in steps of 2 nm.

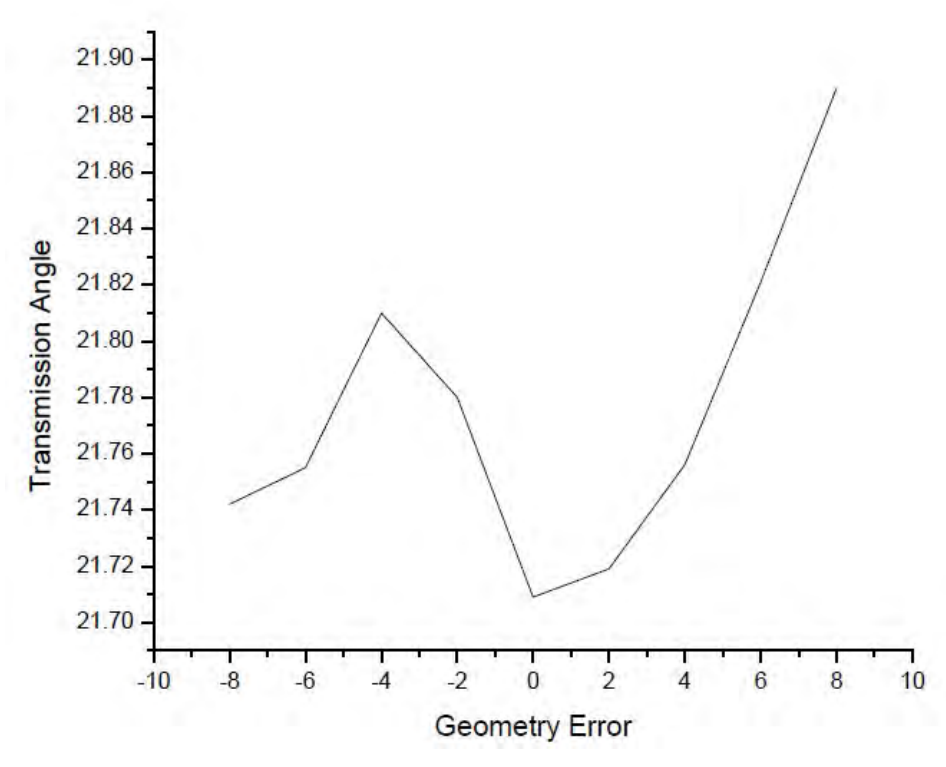
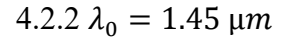


Figure 24 - Analysis of the transmission angle θ_t as geometry errors are inserted in the supercell for the wavelength of 1.4 μm .

To complement the results shown for the wave propagation of Figure 23, it is shown in Figure 24 how the transmission angle, θ_t , varies from the designed angle of 25° for the wavelength of 1.4 μ m, along with the geometry errors. The wavelength of 1.4 μ m has a considerable influence in deviating θ_t in approximately -2.46°. The geometry errors among -8 μ m and +8 μ m increase the error in, respectively, +0.03° and +0.18°, approximately, related to the zero error condition (21.71°).



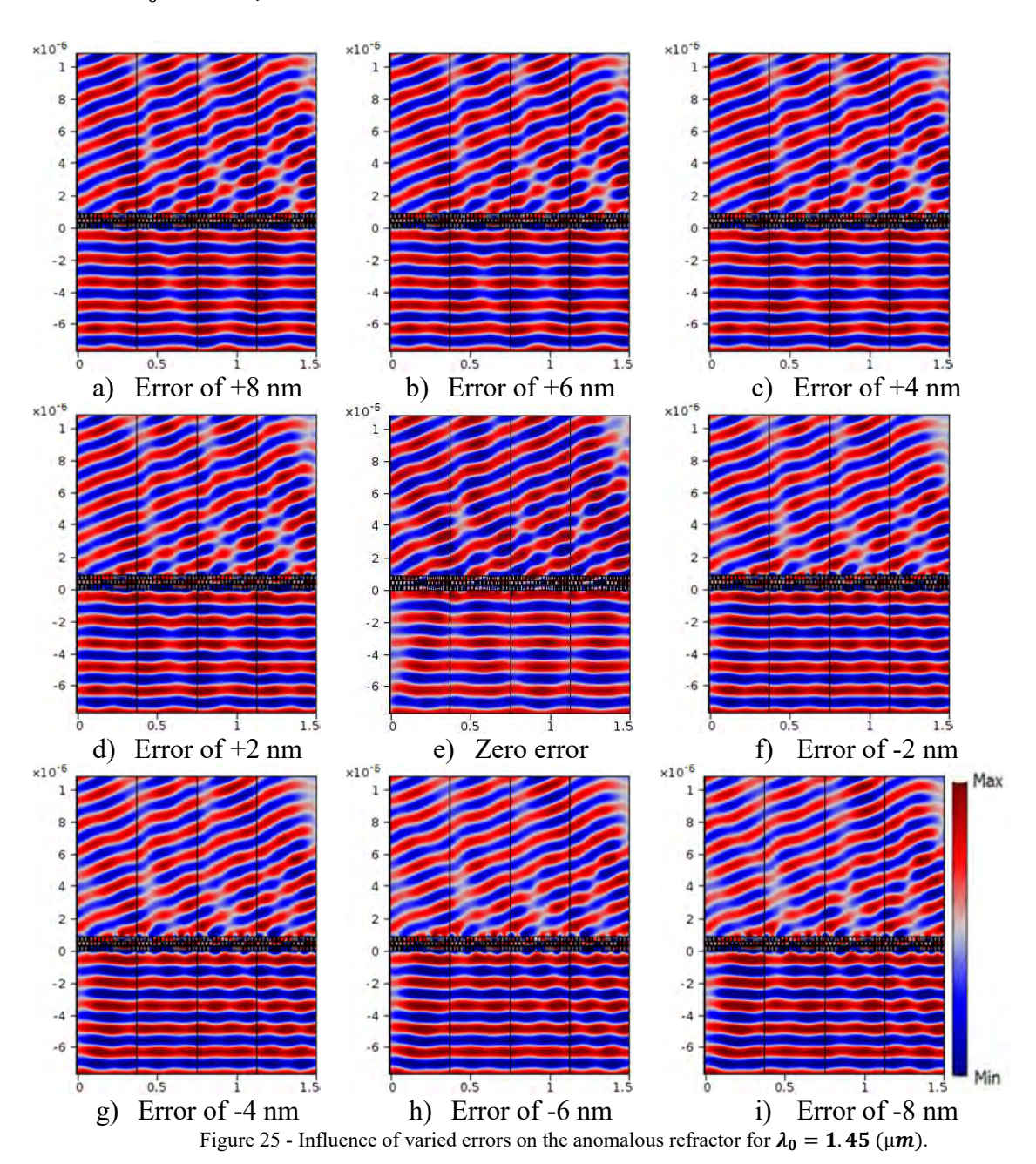


Figure 25 shows, in a qualitative form, the refraction occurring for the wavelength of 1.45 μ m, considering the geometry error range in the pair (w_a, w_b) from -8 to 8 nm in steps of 2 nm.

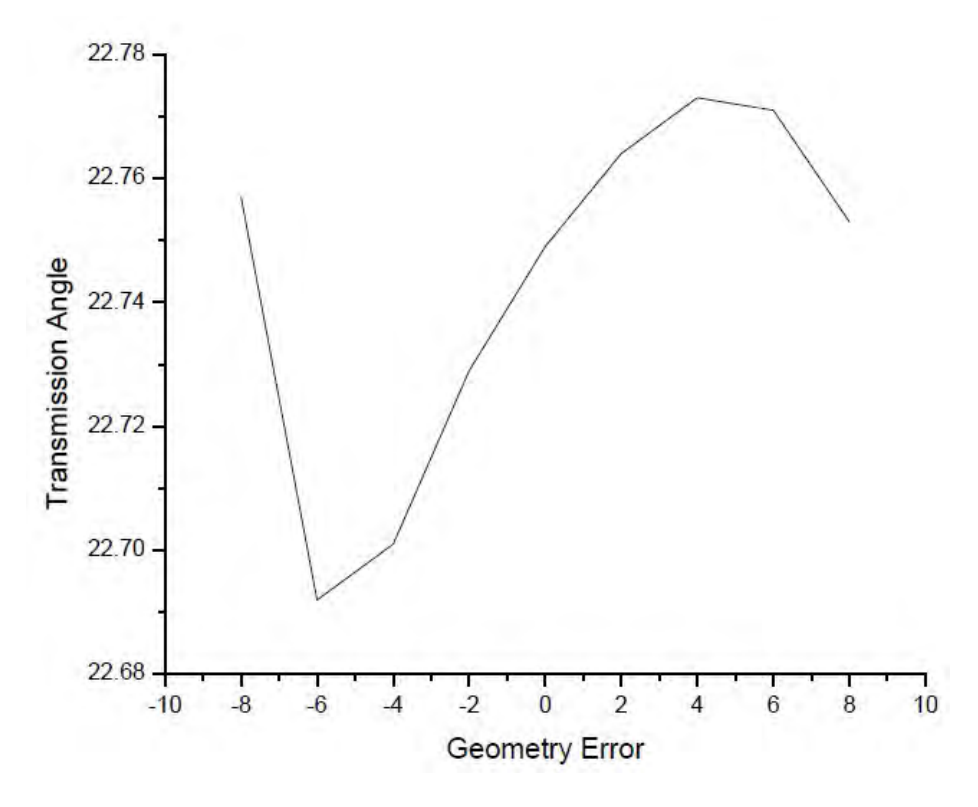
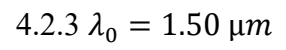


Figure 26 – Analysis of the transmission angle θ_t as geometry errors are inserted in the supercell for the wavelength of 1.45 μm .

To complement the results shown for the wave propagation of Figure 25, it is shown in Figure 26 how the transmission angle, θ_t , varies from the designed angle of 25° for the wavelength of 1.45 (μ m), along with the geometry errors. The wavelength of 1.45 μ m has a reasonable influence in deviating θ_t in approximately -1.42°. The geometry errors among -8 μ m and +8 μ m increase the error in, respectively, +0.01° and +0.01°, approximately, related to the zero error condition (22.75°).



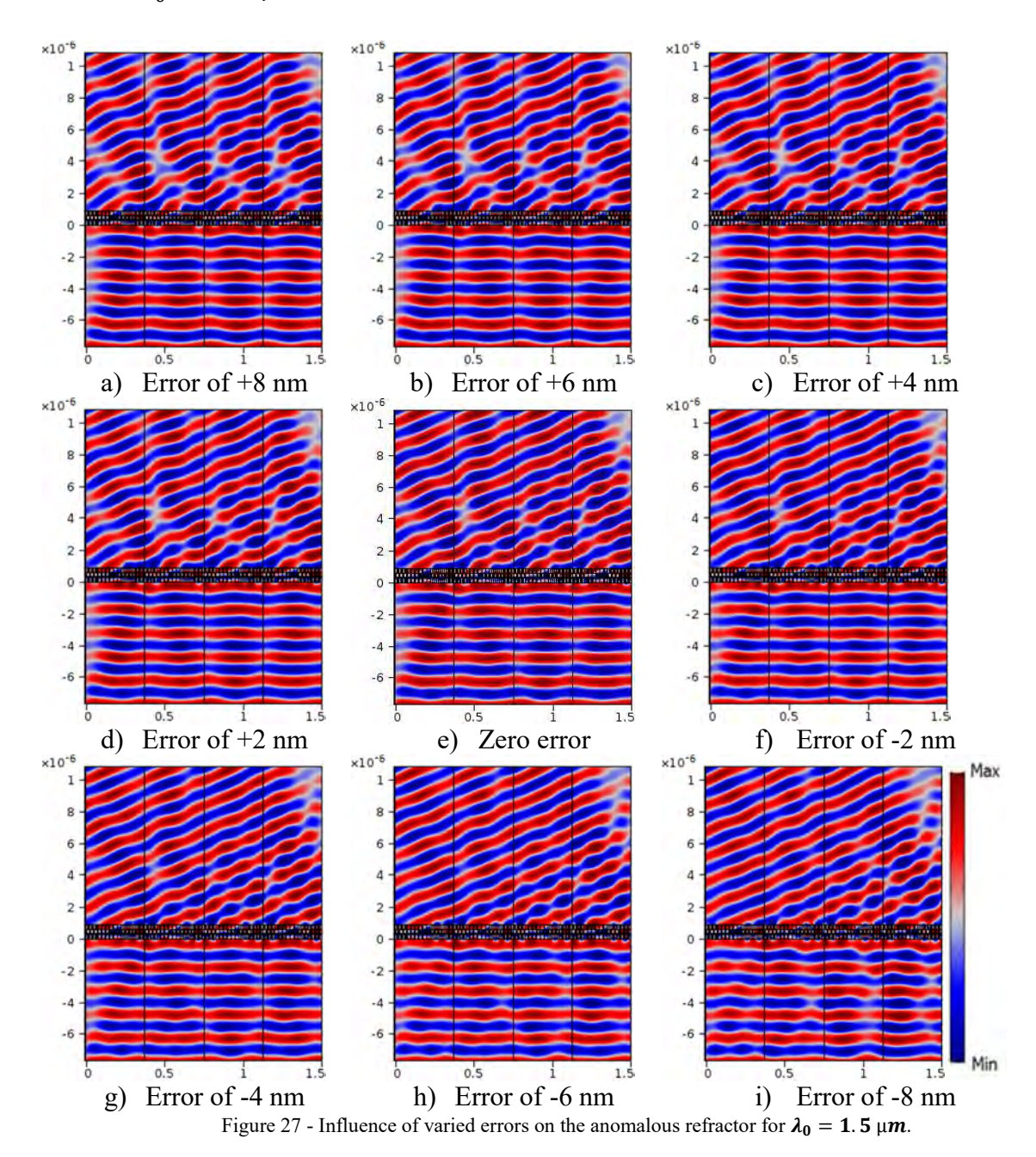


Figure 27 shows, in a qualitative form, the refraction occurring for the wavelength of 1.5 μ m, considering the geometry error range in the pair (w_a, w_b) from - 8 to 8 nm in steps of 2 nm.

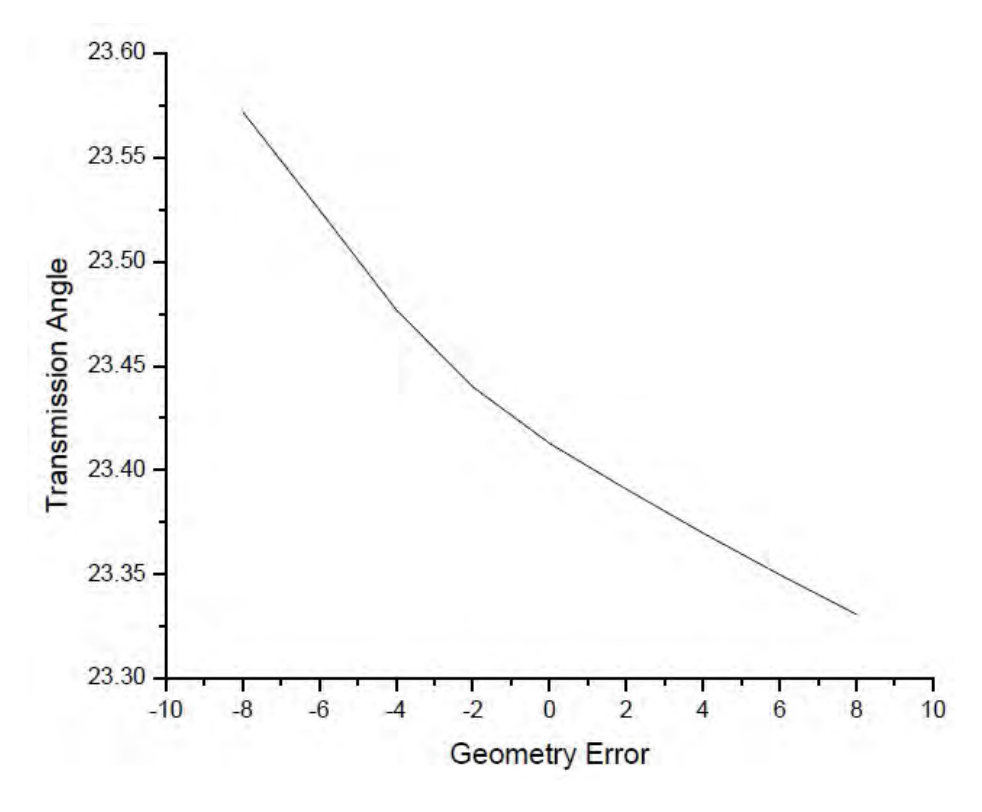
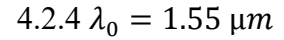


Figure 28 - Analysis of the transmission angle θ_t as geometry errors are inserted in the supercell for the wavelength of 1.5 μm .

To complement the results shown for the wave propagation of Figure 27, it is shown in Figure 28 how the transmission angle, θ_t , varies from the designed angle of 25° for the wavelength of 1.5 μ m, along with the geometry errors. The wavelength of 1.5 μ m has a reasonable influence in deviating θ_t in approximately -0.75°. The geometry errors among -8 μ m and +8 μ m increase the error in +0.15° and -0.10°, approximately, related to the zero error condition (23.42°).



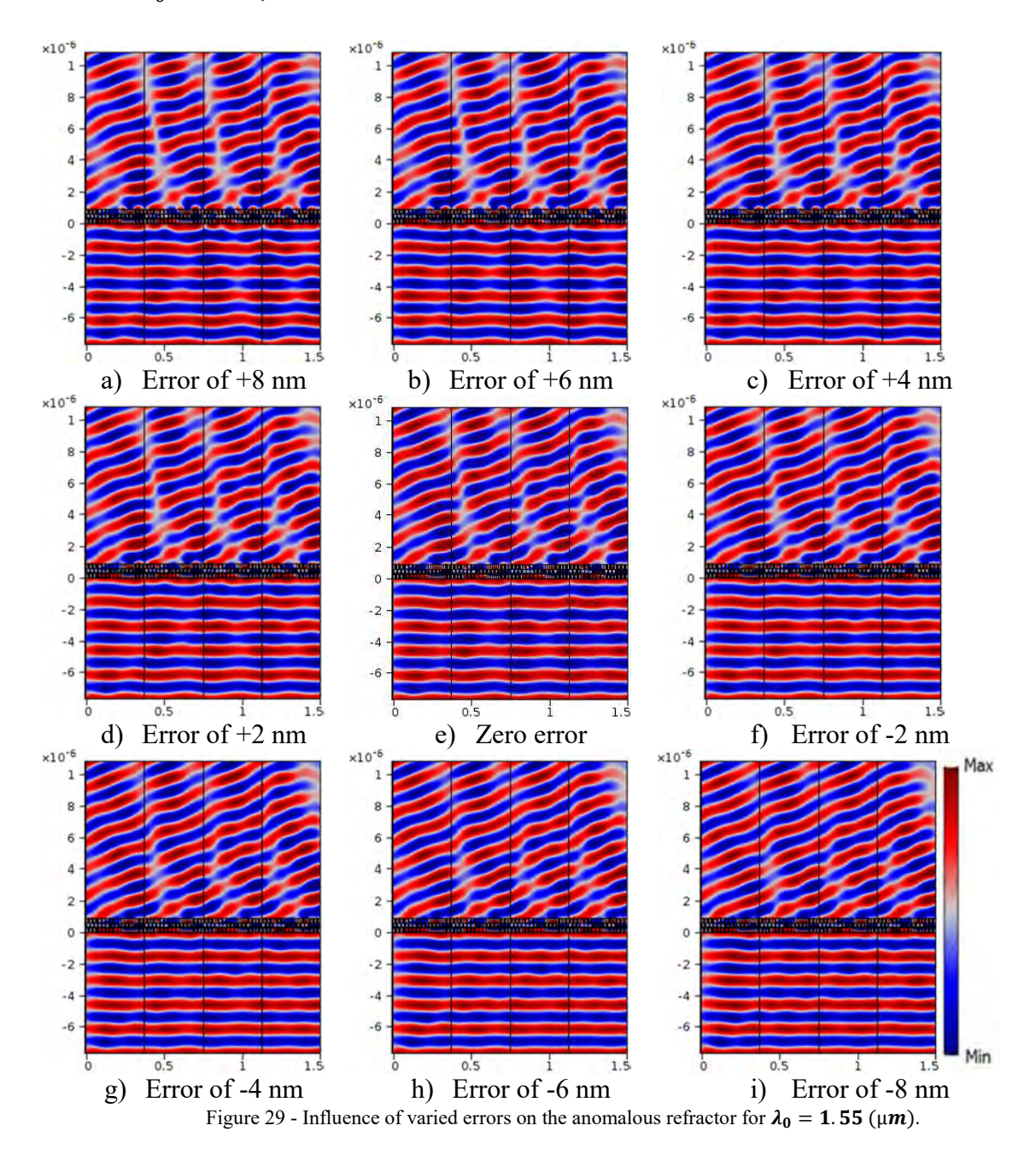


Figure 29 shows, in a qualitative form, the refraction occurring for the wavelength of 1.55 μ m, considering the geometry error range in the pair (w_a, w_b) from -8 to 8 nm in steps of 2 nm.

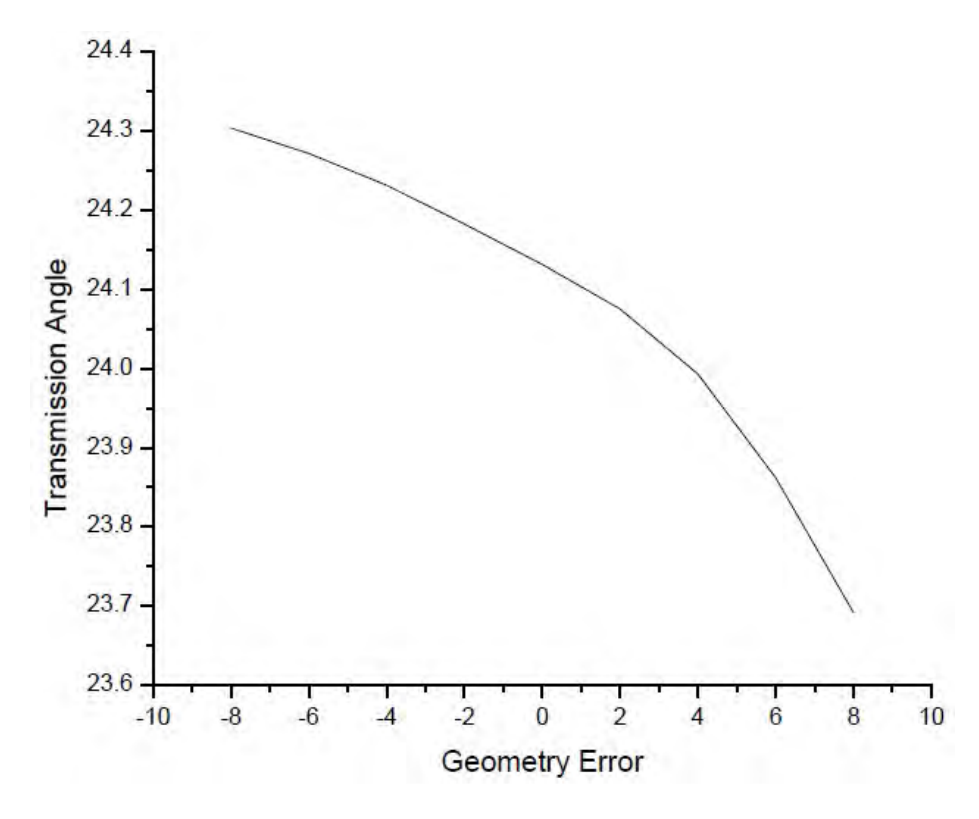


Figure 30 - Analysis of the transmission angle θ_t as geometry errors are inserted in the supercell for the wavelength of 1.55 μm .

To complement the results shown for the wave propagation of Figure 29, it is shown in Figure 30 how the transmission angle, θ_t , varies from the designed angle of 25° for the wavelength of 1.55 μ m, along with the geometry errors. The wavelength of 1.55 μ m has an insignificant influence in deviating θ_t in approximately 0.02°. The geometry errors among -8 μ m and +8 μ m increase reasonably the error in +0.15° and -0.45°, approximately, related to the zero error condition (24.15°).

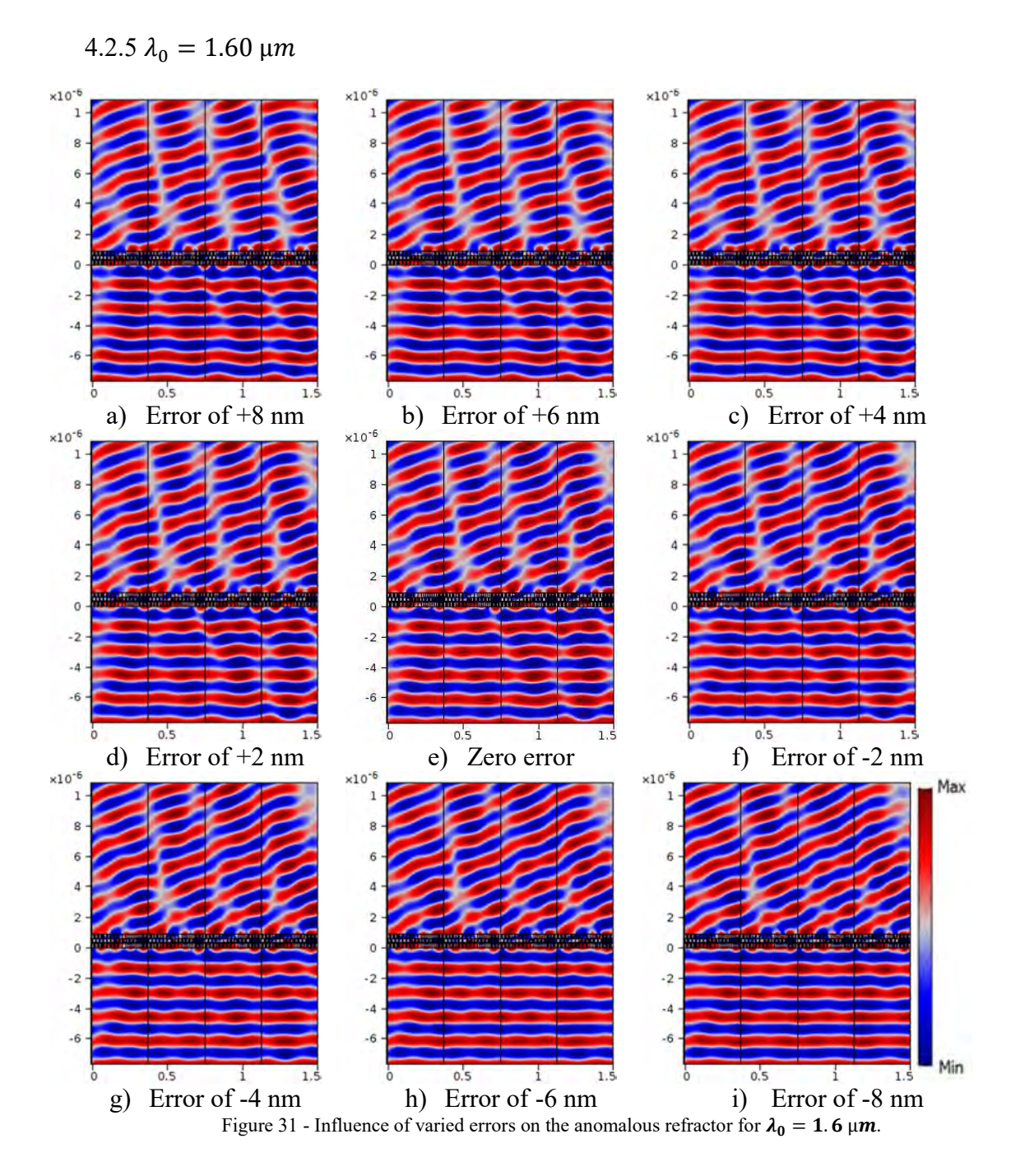


Figure 31 shows, in a qualitative form, the refraction occurring for the wavelength of 1.6 μ m, considering the geometry error range in the pair (w_a, w_b) from - 8 to 8 nm in steps of 2 nm.

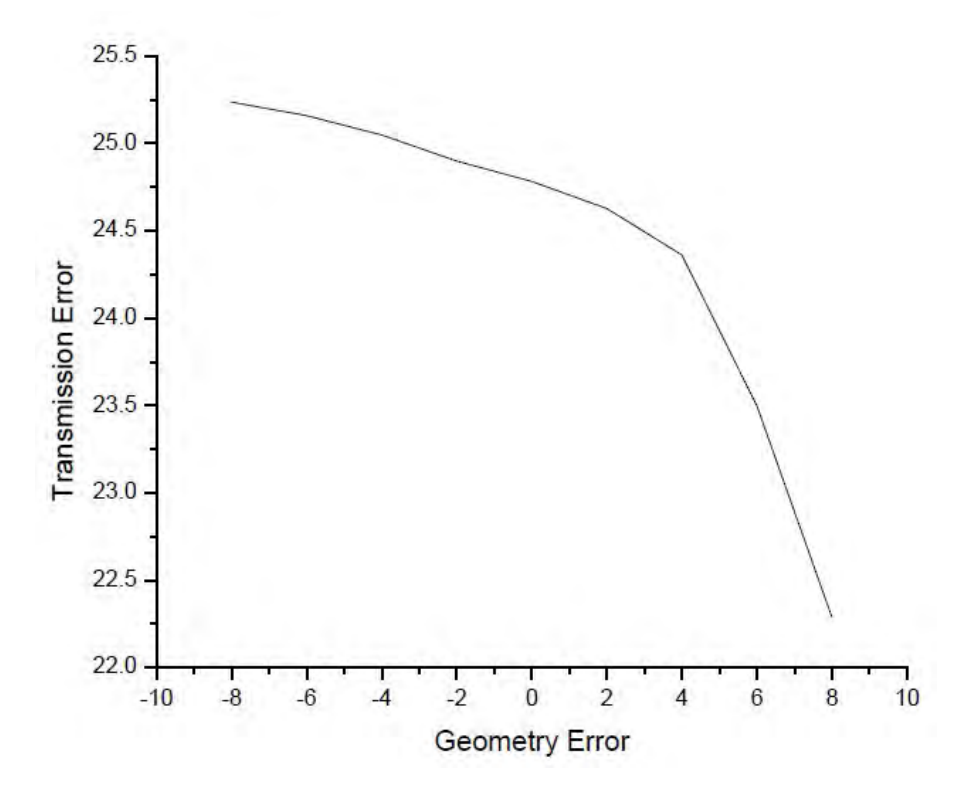


Figure 32 - Analysis of the transmission angle θ_t as geometry errors are inserted in the supercell for the wavelength of 1.60 μm .

To complement the results shown for the wave propagation of Figure 31, it is shown in Figure 32 how the transmission angle, θ_t , varies from the designed angle of 25° for the wavelength of 1.6 μ m, along with the geometry errors. The wavelength of 1.6 μ m has a small influence in deviating θ_t in approximately +0.63°. The geometry errors among -8 μ m and +8 μ m increase substantially the error in +0.45° and -2.5°, approximately, related to the zero error condition (24.8°).

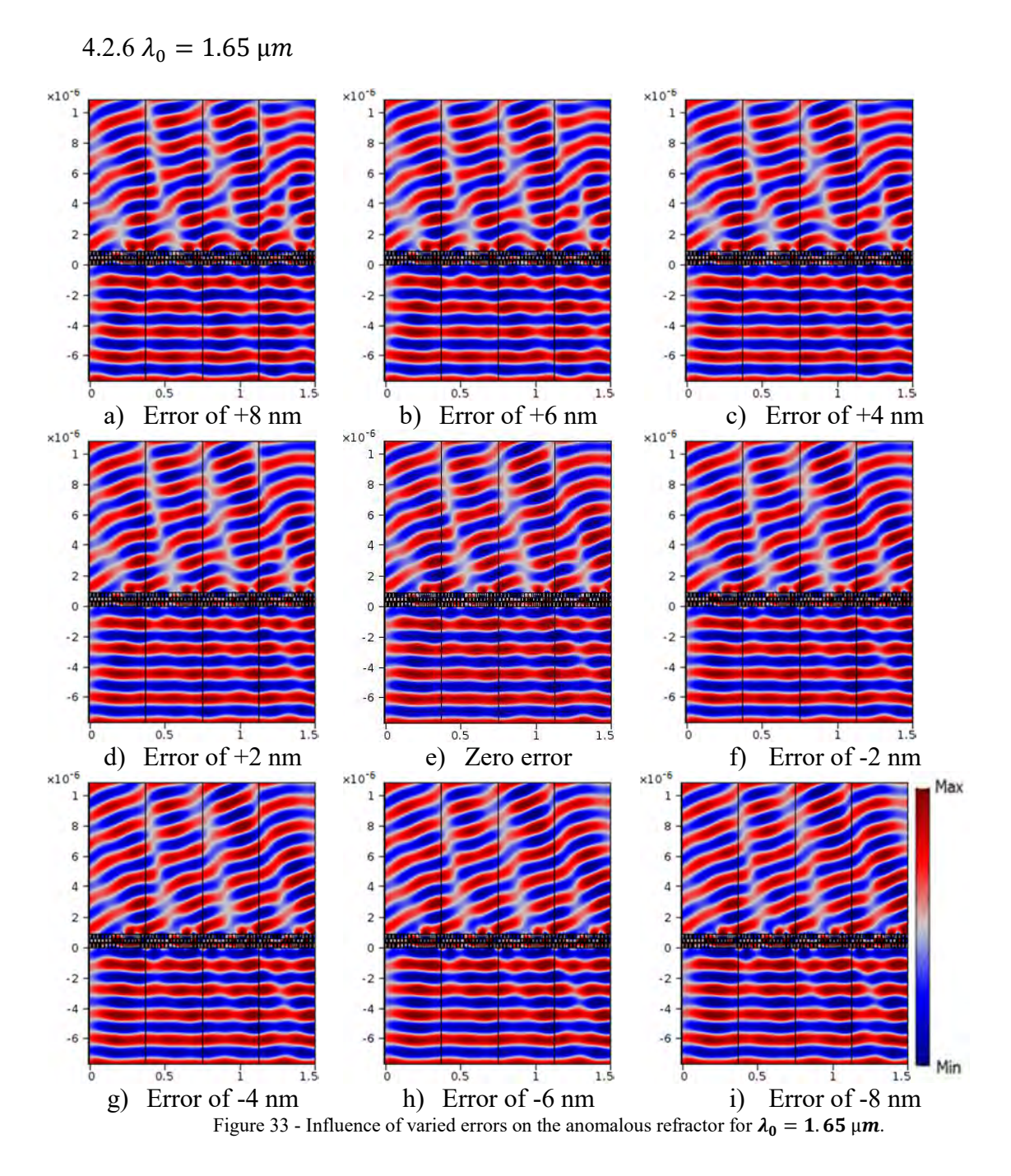


Figure 33 shows, in a qualitative form, the refraction occurring for the wavelength of 1.65 μ m, considering the geometry error range in the pair (w_a, w_b) from -8 to 8 nm in steps of 2 nm.

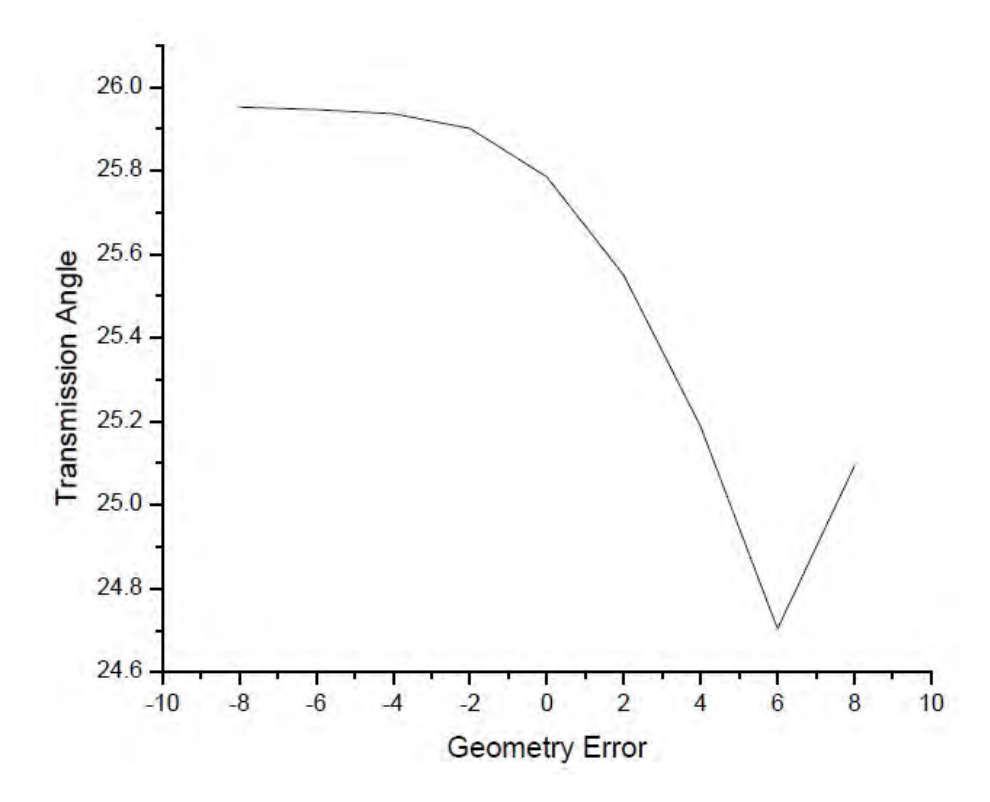


Figure 34 - Analysis of the transmission angle θ_t as geometry errors are inserted in the supercell for the wavelength of 1.65 μm .

To complement the results shown for the wave propagation of Figure 33, it is shown in Figure 34 how the transmission angle, θ_t , varies from the designed angle of 25° for the wavelength of 1.65 μ m, along with the geometry errors. The wavelength of 1.65 μ m has a small influence in deviating θ_t in approximately +0.8°. The geometry errors among -8 μ m and +8 μ m increasing meaninglessly the error in +0.15° and -0.50°, approximately, related to the zero error condition (25.8°).

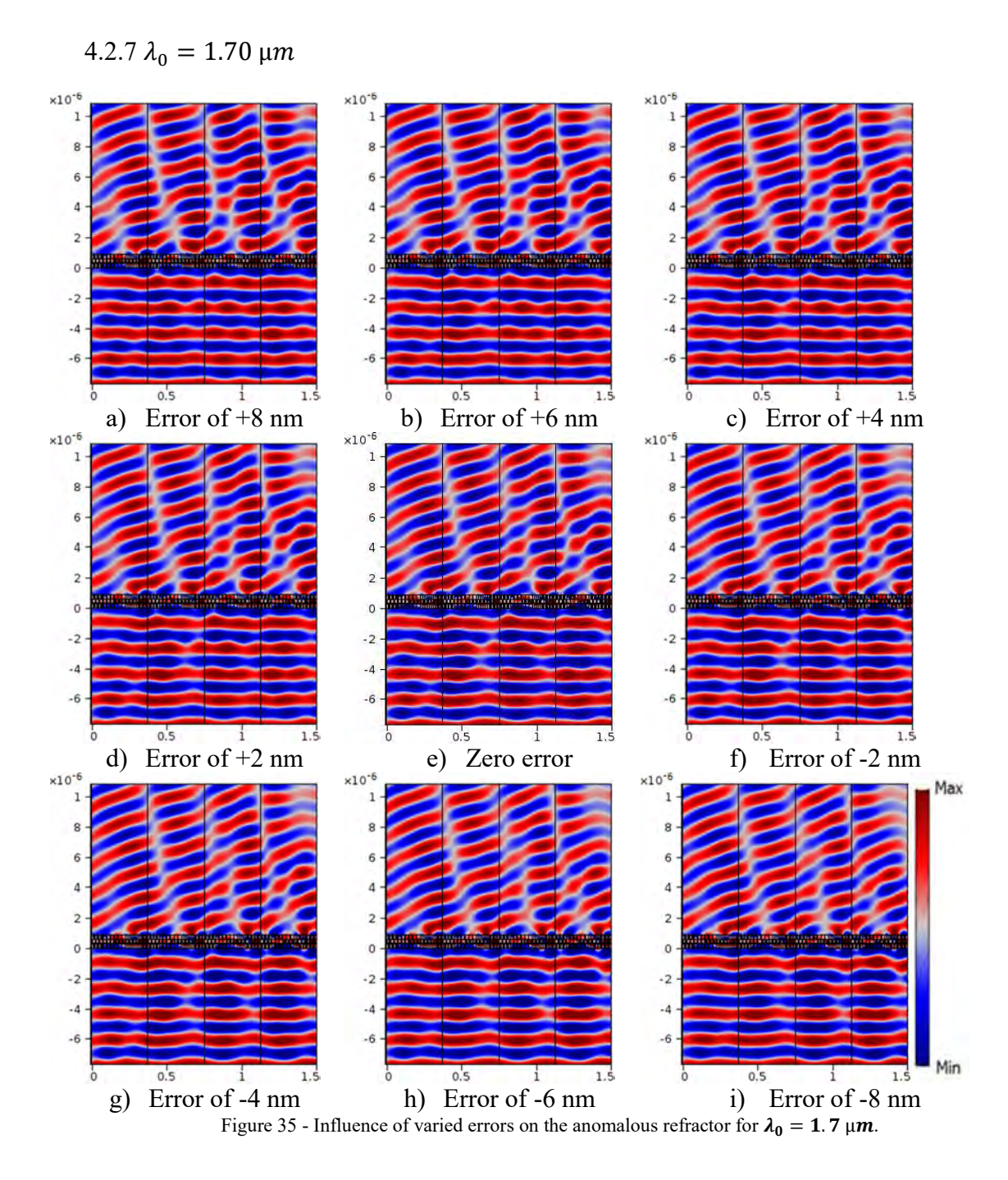


Figure 35 shows, in a qualitative form, the refraction occurring for the wavelength of 1.7 μ m, considering the geometry error range in the pair (w_a, w_b) from - 8 to 8 nm in steps of 2 nm.

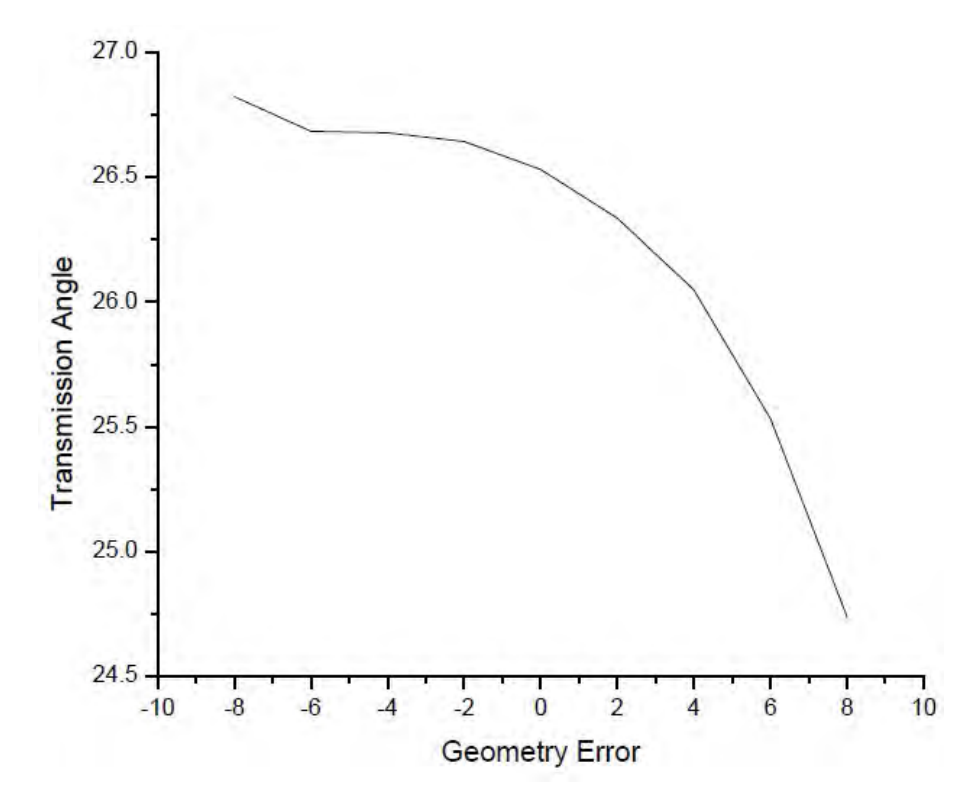


Figure 36 - Analysis of the transmission angle θ_t as geometry errors are inserted in the supercell for the wavelength of 1.7 μ m.

To complement the results shown for the wave propagation of Figure 35, it is shown in Figure 36 how the transmission angle, θ_t , varies from the designed angle of 25° for the wavelength of 1.7 μ m, along with the geometry errors. The wavelength of 1.7 μ m has a small influence in deviating θ_t in approximately +1.5°. The geometry errors among -8 μ m and +8 μ m increasing substantially the error in +0.2° and -1.85°, approximately, related to the zero error condition (26.6°).

4.3 EFFECTS OF GEOMETRY ERRORS IN THE ANOMALOUS REFLECTOR

The effects of geometry errors in the parameters w_a , w_b all over the structure of the anomalous refractor and reflector are expected to deviate both from the ideal performance by affecting the transmission and reflection angle, respectively. Sections 4.3.1 to 4.3.7 show the results of the error insertions for each wavelength.

$$4.3.1 \lambda_0 = 1.40 \ \mu m$$

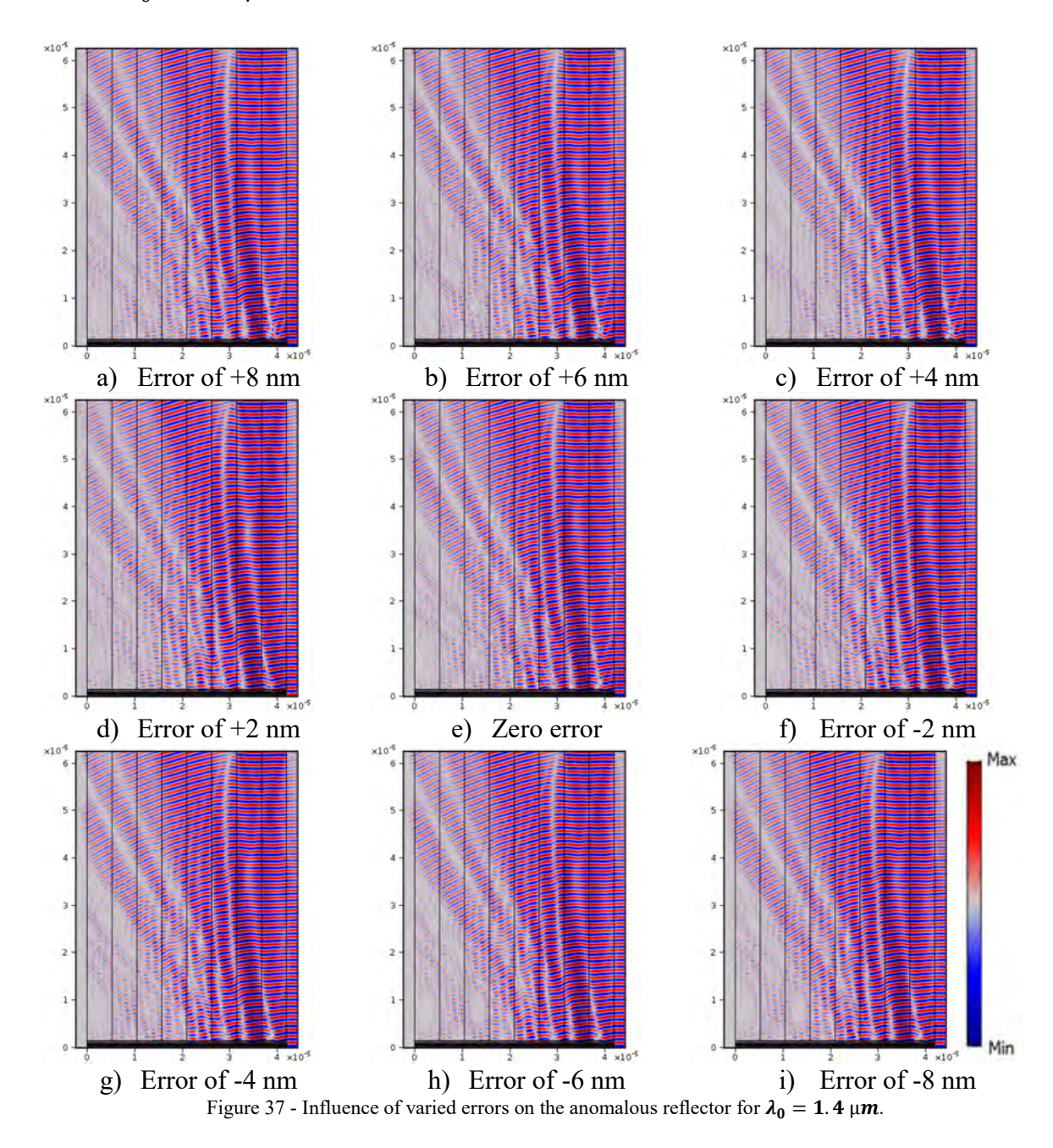


Figure 37 shows, in a qualitative form, the reflection occurring for the wavelength of 1.4 μ m, considering the geometry error range in the pair (w_a, w_b) from - 8 to 8 nm in steps of 2 nm.

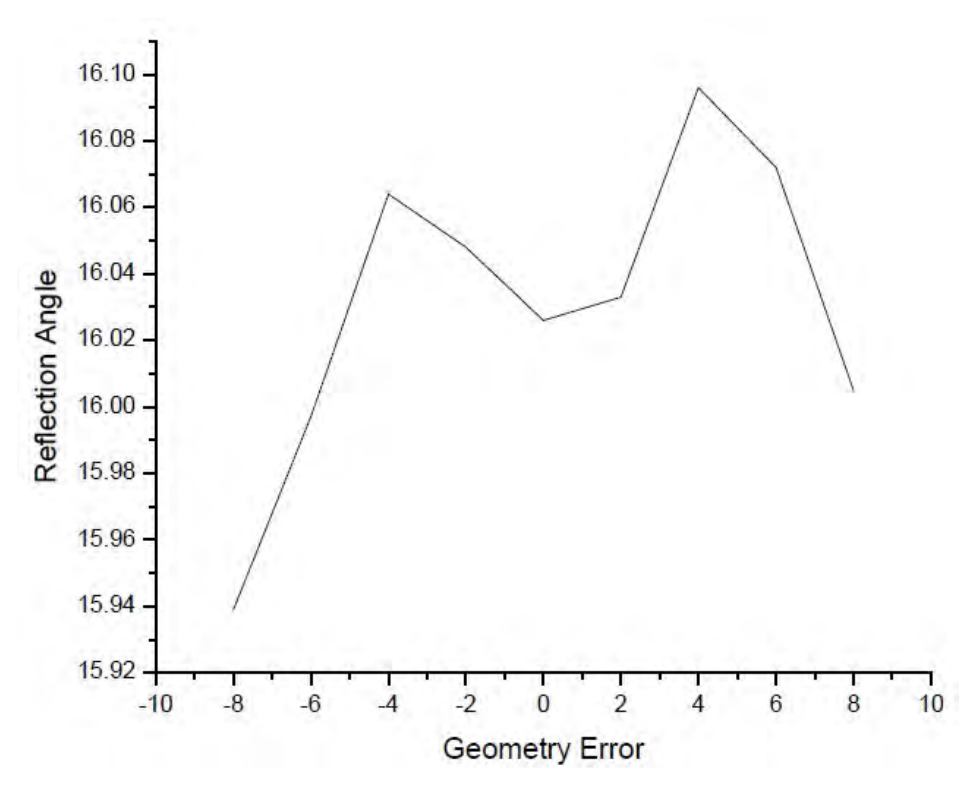
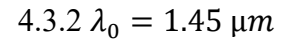


Figure 38 - Analysis of the reflection angle θ_r as geometry errors are inserted in the supercell for the wavelength of 1.4 μm .

To complement the results shown for the wave propagation of Figure 37, it is shown in Figure 38 how the reflection angle, θ_r , varies from the designed angle of 17.17° for the wavelength of 1.4 μ m, along with the geometry errors. The wavelength of 1.4 μ m has a reasonable influence in deviating θ_r in approximately -0.97°. The geometry errors among -8 μ m and +8 μ m increasing meaninglessly the error in, respectively, -1.23° and -1.0°, approximately, related to the zero error condition (16.01°).



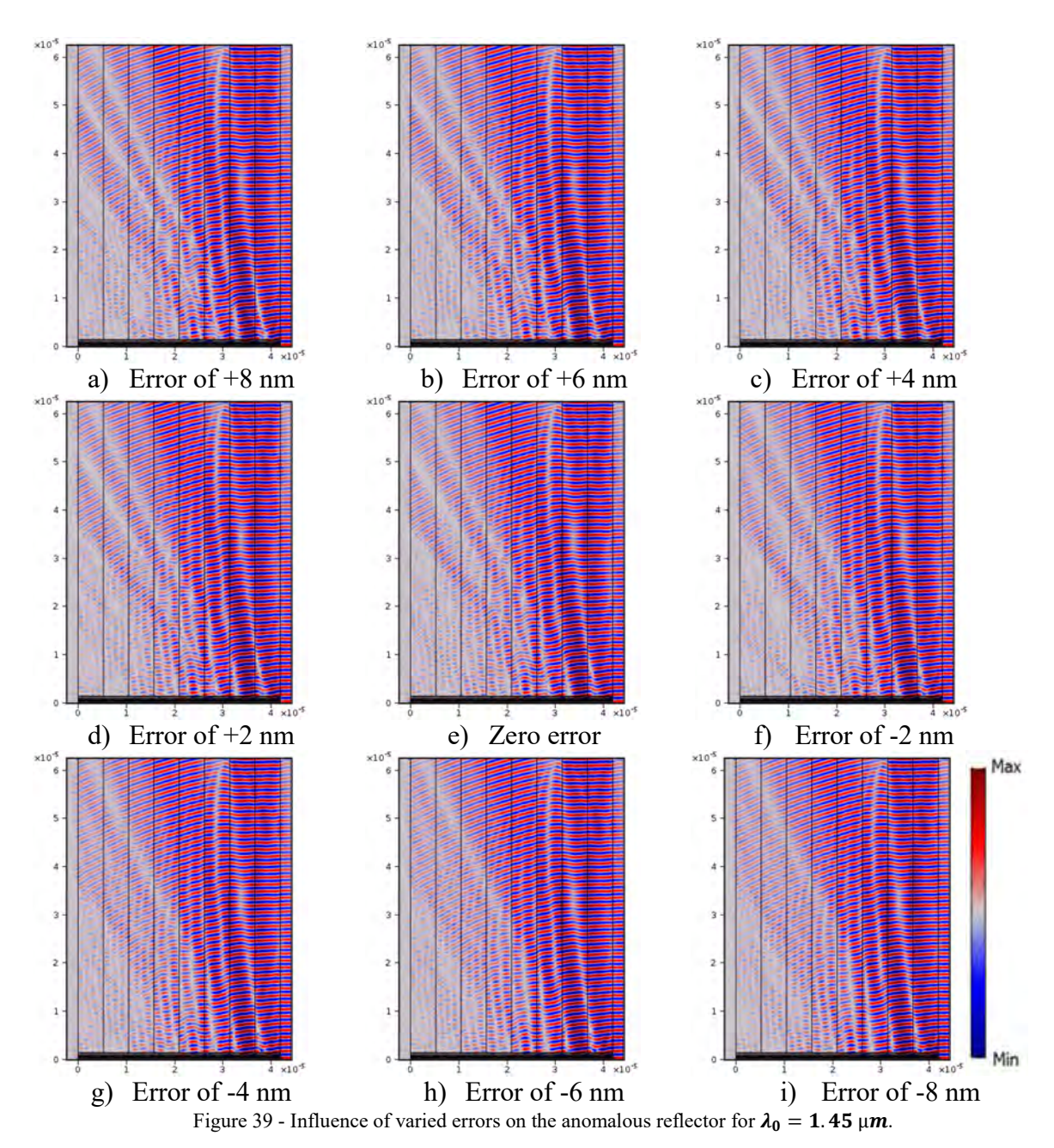


Figure 39 shows, in a qualitative form, the reflection occurring for the wavelength of 1.45 μ m, considering the geometry error range in the pair (w_a , w_b) from -8 to 8 nm in steps of 2 nm.

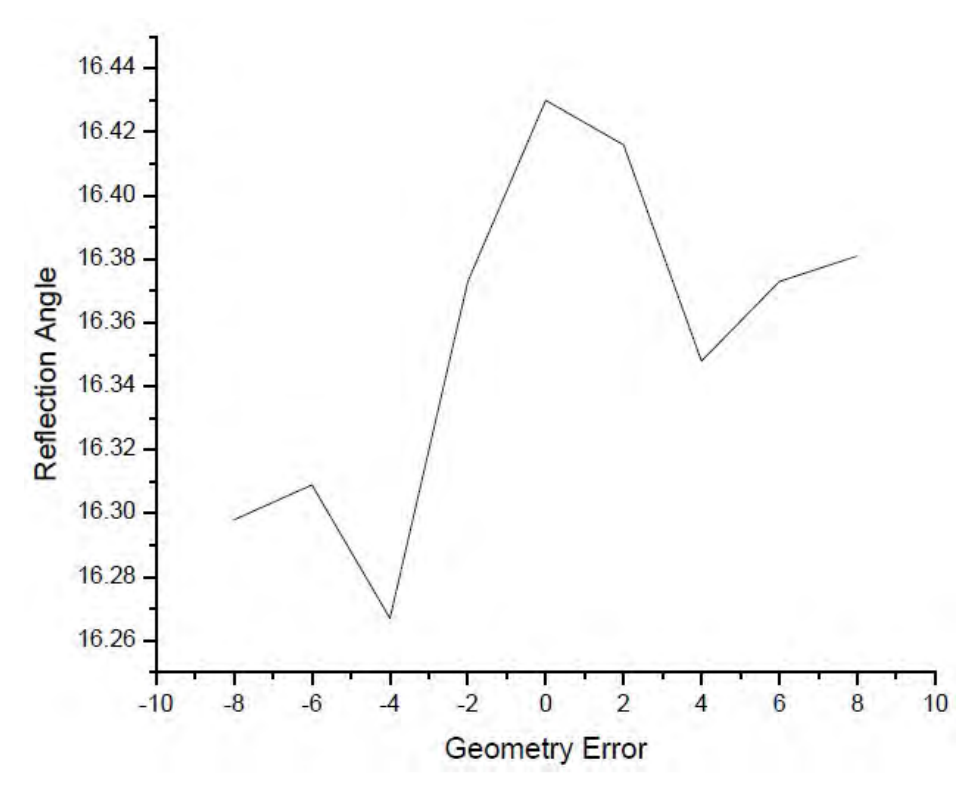
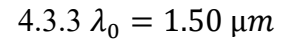


Figure 40 - Analysis of the reflection angle θ_r as geometry errors are inserted in the supercell for the wavelength of 1.45 μm .

To complement the results shown for the wave propagation of Figure 39 it is shown in Figure 40 how the reflection angle, θ_r , varies from the designed angle of 17.17° for the wavelength of 1.45 μ m, along with the geometry errors. The wavelength of 1.45 μ m has a reasonable influence in deviating θ_r in approximately -0.74°. The geometry errors among -8 μ m and +8 μ m increasing meaninglessly the error in, respectively, -0.13° and -0.05°, approximately, related to the zero error condition (16.43°).



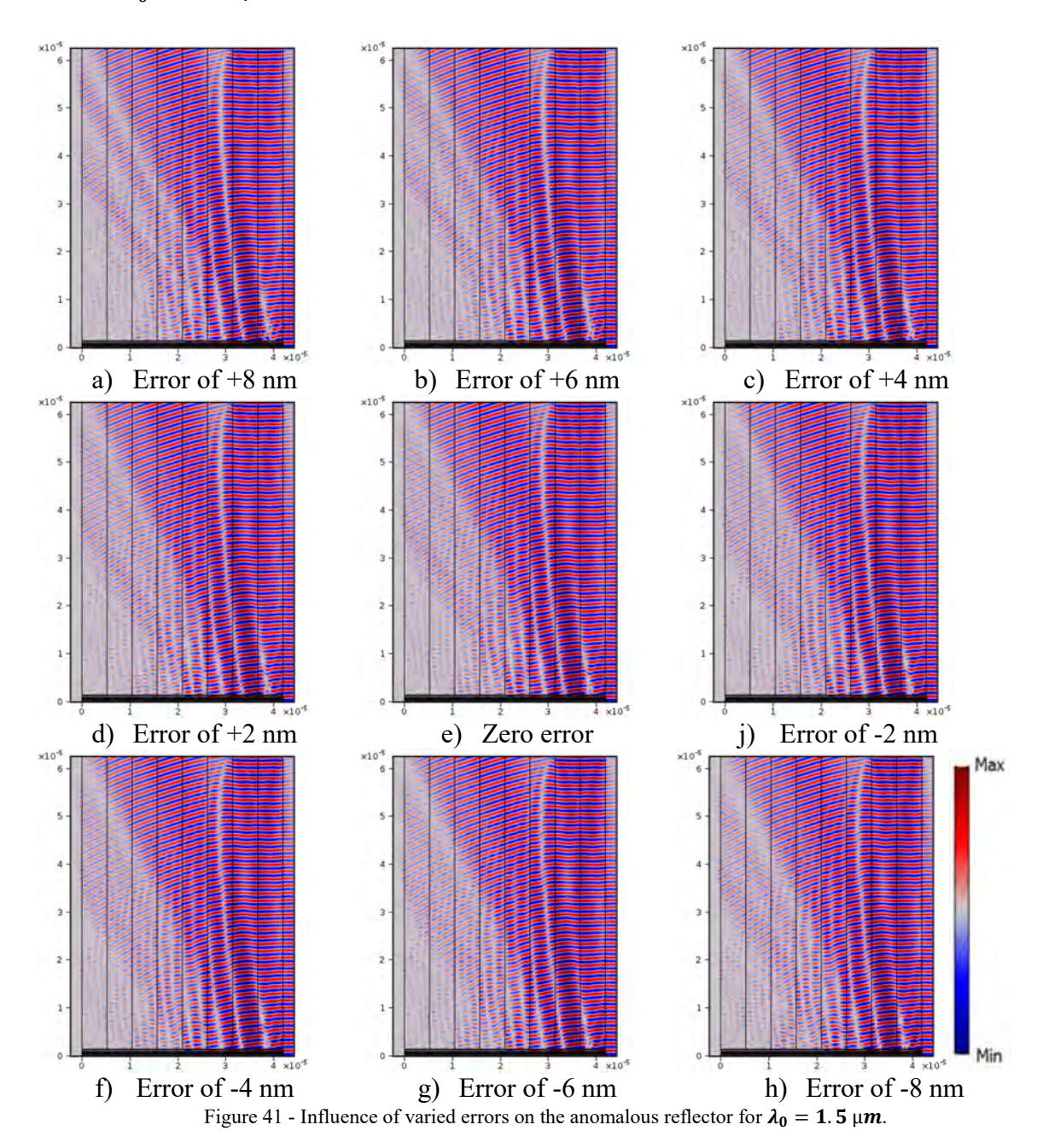


Figure 41 shows, in a qualitative form, the reflection occurring for the wavelength of 1.5 μ m, considering the geometry error range in the pair (w_a, w_b) from - 8 to 8 nm in steps of 2 nm.

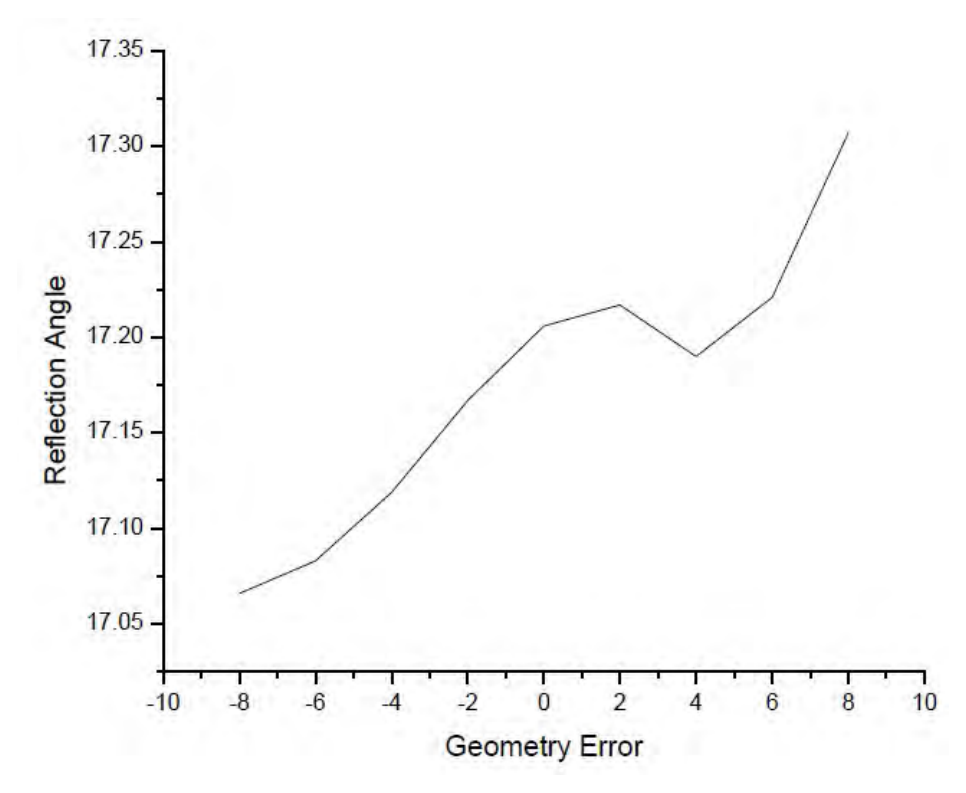
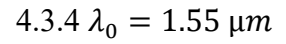


Figure 42 - Analysis of the reflection angle θ_r as geometry errors are inserted in the supercell for the wavelength of 1.5 μ m.

To complement the results shown for the wave propagation of Figure 41 it is shown in Figure 42 how the reflection angle, θ_r , varies from the designed angle of 17.17° for the wavelength of 1.5 µm, along with the geometry errors. The wavelength of 1.5 µm has an insignificant influence in deviating θ_r in approximately +0.03°. The geometry errors among -8 µm and +8 µm increasing meaninglessly the error in, respectively, -0.11° and +0.13°, approximately, related to the zero error condition (17.20°).



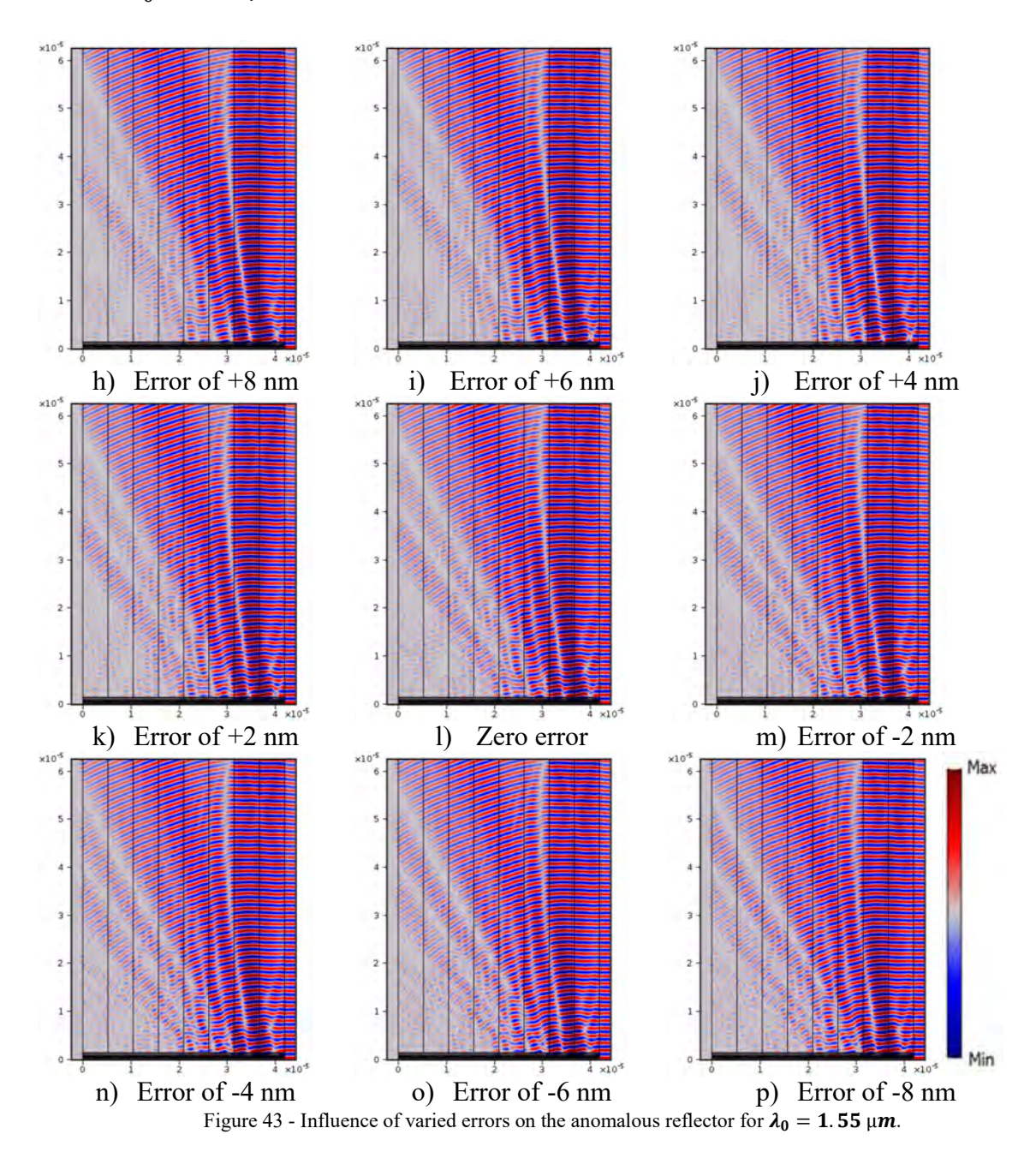


Figure 43 shows, in a qualitative form, the reflection occurring for the wavelength of 1.55 μ m, considering the geometry error range in the pair (w_a, w_b) from -8 to 8 nm in steps of 2 nm.

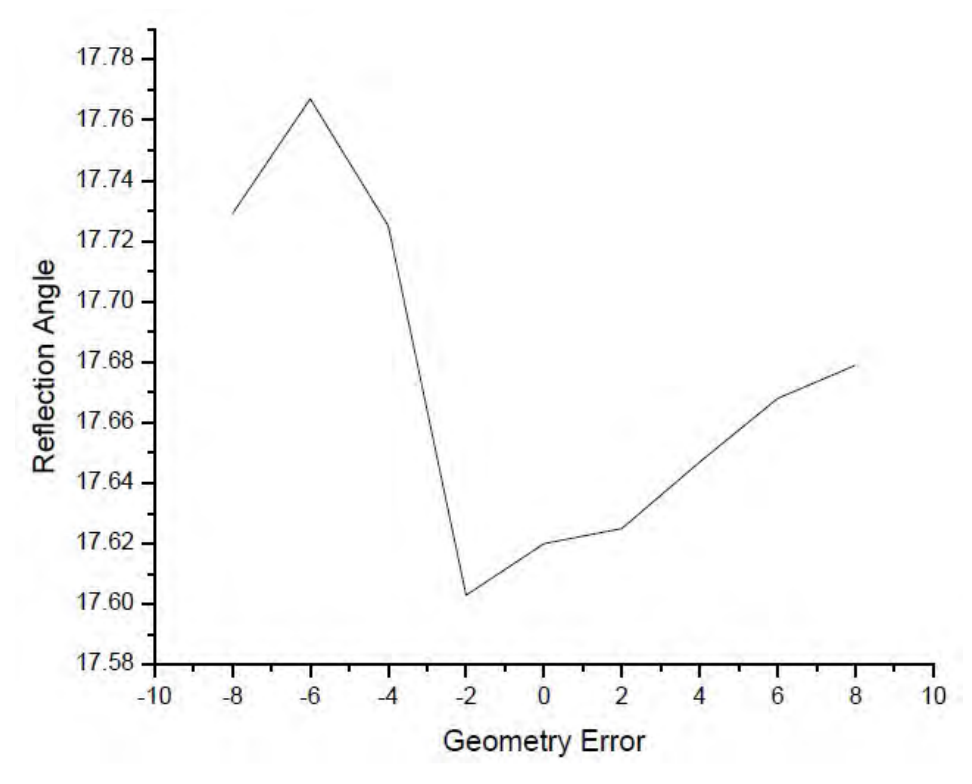
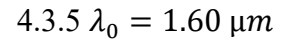


Figure 44 - Analysis of the reflection angle θ_r as geometry errors are inserted in the supercell for the wavelength of 1.55 μm .

To complement the results shown for the wave propagation of Figure 43 it is shown in Figure 44 how the reflection angle, θ_r , varies from the designed angle of 17.17° for the wavelength of 1.55 μ m, along with the geometry errors. The wavelength of 1.55 μ m has a very small influence in deviating θ_r in approximately +0.46°. The geometry errors among -8 μ m and +8 μ m increasing meaninglessly the error in, respectively, +0.1° and +0.05°, approximately, related to the zero error condition (17.63°).



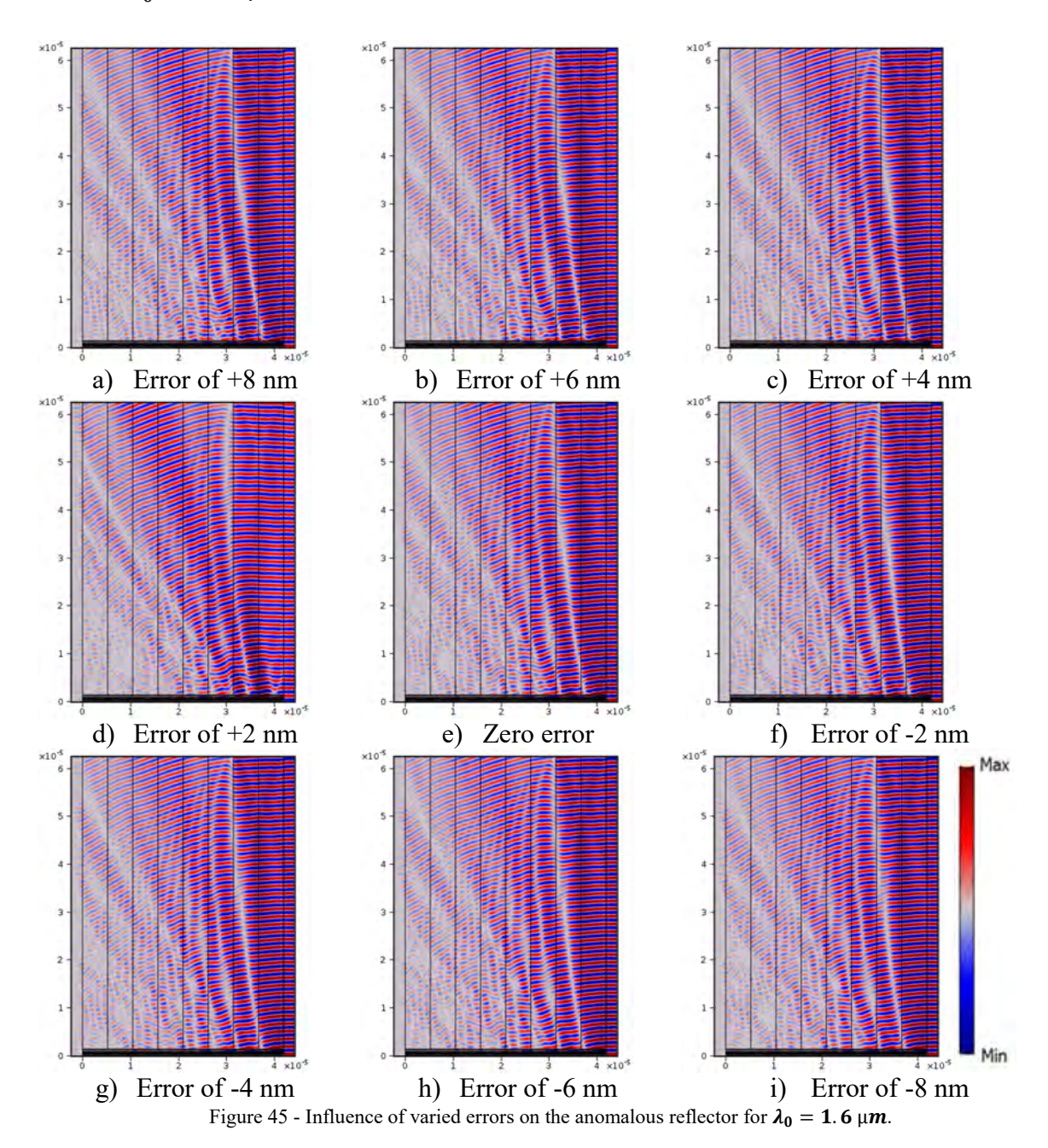


Figure 45 shows, in a qualitative form, the reflection occurring for the wavelength of 1.6 μ m, considering the geometry error range in the pair (w_a, w_b) from - 8 to 8 nm in steps of 2 nm.

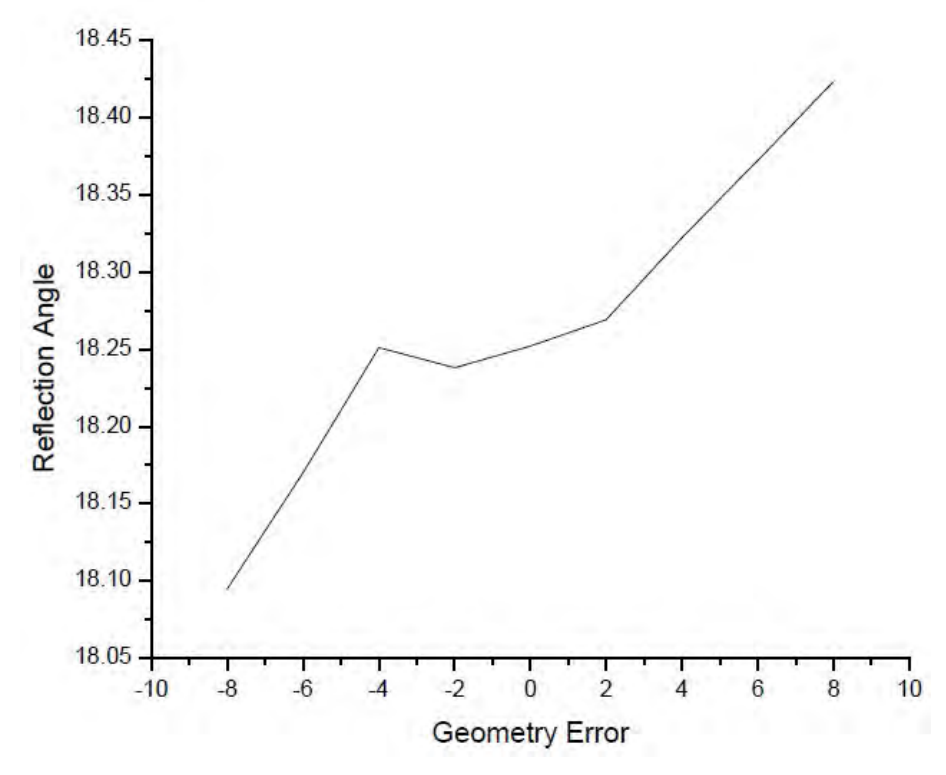
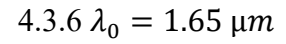


Figure 46 - Analysis of the reflection angle θ_r as geometry errors are inserted in the supercell for the wavelength of 1.6 μm .

To complement the results shown for the wave propagation of Figure 45 it is shown in Figure 46 how the reflection angle, θ_r , varies from the designed angle of 17.17° for the wavelength of 1.6 μ m, along with the geometry errors. The wavelength of 1.6 μ m has a reasonable influence in deviating θ_r in approximately +1.08°. The geometry errors among -8 μ m and +8 μ m increasing meaninglessly the error in -0.15° and +0.18°, approximately, related to the zero error condition (18.25°).



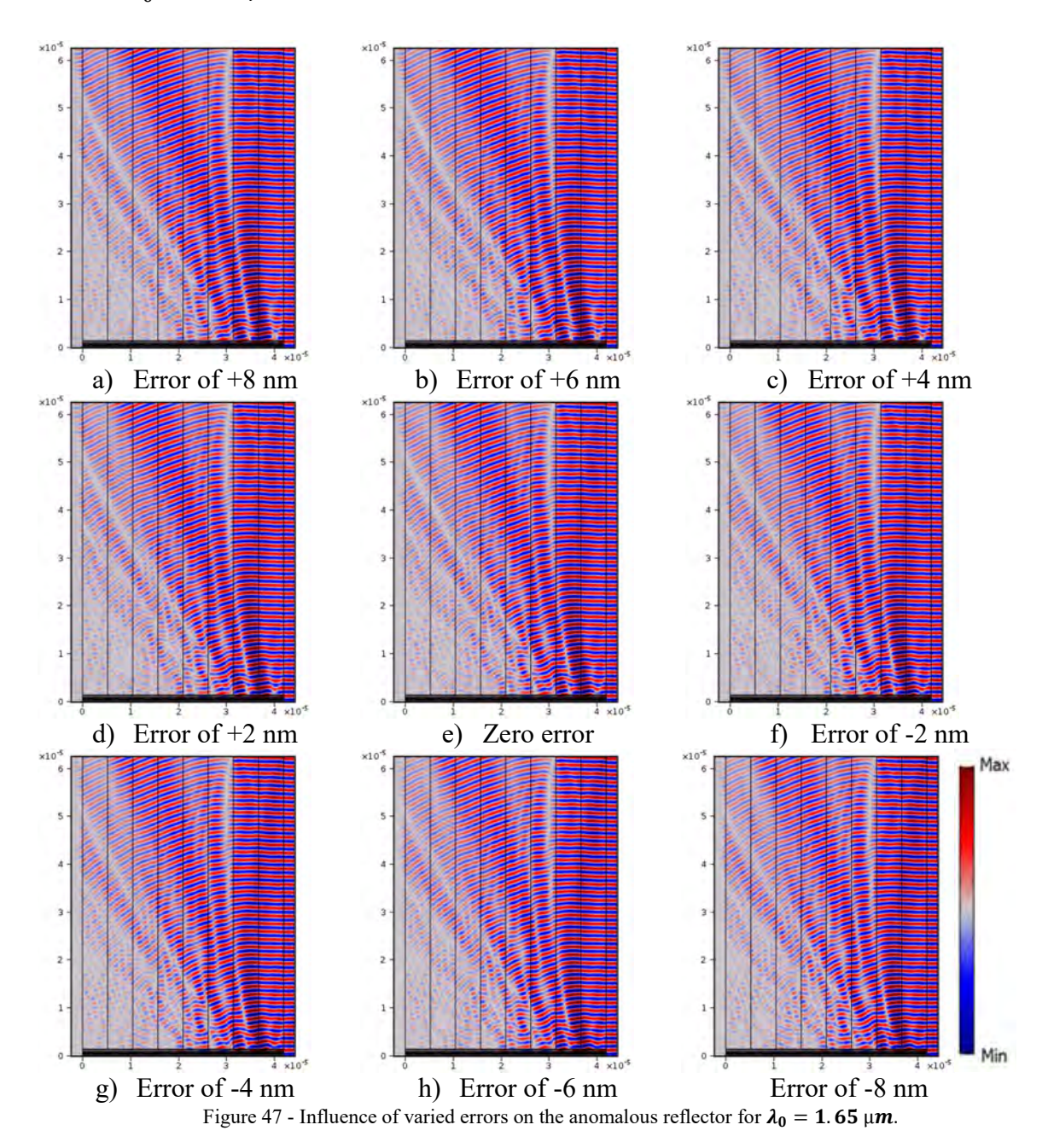


Figure 47 shows, in a qualitative form, the reflection occurring for the wavelength of 1.65 μ m, considering the geometry error range in the pair (w_a, w_b) from -8 to 8 nm in steps of 2 nm.

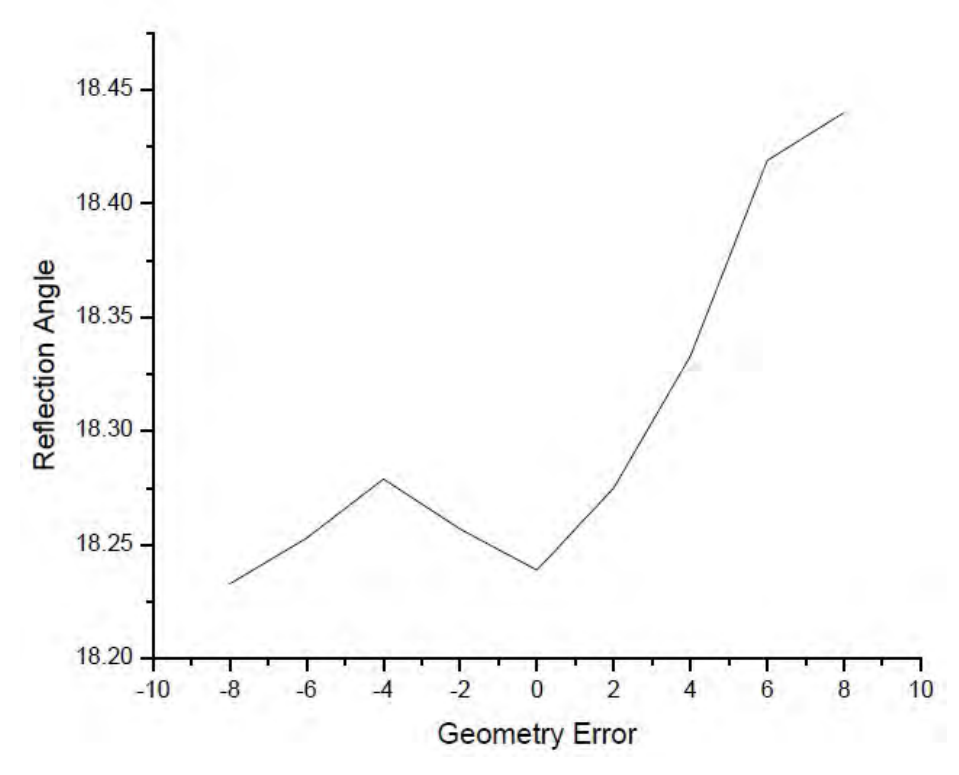
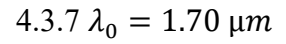


Figure 48 - Analysis of the reflection angle θ_r as geometry errors are inserted in the supercell for the wavelength of 1.65 μm .

To complement the results shown for the wave propagation of Figure 47 it is shown in Figure 48 how the reflection angle, θ_r , varies from the designed angle of 17.17° for the wavelength of 1.65 μ m, along with the geometry errors. The wavelength of 1.65 μ m has a small influence in deviating θ_r in approximately +1.07°. The geometry errors among -8 μ m and +8 μ m increasing meaninglessly the error in 0° and +0.20°, approximately, related to the zero error condition (18.24°).



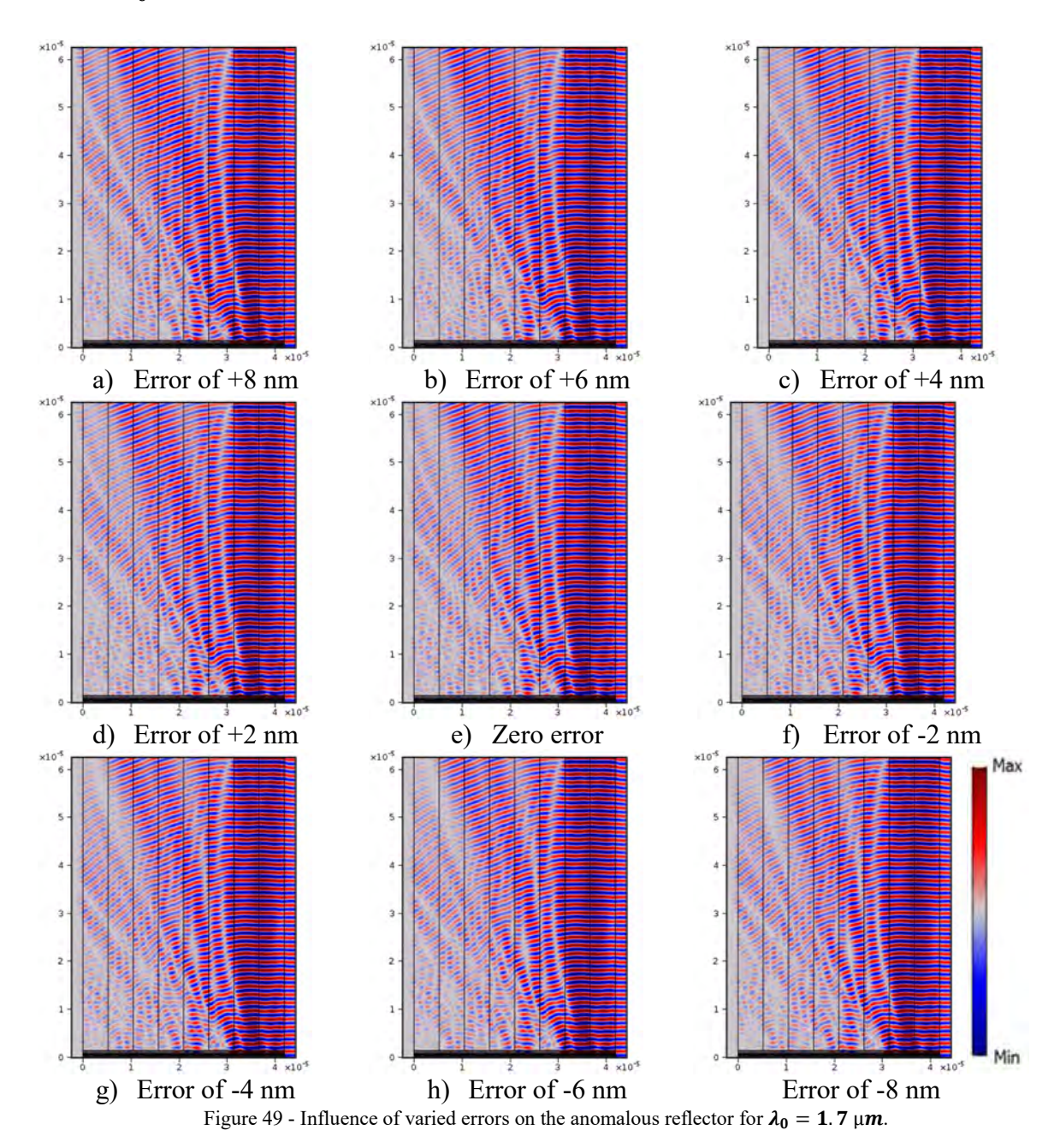


Figure 49 shows, in a qualitative form, the reflection occurring for the wavelength of 1.7 μ m, considering the geometry error range in the pair (w_a, w_b) from - 8 to 8 nm in steps of 2 nm.

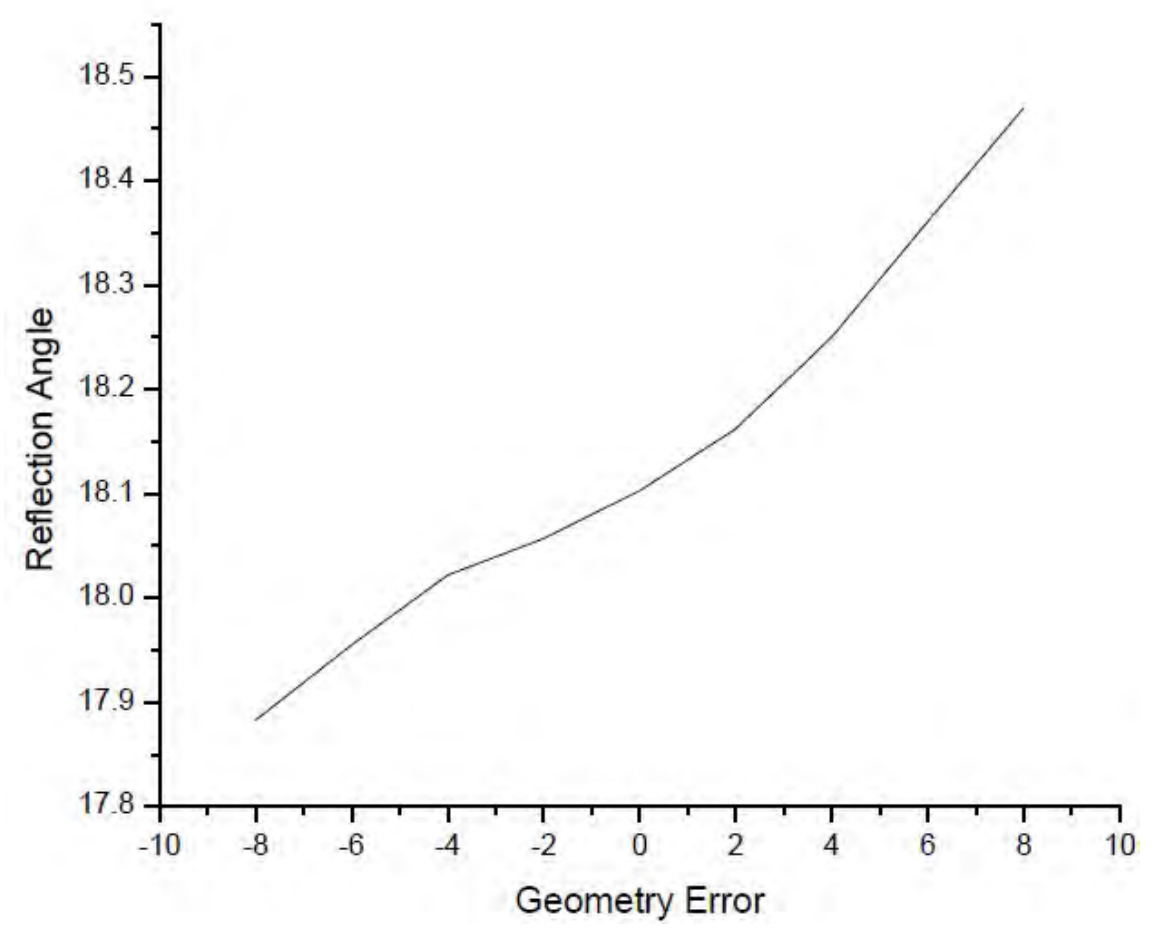


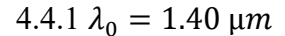
Figura 50 - Analysis of the reflection angle θ_r as geometry errors are inserted in the supercell for the wavelength of 1.7 μ m.

To complement the results shown for the wave propagation of Figure 49 it is shown in Figure 50 how the reflection angle, θ_r , varies from the designed angle of 17.17° for the wavelength of 1.7 μ m, along with the geometry errors. The wavelength of 1.7 μ m has a reasonable influence in deviating θ_r in approximately +0.93°. The geometry errors among -8 μ m and +8 μ m increasing meaninglessly the error in -0.20° and +0.35°, approximately, related to the zero error condition (18.1°).

4.4 EFFECTS OF GEOMETRY ERRORS IN THE METALENS

To find out how much the geometry errors influences the performance of the metalens, for each considered wavelength, one can compare its focal distance and its power density, as well as the square of the electric field, in the focal plane to the expected values of an ideal structure.

The x position of the focal plane of the proposed symmetric metalens is right in its horizontal center. It is, then, of greater importance, to obtain the vertical position y. In order to precisely obtain the position y of the focal plane, the procedure was to extract the point of maximum value of the Poynting vector and its coordinate, which is the searched focal plane y position. This coordinate also delivers the power density module on the focus y coordinate. These two information will be shown on the legends of the next Figures, about the power density of the wave, S (the Poynting vector), through the all-dielectric metalens. Same information will be brought as tables for easiness of consultation.



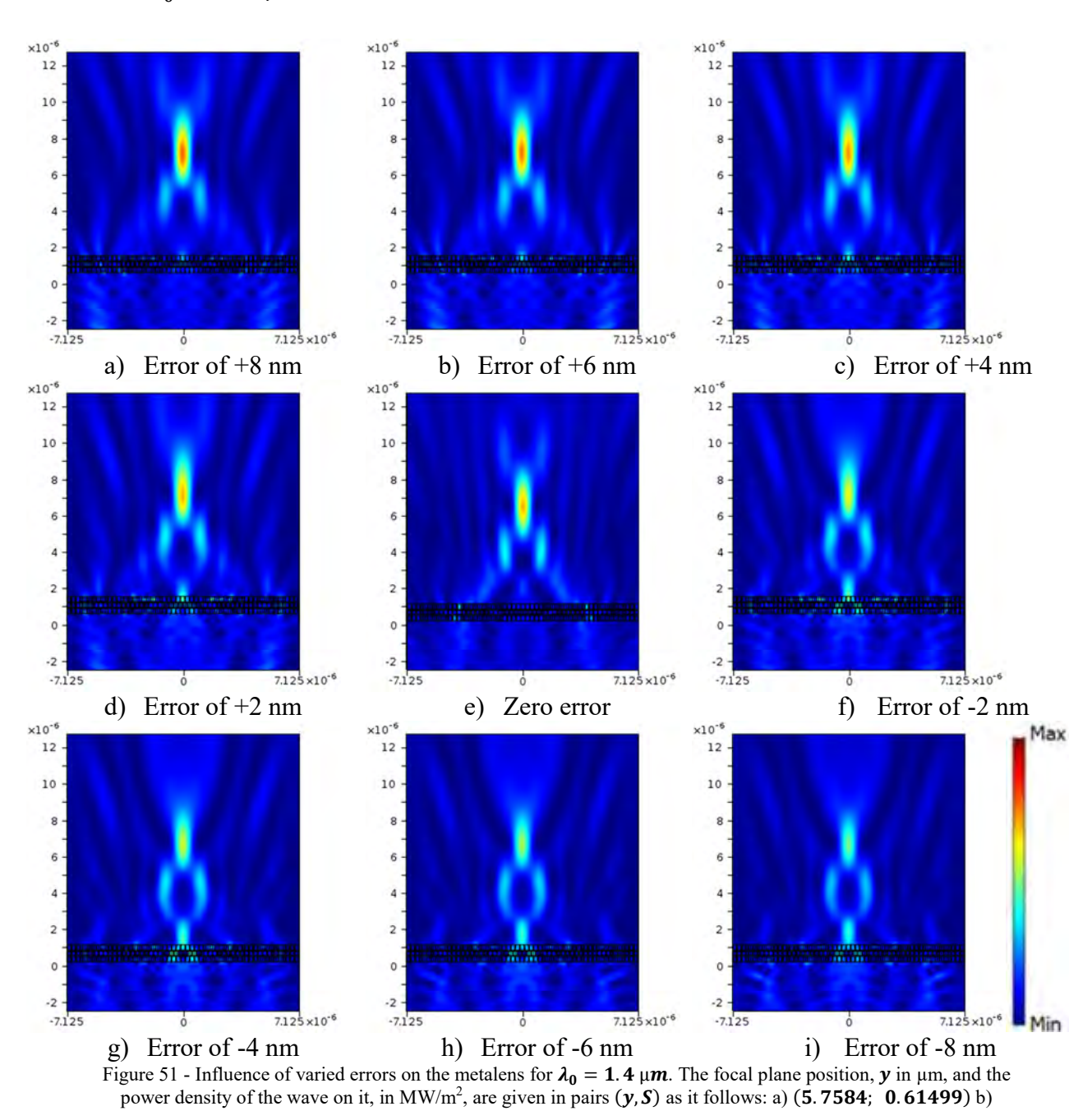


Figure 51 shows, in a qualitative form, the power density of the wave reaching its highest intensity in the region of the focal plane. It is considered for wavelength of 1.4 μ m, and the geometry error range in the pair (w_a, w_b) from -8 to 8 nm in steps of 2 nm.

(5.6029; 0.59454) c) (5.6902; 0.58701) d) (5.6662; 0.5542) e) (5.5132; 0.51946) f) (5.4767; 0.48341) g) (5.5450; 0.46426) h) (5.5544; 0.42149) i) (5.4293; 0.38656)

Table 4.1 relates the power density of the EMW to the position of the focal plane of the metalens:

Geometry error, in (nm)	Focal plane position (y, in μm)	Power density of the wave (S, in MW/m²)
	 	(5, III 141 44/III)
+8	5.7584	0.61499
+6	5.5029	0.59454
+4	5.6902	0.58701
+2	5.6662	0.5542
0	5.5132	0.51946
-2	5.4767	0.48341
-4	5.5450	0.46426
-6	5.5544	0.42149
-8	5.4293	0.38656

Table 4.1 – Focal plane position and power density of the wave related to each geometry error of the metalens, considering $\lambda_0 = 1.4 \ \mu m$.

For $\lambda_0 = 1.4 \,\mu m$, the effects of the geometry errors which are propagated along the structure of the metalens and the power density of the incident wave on the focal plane are shown in Figure 51 and Table 4.1. Figure 51 makes possible to visualize the shifts of the focal plane, while Table 4.1 relates both the focal plane y position and the power density of the wave (on the focal plane) to the applied geometry error over the structure.

Related to the ideal supercell structure (zero error), the error of +8 nm introduces the highest deviation of focal plane position, which shifts up from 5.5132 to 5.7584 μm , while the lowest focal plane position, 5.4293 μm , is set by the error of -8 nm.

The power density of the wave has the highest increase, from 0.51946 to 0.61499 MW/m^2 when the error varies from 0 to +8 nm. Its highest decrease occurs when the geometry error is -8 nm, which lowers the power density from 0.51946 to 0.38656 MW/m^2 .

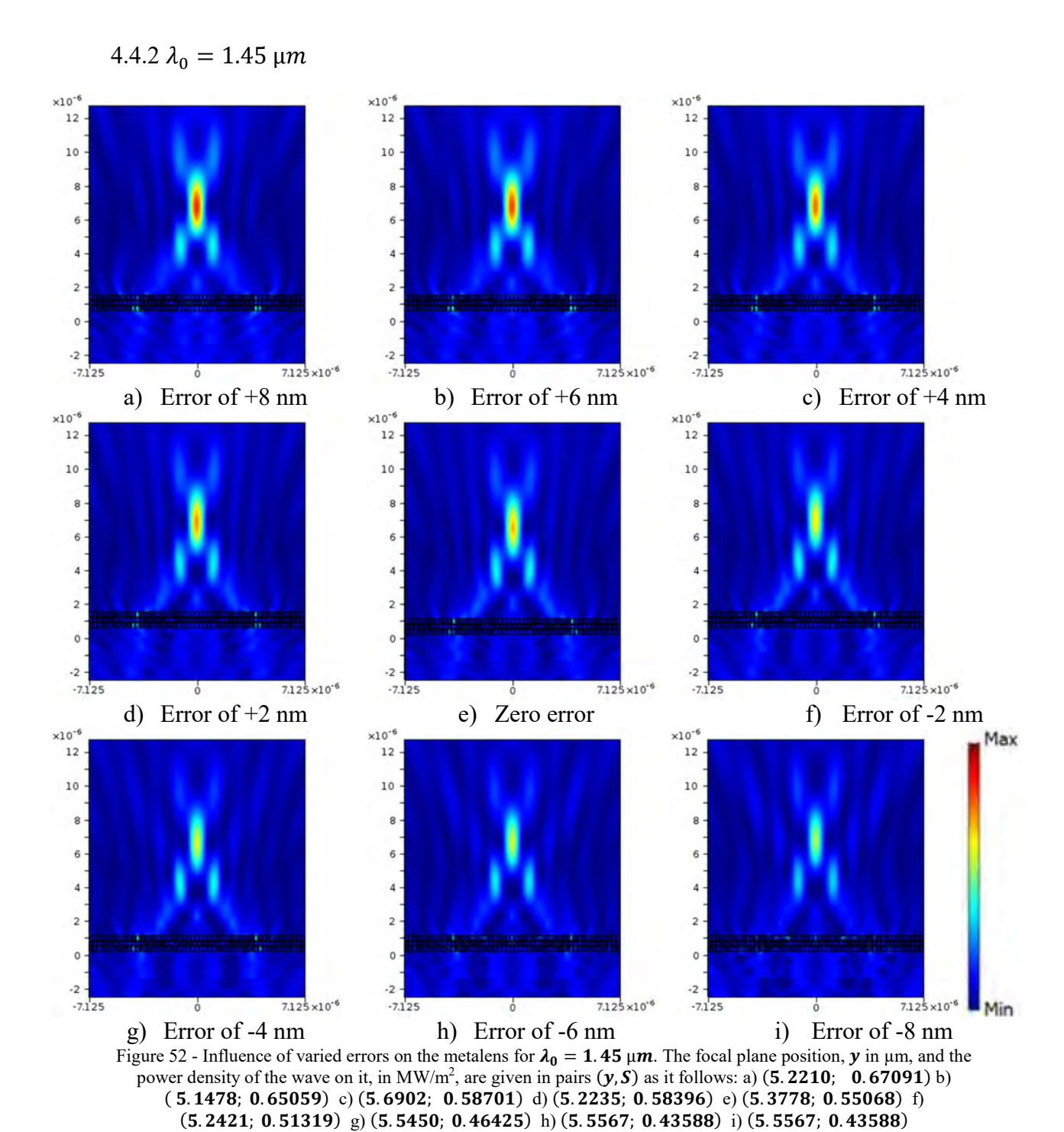


Figure 52 shows, in a qualitative form, the power density of the wave reaching its highest intensity in the region of the focal plane. It is considered for wavelength of 1.45 μ m, and the geometry error range in the pair (w_a, w_b) from -8 to 8 nm in steps of 2 nm.

Table 4.2 relates the power density of the EMW to the position of the focal plane of the metalens:

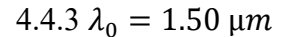
Geometry error,	Focal plane position (y, in	Power density of the wave (S, in MW/m²)
in (nm)	μm)	(3, III WI W/III)
+8	5.2210	0.67091
+6	5.1478	065059
+4	5.6902	0.58701
+2	5.2235	0.58396
0	5.3778	0.55068
-2	5.2421	0.51319
-4	5.5450	0.46425
-6	5.5567	0.43588
-8	5.5567	0.43588

Table 4.2 – Focal plane position and power density of the wave related to each geometry error of the metalens, considering $\lambda_0 = 1.45 \ \mu m$.

For $\lambda_0 = 1.45 \,\mu m$, the effects of the geometry errors which are propagated along the structure of the metalens and the power density of the incident wave on the focal plane are shown in Figure 52 and Table 4.2. Figure 52 makes possible to visualize the shifts of the focal plane, while Table 4.2 relates both the focal plane y position and the power density of the wave (on the focal plane) to the applied geometry error over the structure.

Related to the ideal supercell structure (zero error), the error of +4 nm introduces the highest deviation of focal plane position, which shifts up from 5.3778 to 5.6902 μm , while the lowest focal plane position, 5.1478 μm , is set by the error of +6 nm.

The power density of the wave has the highest increase, from 0.55068 to 0.67091 MW/m^2 when the error varies from 0 to +8 nm. Its highest decrease occurs when the geometry error is -8 nm, which lowers the power density from 0.55068 to 0.43588 MW/m^2 .



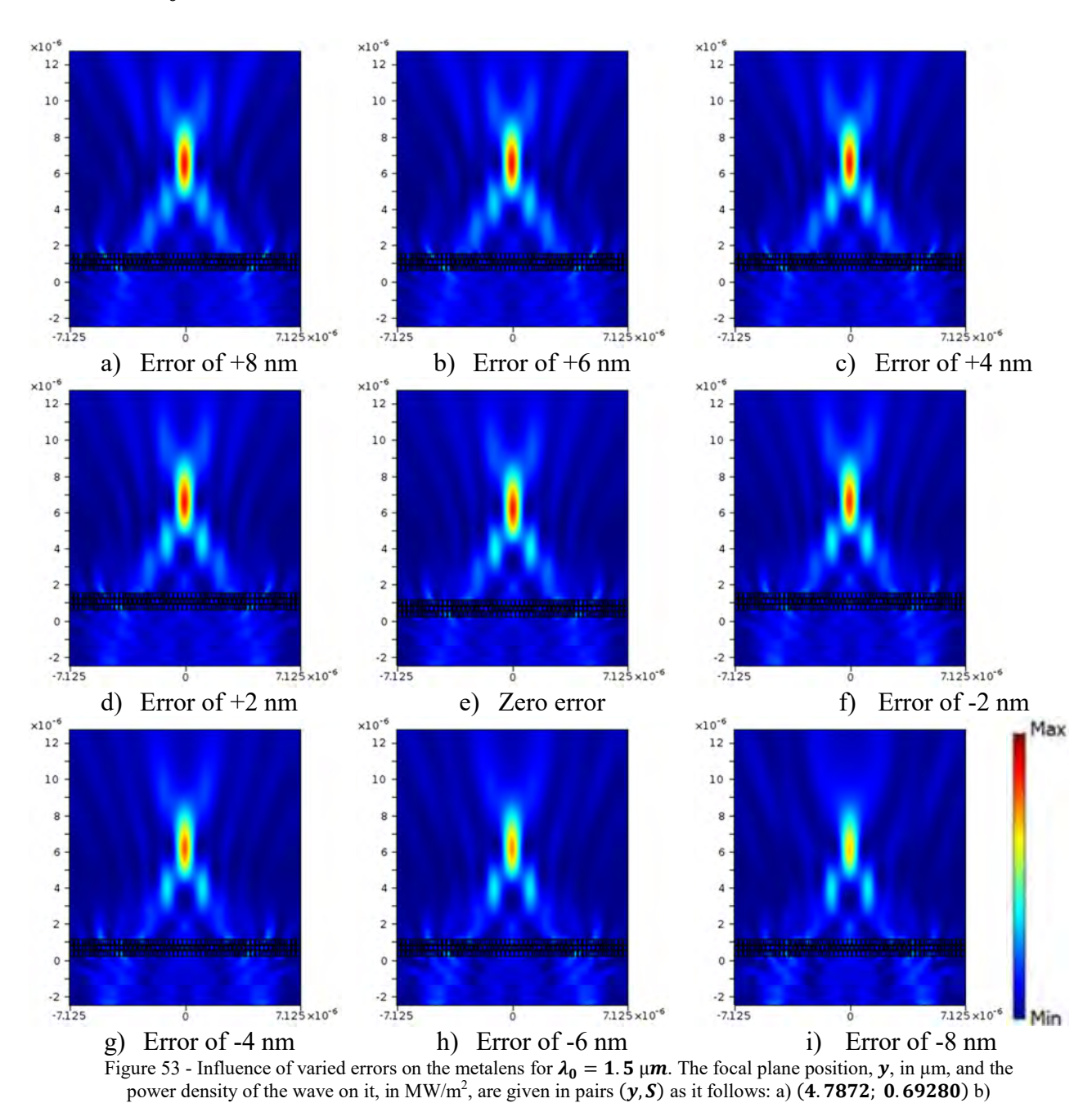


Figure 53 shows, in a qualitative form, the power density of the wave reaching its highest intensity in the region of the focal plane. It is considered for wavelength of 1.5 μ m, and the geometry error range in the pair (w_a, w_b) from -8 to 8 nm in steps of 2 nm.

(4.4892; 0.66862) c) (5.0734; 0.69189) d) (4.9592; 0.68257) e) (5.1144; 0.67768) f) (4.9180; 0.66198) g) (5.0850; 0.62426) h) (5.1741; 0.58496) i) (5.0028; 0.53436)

Table 4.3 relates the power density of the EMW to the position of the focal plane of the metalens:

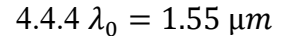
Geometry error,	Focal plane position (y, in μm)	Power density of the wave
in (nm)		$(S, \text{ in } MW/m^2)$
+8	4.7872	0.69280
+6	4.4892	0.66862
+4	5.0734	0.69189
+2	4.9592	0.68257
0	5.1144	0.67768
-2	4.9180	0.66198
-4	5.0850	0.62426
-6	5.1741	0.58496
-8	5.0028	0.53436

Table 4.3 – Focal plane position and power density of the wave related to each geometry error of the metalens, considering $\lambda_0 = 1.5 \ \mu m$.

For $\lambda_0 = 1.5 \,\mu m$, the effects of the geometry errors which are propagated along the structure of the metalens and the power density of the incident wave on the focal plane are shown in Figure 53 and Table 4.3. Figure 53 makes possible to visualize the shifts of the focal plane, while Table 4.3 relates both the focal plane y position and the power density of the wave (on the focal plane) to the applied geometry error over the structure.

Related to the ideal supercell structure (zero error), the error of -6 nm introduces the highest deviation of focal plane position, which shifts up from 5.1144 to 5.1741 μm , while the lowest focal plane position, 4.4892 μm , is set by the error of +6 nm.

The power density of the wave has the highest increase, from 0.67768 to 0.69280 MW/m^2 when the error varies from 0 to +8 nm. Its highest decrease occurs when the geometry error is -8 nm, which lowers the power density from 0.67768 to 0.53436 MW/m^2 .



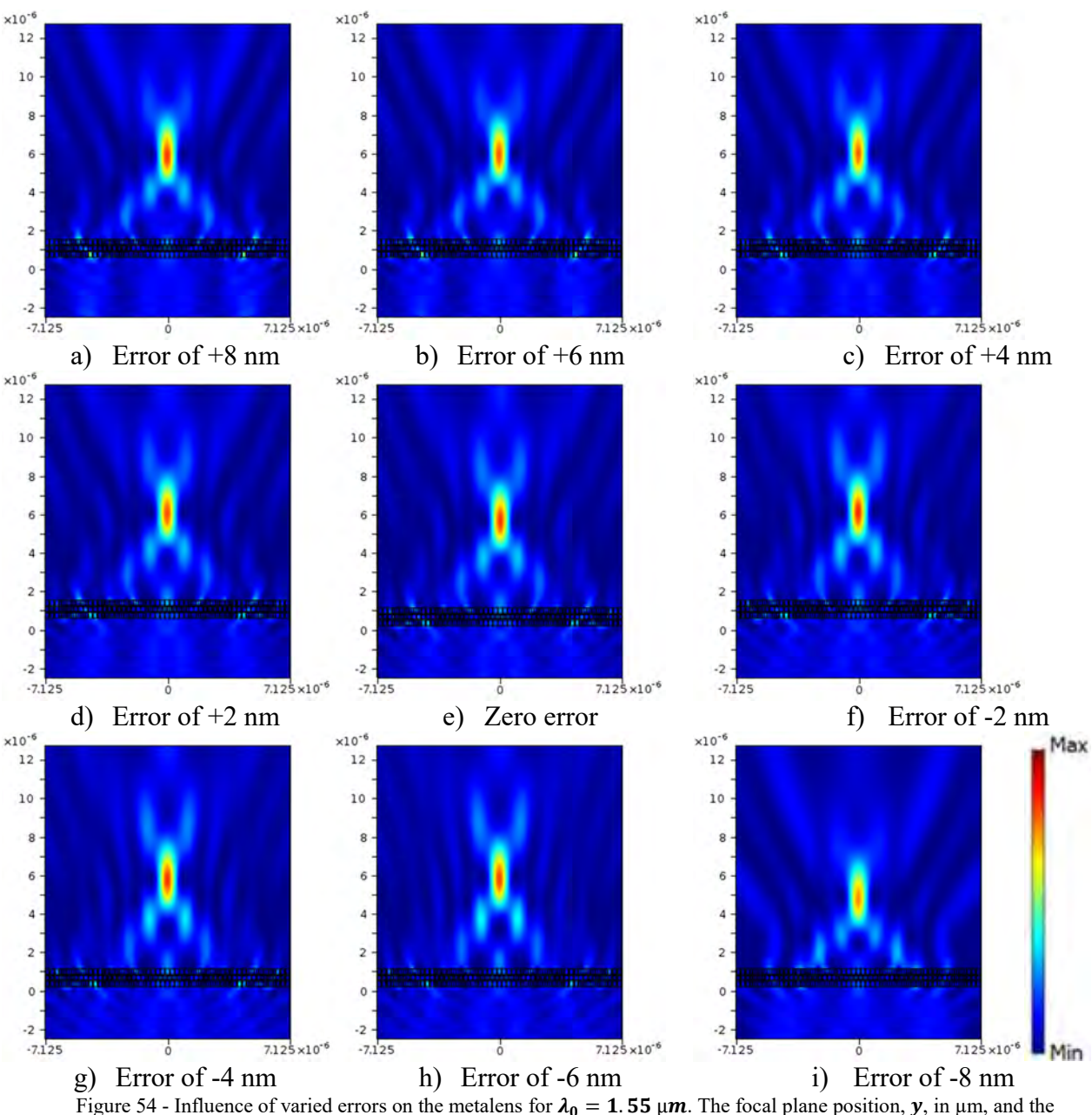


Figure 54 - Influence of varied errors on the metalens for $\lambda_0 = 1.55 \,\mu\text{m}$. The focal plane position, y, in μ m, and the power density of the wave on it, in MW/m², are given in pairs (y, S) as it follows: a) $(4.4481; \ 0.65490)$ b) $(4.4892; \ 0.62586)$ c) $(4.4456; \ 0.63027)$ d) $(4.5300; \ 0.64069)$ e) $(4.3404; \ 0.65677)$ f) $(4.6256; \ 0.67154)$ g) $(4.6594; \ 0.65990)$ h) $(4.7515; \ 0.64987)$ i) $(4.5630; \ 0.63008)$

Figure 54 shows, in a qualitative form, the power density of the wave reaching its highest intensity in the region of the focal plane. It is considered for wavelength of 1.55 μ m, and the geometry error range in the pair (w_a, w_b) from -8 to 8 nm in steps of 2 nm.

Table 4.4 relates the power density of the EMW to the position of the focal plane of the metalens:

Geometry error, in (nm)	Focal plane position (y, in μm)	Power density of the wave (S, in MW/m ²)
+8	4.4481	0.65490
+6	4.4892	0.62586
+4	4.4456	0.63027
+2	4.5300	0.64069
0	4.3404	0.65677
-2	4.6256	0.67154
-4	4.6594	0.65990
-6	4.7515	0.64897
-8	4.5630	0.63008

Table 4.4 – Focal plane position and power density of the wave related to each geometry error of the metalens, considering $\lambda_0 = 1.55 \, \mu m$.

For $\lambda_0 = 1.55 \,\mu m$, the effects of the geometry errors which are propagated along the structure of the metalens and the power density of the incident wave on the focal plane are shown in Figure 54 and Table 4.4. Figure 54 makes possible to visualize the shifts of the focal plane, while Table 4.4 relates both the focal plane y position and the power density of the wave (on the focal plane) to the applied geometry error over the structure.

Related to the ideal supercell structure (zero error), the error of -6 nm introduces the highest deviation of focal plane position, which shifts up from 4.3404 to 4.7515 μ m, while the lowest focal plane position, 4.3404 μ m, is set by the ideal (zero error) supercell geometry.

The power density of the wave has the highest increase, from 0.65677 to $0.67154~\text{MW/m}^2$ when the error varies from 0 to -2 nm. Its highest decrease occurs when the geometry error is -8 nm, which lowers the power density from 0.67768 to $0.62586~\text{MW/m}^2$.



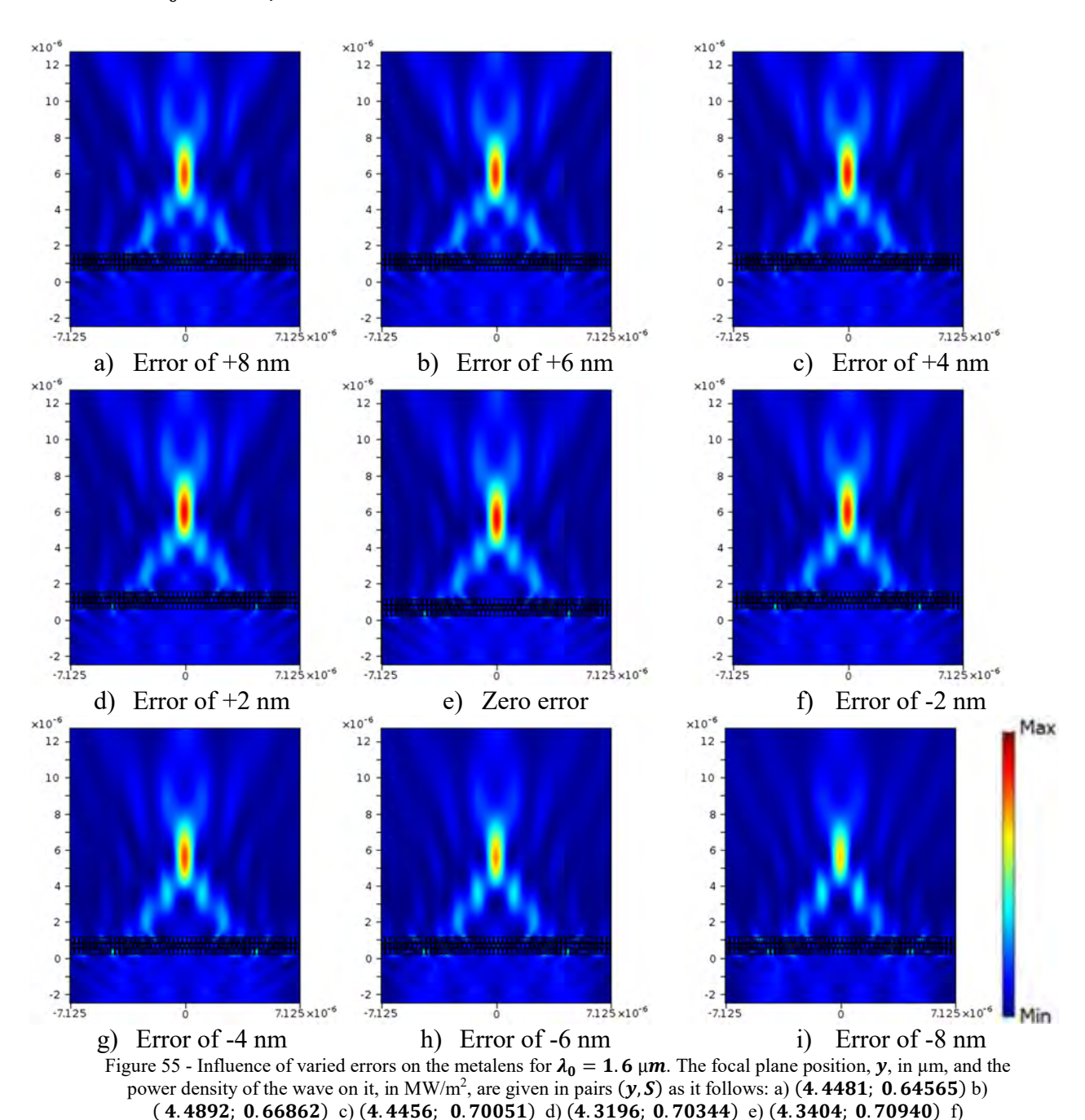


Figure 55 shows, in a qualitative form, the power density of the wave reaching its highest intensity in the region of the focal plane. It is considered for wavelength of 1.6 μ m, and the geometry error range in the pair (w_a, w_b) from -8 to 8 nm in steps of 2 nm.

(4.5019; 0.68495) g) (4.3267; 0.65145) h) (4.4219; 0.58850) i) (4.5630; 0.53420)

Table 4.5 relates the power density of the EMW to the position of the focal plane of the metalens:

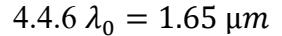
Geometry error, in	Focal plane position	Power density of the wave (S, in
(nm)	(y, in μm)	MW/m^2)
+8	4.4481	0.64565
+6	4.4892	0.66862
+4	4.4456	0.70051
+2	4.3196	0.70344
0	4.3404	0.70940
-2	4.5019	0.68495
-4	4.3267	0.65145
-6	4.4219	0.58850
-8	4.5630	0.53420

Table 4.5 – Focal plane position and power density of the wave related to each geometry error of the metalens, considering $\lambda_0 = 1.6 \ \mu m$.

For $\lambda_0 = 1.6 \,\mu m$, the effects of the geometry errors which are propagated along the structure of the metalens and the power density of the incident wave on the focal plane are shown in Figure 55 and Table 4.5. Figure 55 makes possible to visualize the shifts of the focal plane, while Table 4.5 relates both the focal plane y position and the power density of the wave (on the focal plane) to the applied geometry error over the structure.

Related to the ideal supercell structure (zero error), the error of -8 nm introduces the highest deviation of focal plane position, which shifts up from 4.3404 to $4.5630\mu m$, while the lowest focal plane position, $4.3196 \mu m$, is set by the error of +2 nm.

The highest power density of the wave is 0.70940 MW/m^2 and occurs for the ideal supercell (for zero geometry error). The highest decrease of the power density occurs when the geometry error is -8 nm, which lowers the power density from $0.70940 \text{ to } 0.53420 \text{ MW/m}^2$.



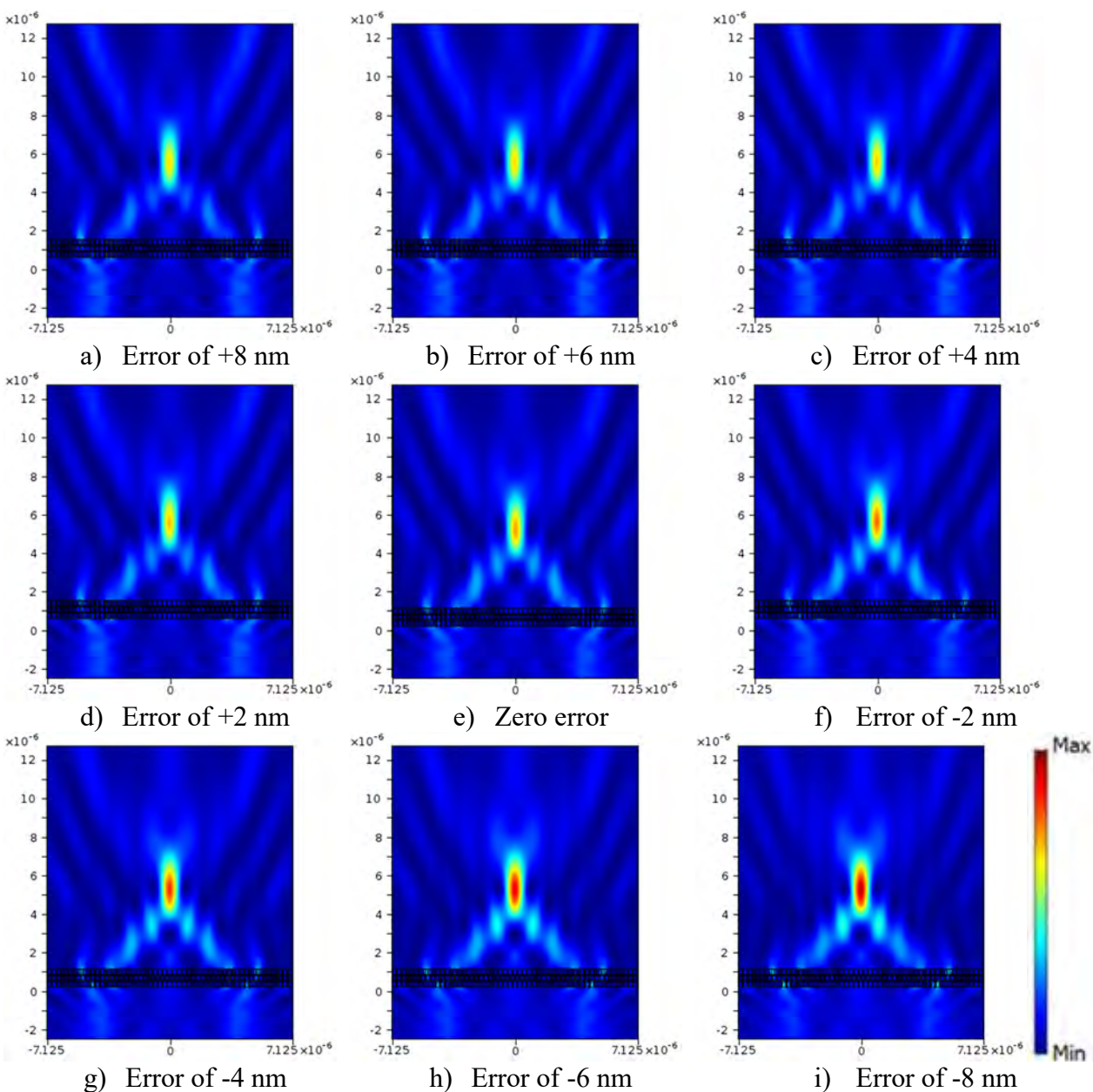


Figure 56 - Influence of varied errors on the metalens for $\lambda_0 = 1.65 \,\mu\text{m}$. The focal plane position, y, in μ m, and the power density of the wave on it, in MW/m², are given in pairs (y, S) as it follows: a) (4.1191; 0.51865) b) (4.0648; 0.52657) c) (4.1253; 0.54076) d) (3.9957; 0.55116) e) (4.0245; 0.57932) f) (4.1857; 0.61725) g) (4.0018; 0.66539) h) (3.9871; 0.71970) i) (4.1187; 0.75978)

Figure 56 shows, in a qualitative form, the power density of the wave reaching its highest intensity in the region of the focal plane. It is considered for wavelength of 1.65 μ m, and the geometry error range in the pair (w_a, w_b) from -8 to 8 nm in steps of 2 nm.

Table 4.6 relates the power density of the EMW to the position of the focal plane of the metalens:

Geometry error, in (nm)	Focal plane position	Power density of the wave (S, in MW/m²)
	(y, in μm)	(3, III WI W/III)
+8	4.1191	0.51865
+6	4.0648	0.52657
+4	4.1253	0.54076
+2	3.9957	0.55116
0	4.0245	0.57932
-2	4.1857	0.61725
-4	4.0018	0.66539
-6	3.9871	0.71970
-8	4.1187	0.75978

Table 4.6 – Focal plane position and power density of the wave related to each geometry error of the metalens, considering $\lambda_0 = 1.65 \, \mu m$.

For $\lambda_0 = 1.65 \,\mu m$, the effects of the geometry errors which are propagated along the structure of the metalens and the power density of the incident wave on the focal plane are shown in Figure 56 and Table 4.6. Figure 56 makes possible to visualize the shifts of the focal plane, while Table 4.6 relates both the focal plane y position and the power density of the wave (on the focal plane) to the applied geometry error over the structure.

Related to the ideal supercell structure (zero error), the error of -2 nm introduces the highest deviation of focal plane position, which shifts up from 4.0245 to 4.1857 μ m, while the lowest focal plane position, 3.9871 μ m, is set by the error of -6 nm.

The power density of the wave has the highest increase, from 0.57932 to 75978 MW/m² when the error varies from 0 to -8 nm. Its highest decrease occurs when the geometry error is +8 nm, which lowers the power density from 0.57932 to 0.51685 MW/m².

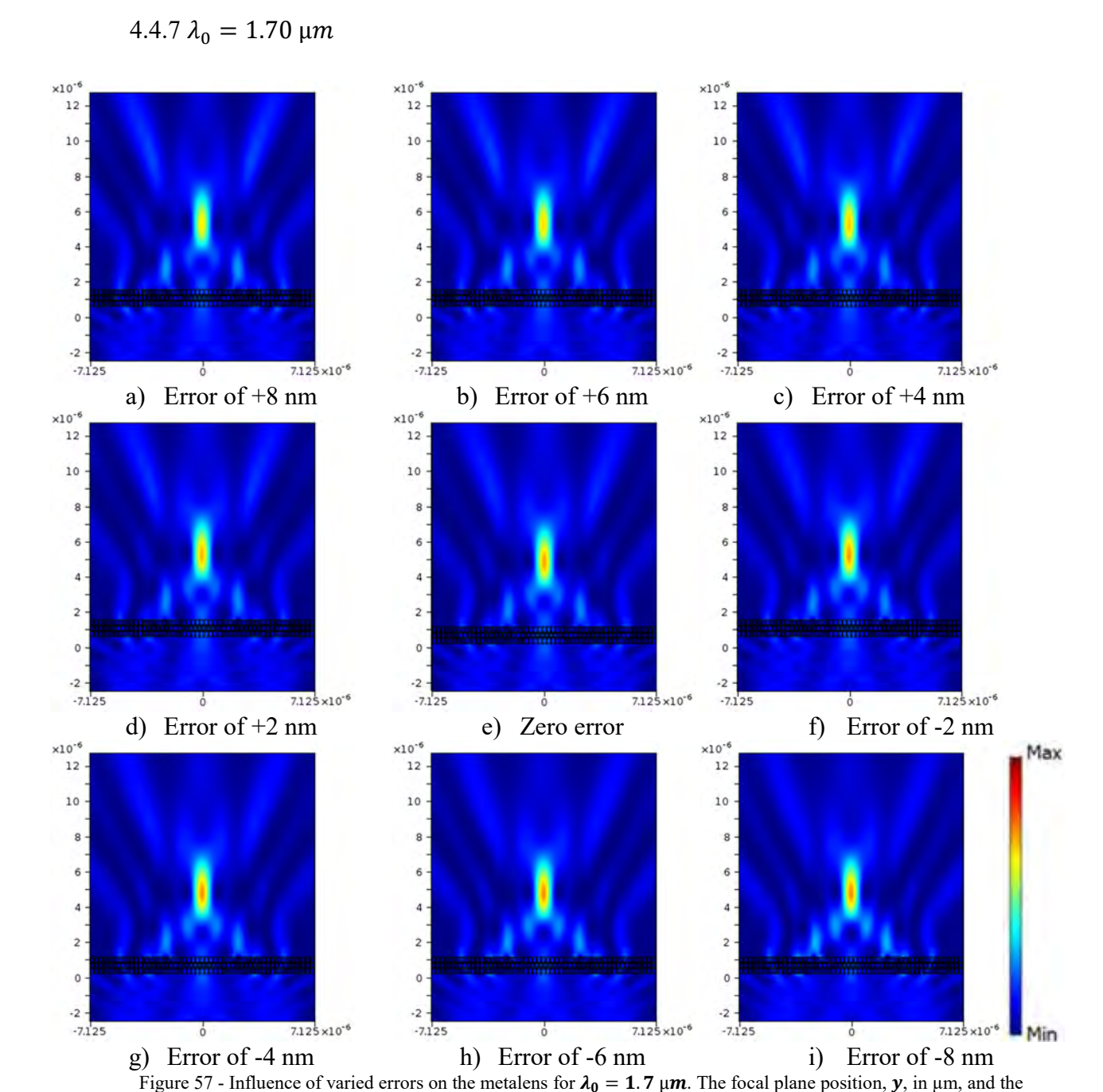


Figure 57 shows, in a qualitative form, the power density of the wave reaching its highest intensity in the region of the focal plane. It is considered for wavelength of 1.7 μ m, and the geometry error range in the pair (w_a, w_b) from -8 to 8 nm in steps of 2 nm.

power density of the wave on it, in MW/m², are given in pairs (y, S) as it follows: a) (3.6582; 0.51538) b) (3.7319; 0.53078) c) (3.7972; 0.56162) d) (3.6728; 0.56162) e) (3.7135; 0.56839) f) (3.7239; 0.57956) g) (3.5647; 0.58527) h) (3.6523; 0.58430) i) (3.6617; 0.59465)

The following Table relates the power density of the EMW to the position of the focal plane of the metalens:

Geometry error, in (nm)	Focal plane position (y,	Power density of the wave
	in μm)	$(S, \text{ in MW/m}^2)$
+8	3.6582	0.51538
+6	3.7319	0.53078
+4	3.7972	0.56162
+2	3.6728	0.56162
0	3.3778	0.56839
-2	3.5241	0.57956
-4	3.5450	0.58527
-6	3.5567	0.58430
-8	3.5567	0.59465

Table 4.7 – Focal plane position and power density of the wave related to each geometry error of the metalens, considering $\lambda_0 = 1.7 \ \mu m$.

For $\lambda_0 = 1.7 \,\mu m$, the effects of the geometry errors which are propagated along the structure of the metalens and the power density of the incident wave on the focal plane are shown in Figure 57 and Table 4.7. Figure 57 makes possible to visualize the shifts of the focal plane, while Table 4.7 relates both the focal plane y position and the power density of the wave (on the focal plane) to the applied geometry error over the structure.

Related to the ideal supercell structure (zero error), the error of +4 nm introduces the highest deviation of focal plane position, which shifts up from 3.3778 to $3.7972~\mu m$, while the lowest focal plane position, $3.3778~\mu m$, is set by the ideal (zero error) supercell geometry.

The power density of the wave has the highest increase, from 0.56839 to 0.59465 MW/m^2 when the error varies from 0 to -8 nm. Its highest decrease occurs when the geometry error is +8 nm, which lowers the power density from 0.56839 to 0.51538 MW/m^2 .

4.4.8 Effect of geometry errors on the square electric field for $\lambda_0 = 1.40 \ \mu m$

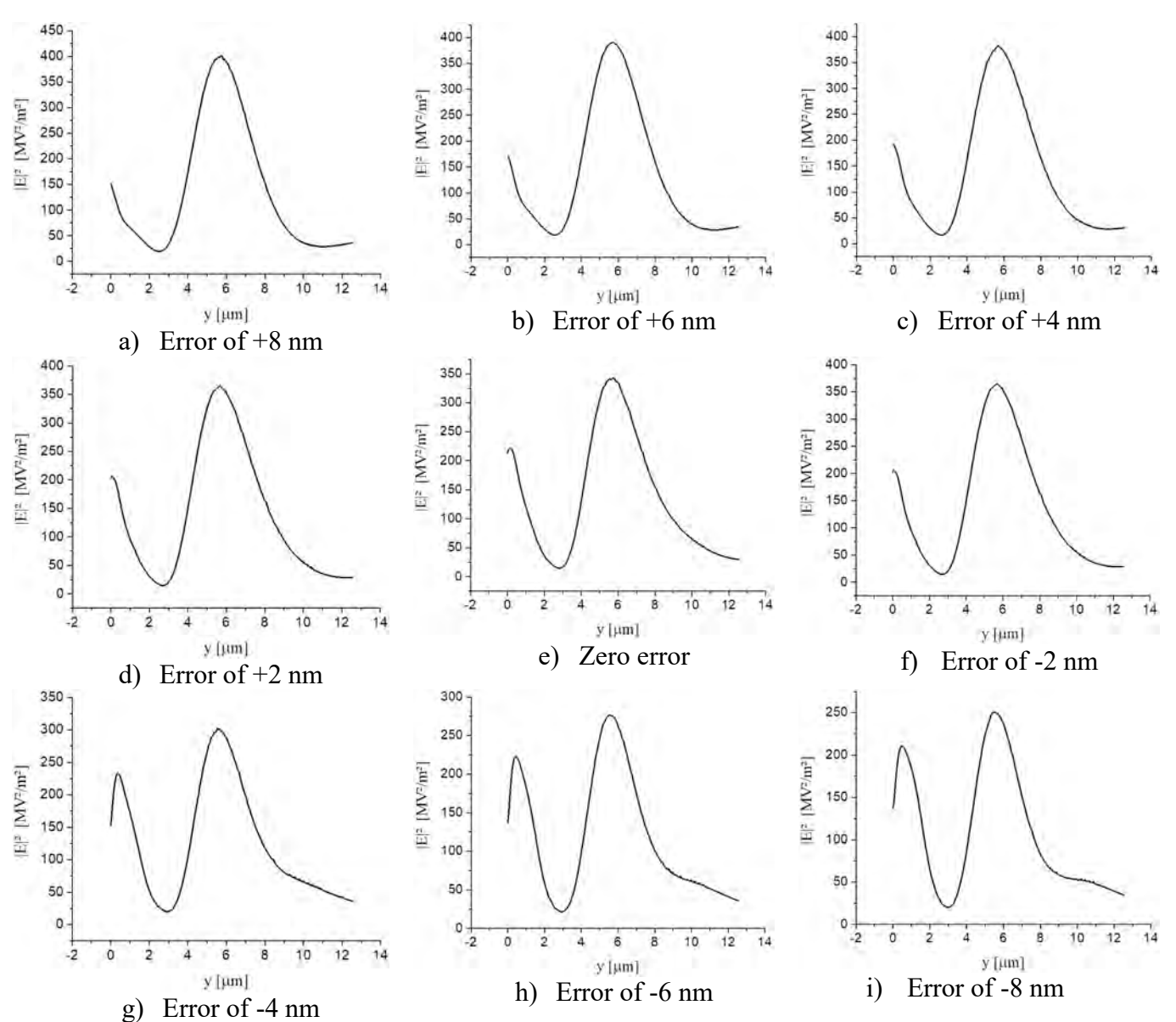


Figure 58 - Influence of varied errors on the metalens for $\lambda_0 = 1.4 \,\mu\text{m}$. The focal plane position, y in μ m, and the square electric field of the wave on it, in MV²/m², are given in pairs (y, E^2) as it follows: a) (5.7584; 401.2516) b) (5.6029; 389.6459) c) (5.6902; 353.8914) d) (5.6662; 365.0699) e) (5.5132; 340.6452) f) (5.4767; 315.3953) g) (5.5450; 302.6883) h) (5.5544; 276.6490) i) (5.4293; 250.3519)

Table 4.8 relates the square electric field of the EMW to the position of the focal plane of the metalens:

Geometry error, in (nm)	Focal plane position (y, in μm)	Square electric field $(E^2$, in MV^2/m^2)
+8	5.7584	401.2516
+6	5.5029	389.6459
+4	5.6902	353.8914
+2	5.6662	365.0699
0	5.5132	340.6452
-2	5.4767	315.3953
-4	5.5450	302.6883
-6	5.5544	276.6490
-8	5.4293	250.3519

Table 4.8 – Focal plane position and square electric field of the wave related to each geometry error of the metalens, considering $\lambda_0 = 1.4 \, \mu m$.

For $\lambda_0 = 1.4 \,\mu m$, the effects of the geometry errors which are propagated along the structure of the metalens and the square electric field of the incident wave on the focal plane are shown in Figure 58 and Table 4.8. Figure 58 makes possible to visualize the shifts of the focal plane, while Table 4.8 relates both the focal plane y position and the square electric field of the wave (on the focal plane) to the applied geometry error over the structure.

Related to the ideal supercell structure (zero error), the error of +8 nm introduces the highest deviation of focal plane position, which shifts up from 5.5132 to 5.7584 μm , while the lowest focal plane position, 5.4293 μm , is set by the error of -8 nm.

The square electric field, E^2 , of the wave has the highest increase, from 340.6452 to 401.2516 MV²/m² when the error varies from 0 to +8 nm. Its highest decrease occurs when the geometry error is -8 nm, which lowers the square electric field from 340.6452 to 250.3519 MV²/m².

4.4.9 Effect of geometry errors on the square electric field for $\lambda_0 = 1.45 \ \mu m$

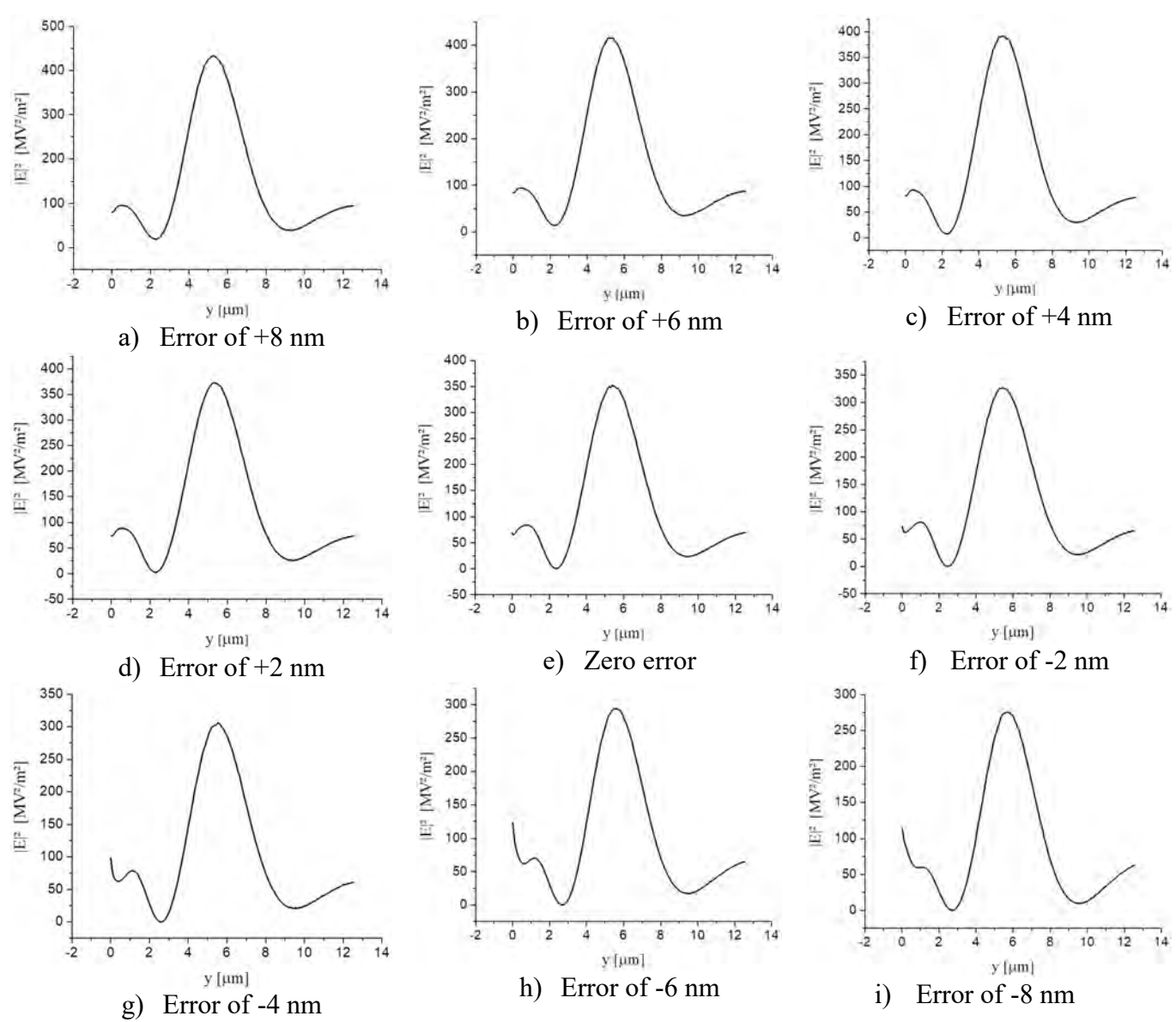


Figure 59 - Influence of varied errors on the metalens for $\lambda_0=1.45~\mu m$. The focal plane position, y in μm , and the square electric field of the wave on it, in MV²/m², are given in pairs (y,E^2) as it follows: a) (5.2210; 432.9392) b) (5.1478; 415.5470) c) (5.6902; 353.8914) d) (5.2235; 371.5872) e) (5.3778; 352.4532) f) (5.2421; 324.6345) g) (5.5450; 306.6178) h) (5.5567; 294.7587) i) (5.5567; 272.2729)

Table 4.9 relates the square electric field of the EMW to the position of the focal plane of the metalens:

Geometry error, in (nm)	Focal plane position (y, in μm)	Square electric field $(E^2$, in MV^2/m^2)
+8	5.2210	432.9392
+6	5.1478	415.5470
+4	5.6902	353.8914
+2	5.2235	371.5872
0	5.3778	352.4532
-2	5.5351	324.6345
-4	5.5450	306.6178
-6	5.5567	294.7587
-8	5.5567	272.2729

Table 4.9 – Focal plane position and square electric field of the wave related to each geometry error of the metalens, considering $\lambda_0 = 1.45 \ \mu m$.

For $\lambda_0 = 1.45 \,\mu m$, the effects of the geometry errors which are propagated along the structure of the metalens and the square electric field of the incident wave on the focal plane are shown in Figure 59 and Table 4.9. Figure 59 makes possible to visualize the shifts of the focal plane, while Table 4.9 relates both the focal plane y position and the square electric field of the wave (on the focal plane) to the applied geometry error over the structure.

Related to the ideal supercell structure (zero error), the error of +4 nm introduces the highest deviation of focal plane position, which shifts up from 5.3778 to $5.6902~\mu m$, while the lowest focal plane position, $5.1478~\mu m$, is set by the error of +6 nm.

The square electric field, E^2 , of the wave has the highest increase, from 352.4532 to 432.9392 MV²/m² when the error varies from 0 to +8 nm. Its highest decrease occurs when the geometry error is -8 nm, which lowers the square electric field from 352.4532 to 279.2729 MV²/m².

4.4.10 Effect of geometry errors on the square electric field for $\lambda_0 = 1.50 \ \mu m$

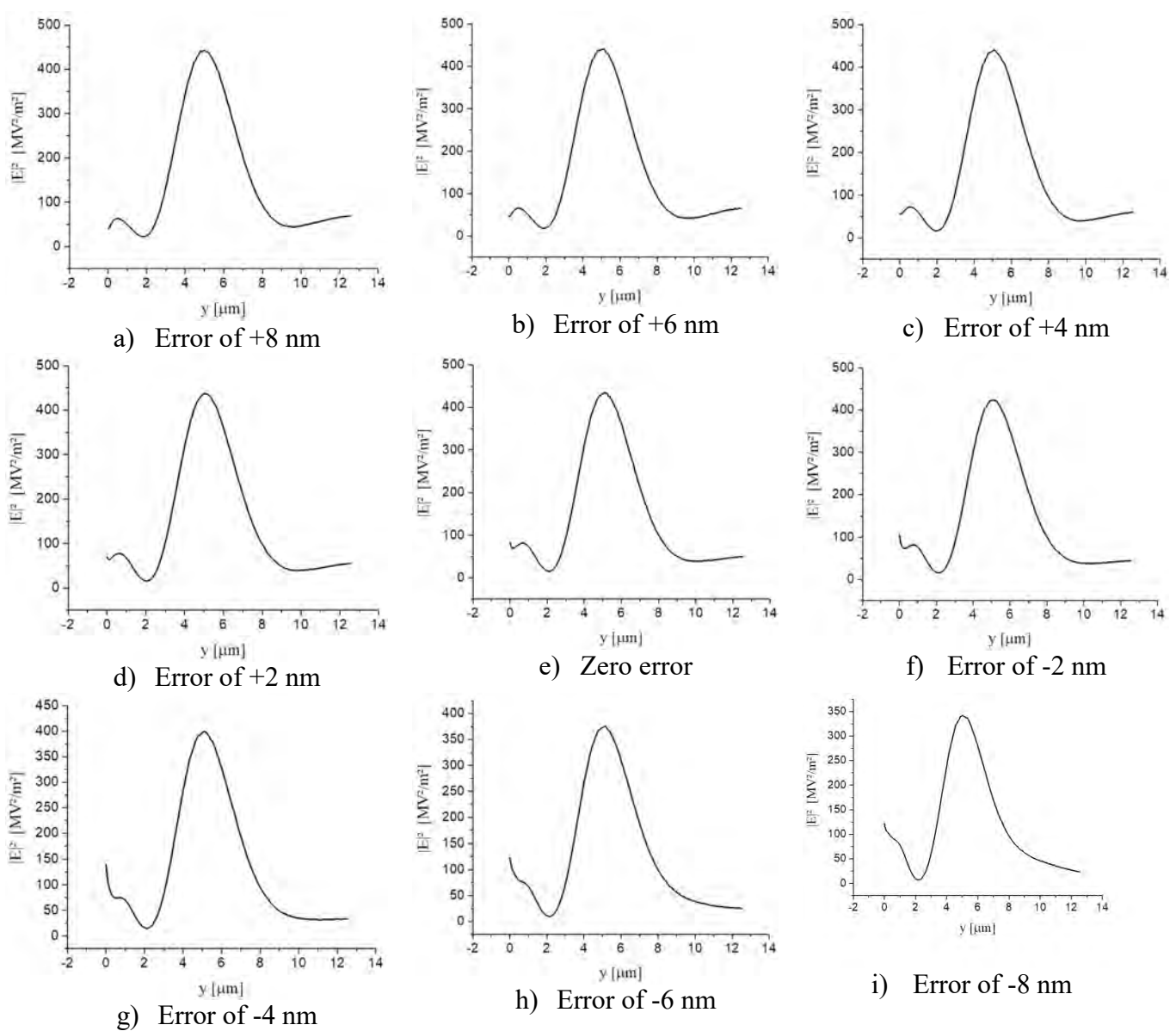


Figure 60 - Influence of varied errors on the metalens for $\lambda_0 = 1.50 \,\mu m$. The focal plane position, y in μm , and the square electric field of the wave on it, in MV²/m², are given in pairs (y, E^2) as it follows: a) (4.7872; 441.1914) b) (4.4892; 412.9054) c) (5.0734; 441.6080) d) (4.9592; 435.7876) e) (5.1144; 432.6700) f) (4.9180; 422.1848) g) (5.0850; 399.3619) h) (5.1741; 376.0848) i) (5.0028; 341.3763)

Table 4.10 relates the square electric field of the EMW to the position of the focal plane of the metalens:

Geometry error, in (nm)	Focal plane position (y, in μm)	Square electric field $(E^2$, in MV^2/m^2)
+8	4.7872	441.1914
+6	4.4892	412.9054
+4	5.0734	441.6080
+2	4.9592	435.7876
0	5.1144	432.6700
-2	4.9180	422.1848
-4	5.0850	399.3619
-6	5.1741	376.0848
-8	5.0028	341.3763

Table 4.10 – Focal plane position and square electric field of the wave related to each geometry error of the metalens, considering $\lambda_0 = 1.50 \ \mu m$.

For $\lambda_0 = 1.5 \,\mu m$, the effects of the geometry errors which are propagated along the structure of the metalens and the square electric field of the incident wave on the focal plane are shown in Figure 60 and Table 4.10. Figure 60 makes possible to visualize the shifts of the focal plane, while Table 4.10 relates both the focal plane y position and the square electric field of the wave (on the focal plane) to the applied geometry error over the structure.

Related to the ideal supercell structure (zero error), the error of -6 nm introduces the highest deviation of focal plane position, which shifts up from 5.1144 to 5.1741 μm , while the lowest focal plane position, 4.4892 μm , is set by the error of +6 nm.

The square electric field, E^2 , of the wave has the highest increase, from 432.6700 to 441.6080 MV²/m² when the error varies from 0 to +4 nm. Its highest decrease occurs when the geometry error is -8 nm, which lowers the square electric field from 432.6700 to 341.3763 MV²/m².

4.4.11 Effect of geometry errors on the square electric field for $\lambda_0 = 1.55 \,\mu m$

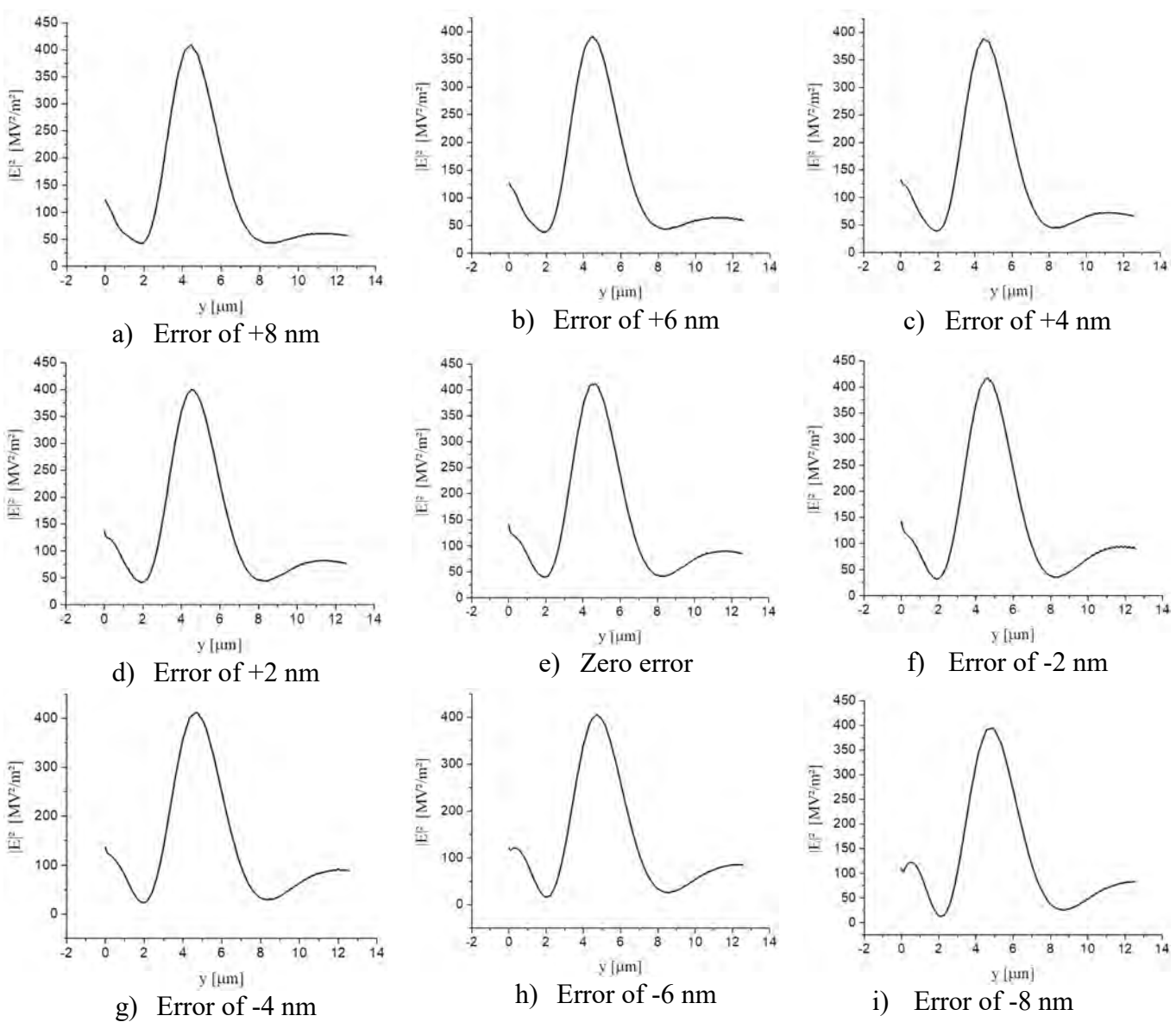


Figure 61 - Influence of varied errors on the metalens for $\lambda_0=1.55~\mu m$. The focal plane position, y in μm , and the square electric field of the wave on it, in MV²/m², are given in pairs (y,E^2) as it follows: a) (4.4481;~408.8204) b) (4.4892;~390.5393) c) (4.4456;~389.1783) d) (4.5300;~399.2400) e) (4.3404;~406.5665) f) (4.6256;~418.2131) g) (4.6594;~411.3966) h) (4.7515;~405.6554) i) (4.5630;~391.0229)

Table 4.11 relates the square electric field of the EMW to the position of the focal plane of the metalens:

Geometry error, in (nm)	Focal plane position (y, in μm)	Square electric field $(E^2$, in MV^2/m^2)
+8	4.4481	402.8204
+6	4.4892	390.5393
+4	4.4456	389.1783
+2	4.5300	399.2400
0	4.3404	406.5665
-2	4.6256	418.2131
-4	4.6594	411.3966
-6	4.7515	405.6554
-8	4.5630	391.0229

Table 4.11 – Focal plane position and square electric field of the wave related to each geometry error of the metalens, considering $\lambda_0 = 1.55 \ \mu m$.

For $\lambda_0 = 155 \,\mu m$, the effects of the geometry errors which are propagated along the structure of the metalens and the square electric field of the incident wave on the focal plane are shown in Figure 61 and Table 4.11. Figure 61 makes possible to visualize the shifts of the focal plane, while Table 4.11 relates both the focal plane y position and the square electric field of the wave (on the focal plane) to the applied geometry error over the structure.

Related to the ideal supercell structure (zero error), the error of -6 nm introduces the highest deviation of focal plane position, which shifts up from 4.3404 to 4.7515 μ m, while the lowest focal plane position, 4.3404 μ m, is set by the ideal (zero error) supercell geometry.

The square electric field, E^2 , of the wave has the highest increase, from 406.5665 to 418.2131 MV²/m² when the error varies from 0 to -2 nm. Its highest decrease occurs when the geometry error is +4 nm, which lowers the square electric field from 406.5665 to 389.1783 MV²/m².

4.4.12 Effect of geometry errors on the square electric field for $\lambda_0 = 1.60 \ \mu m$

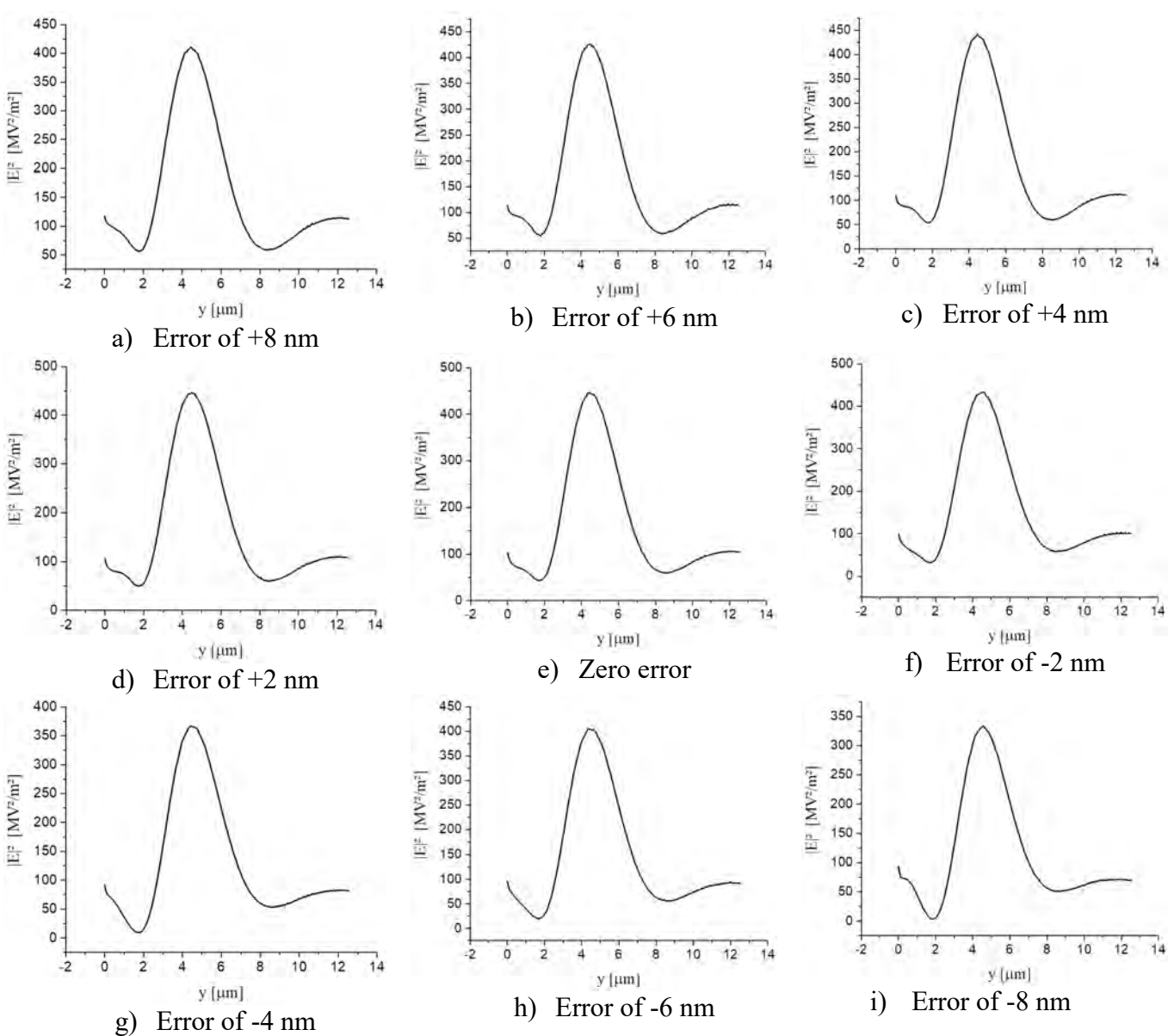


Figure 62 - Influence of varied errors on the metalens for $\lambda_0 = 1.60 \, \mu m$. The focal plane position, y in μm , and the square electric field of the wave on it, in MV²/m², are given in pairs (y, E^2) as it follows: a) (4.4481; 410.9337) b) (4.4892; 426.1810) c) (4.4456; 441.9019) d) (4.3196; 443.5039) e) (4.3404; 445.7053) f) (4.5019; 432.3148) g) (4.3267; 405.0702) h) (4.4219; 366.4733) i) (4.5630; 333.4868)

Table 4.12 relates the square electric field of the EMW to the position of the focal plane of the metalens:

Geometry error, in (nm)	Focal plane position (y, in μm)	Square electric field $(E^2$, in MV^2/m^2)
+8	4.4481	410.9337
+6	4.4892	426.1810
+4	4.4456	441.9019
+2	4.3196	443.5039
0	4.3404	445.7053
-2	4.5019	432.3148
-4	4.3267	405.0702
-6	4.4219	366.4733
-8	4.5630	333.4868

Table 4.12 – Focal plane position and square electric field of the wave related to each geometry error of the metalens, considering $\lambda_0 = 1.60 \ \mu m$.

For $\lambda_0 = 1.6 \,\mu m$, the effects of the geometry errors which are propagated along the structure of the metalens and the square electric field of the incident wave on the focal plane are shown in Figure 62 and Table 4.12. Figure 62 makes possible to visualize the shifts of the focal plane, while Table 4.12 relates both the focal plane y position and the square electric field of the wave (on the focal plane) to the applied geometry error over the structure.

Related to the ideal supercell structure (zero error), the error of -8 nm introduces the highest deviation of focal plane position, which shifts up from 4.3404 to $4.5630\mu m$, while the lowest focal plane position, $4.3196 \mu m$, is set by the error of +2 nm.

The square electric field, E^2 , of the wave has the highest value, of 445.7053 MV^2/m^2 when the structure is ideal (the geometry error is zero). Its highest decrease occurs when the geometry error is +8 nm, which lowers the square electric field from 445.7053 to 333.4868 MV^2/m^2 .

4.4.13 Effect of geometry errors on the square electric field for $\lambda_0 = 1.65 \,\mu m$

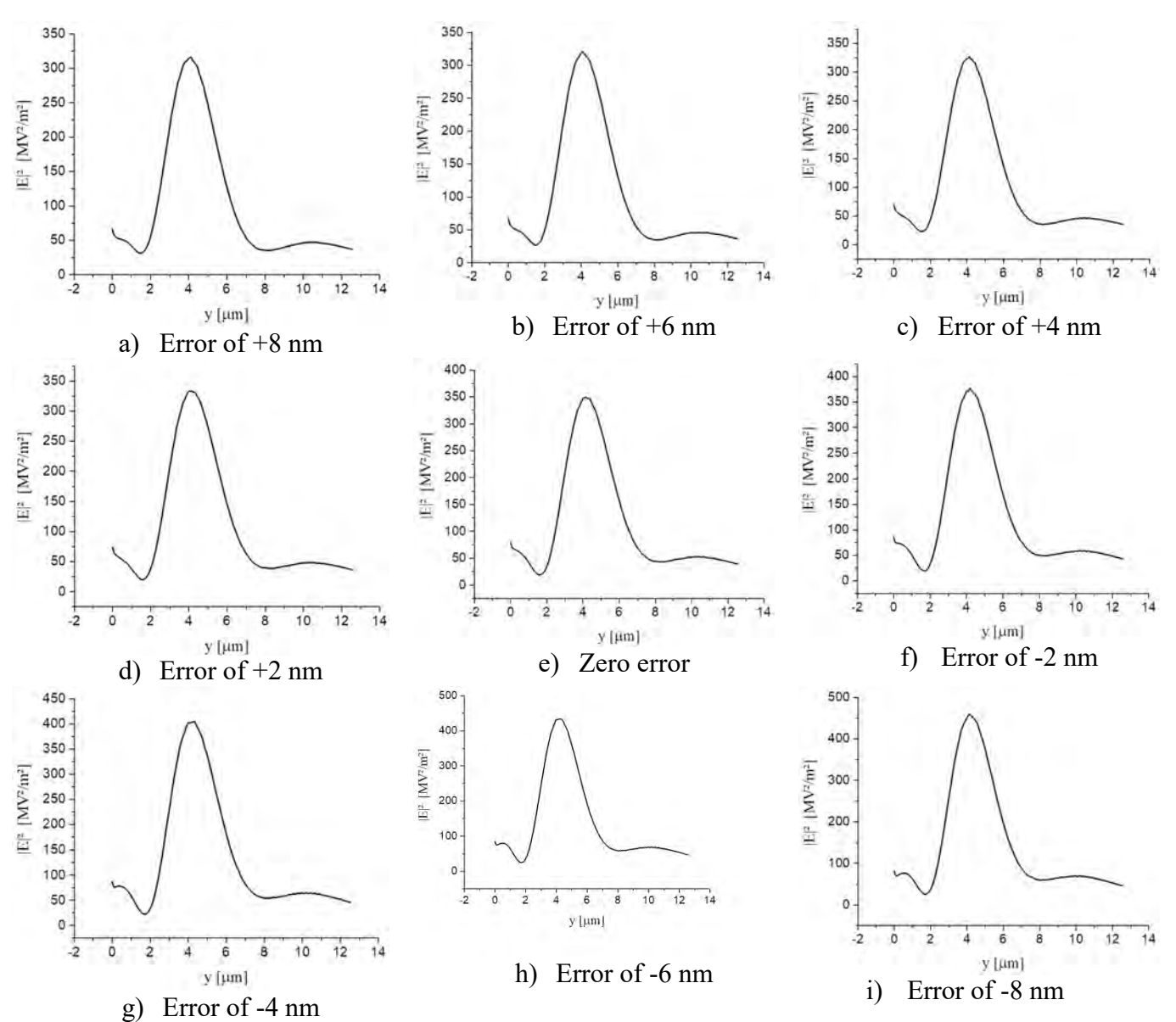


Figure 63 - Influence of varied errors on the metalens for $\lambda_0=1.65~\mu m$. The focal plane position, y in μm , and the square electric field of the wave on it, in MV²/m², are given in pairs (y,E^2) as it follows: a) (4.1191;~315.9577) b) (4.0648;~319.7048) c) (4.1253;~326.2227) d) (3.9957;~332.6175) e) (4.0245;~347.9824) f) (4.1857;~376.2801) g) (4.0018;~401.4145) h) (3.9871;~341.5878) i) (4.1187;~459.3179)

Table 4.13 relates the square electric field of the EMW to the position of the focal plane of the metalens:

Geometry error, in (nm)	Focal plane position (y, in μm)	Square electric field $(E^2$, in MV^2/m^2)
+8	4.1191	315.9577
+6	4.0648	319.7048
+4	4.1253	326.2227
+2	3.9957	332.6175
0	4.0245	347.9824
-2	4.1857	376.2801
-4	4.0018	401.4145
-6	3.9871	348.5878
-8	4.1187	459.3179

Table 4.13 – Focal plane position and square electric field of the wave related to each geometry error of the metalens, considering $\lambda_0 = 1.65 \ \mu m$.

For $\lambda_0 = 1.65 \,\mu m$, the effects of the geometry errors which are propagated along the structure of the metalens and the square electric field of the incident wave on the focal plane are shown in Figure 63 and Table 4.13. Figure 63 makes possible to visualize the shifts of the focal plane, while Table 4.13 relates both the focal plane y position and the square electric field of the wave (on the focal plane) to the applied geometry error over the structure.

Related to the ideal supercell structure (zero error), the error of -2 nm introduces the highest deviation of focal plane position, which shifts up from 4.0245 to 4.1857 μ m, while the lowest focal plane position, 3.9871 μ m, is set by the error of -6 nm.

The square electric field, E^2 , of the wave has the highest increase, from 347.9824 to 459.3179 MV²/m² when the error varies from 0 to -8 nm. Its highest decrease occurs when the geometry error is +8 nm, which lowers the square electric field from 347.9824 to 315.9577 MV²/m².

4.4.14 Effect of geometry errors on the square electric field for $\lambda_0 = 1.70 \ \mu m$

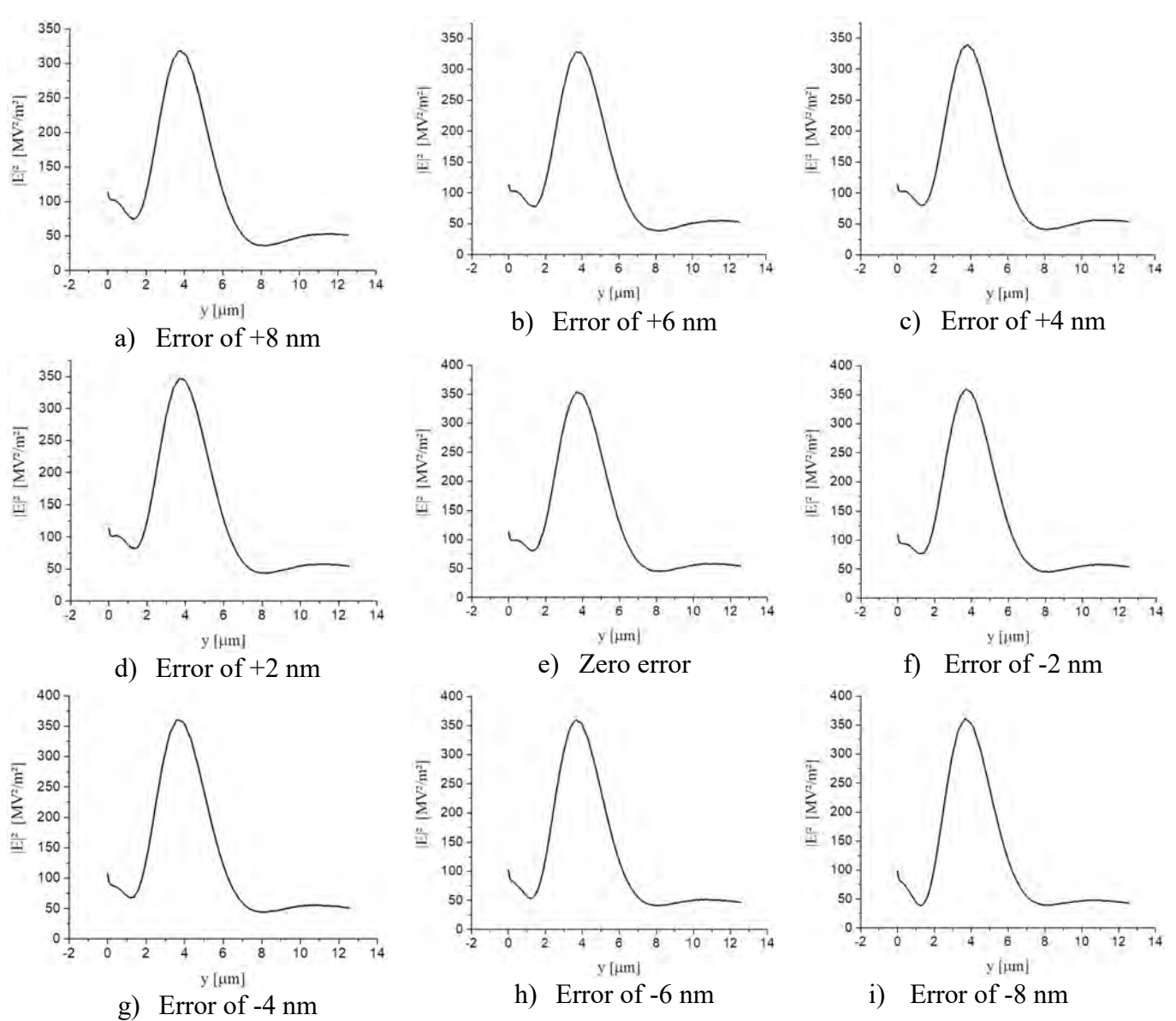


Figure 64 - Influence of varied errors on the metalens for $\lambda_0 = 1.70 \,\mu m$. The focal plane position, y in μm , and the square electric field of the wave on it, in MV²/m², are given in pairs (y, E^2) as it follows: a) (3.6582; 316.3773) b) (3.7319; 327.7093) c) (3.7972; 339.8072) d) (3.6728; 347.0631) e) (3.3778; 337.764) f) (3.5241; 351.5411) g) (3.5450; 359.6580) h) (3.5567; 355.5348) i) (3.5567; 354.9597)

Table 4.14 relates the square electric field of the EMW to the position of the focal plane of the metalens:

Geometry error, in (nm)	Focal plane position (y, in μm)	Square electric field $(E^2$, in MV^2/m^2)
+8	3.6582	316.3773
+6	3.7319	327.7093
+4	3.7972	339.8072
+2	3.6728	347.0631
0	3.3778	337.764
-2	3.5241	351.5411
-4	3.5450	359.6580
-6	3.5567	355.5348
-8	3.5567	354.9597

Table 4.14 – Focal plane position and square electric field of the wave related to each geometry error of the metalens, considering $\lambda_0 = 1.70 \ \mu m$.

For $\lambda_0 = 1.7 \,\mu m$, the effects of the geometry errors which are propagated along the structure of the metalens and the square electric field of the incident wave on the focal plane are shown in Figure 64 and Table 4.14. Figure 64 makes possible to visualize the shifts of the focal plane, while Table 4.14 relates both the focal plane y position and the square electric field of the wave (on the focal plane) to the applied geometry error over the structure.

Related to the ideal supercell structure (zero error), the error of +4 nm introduces the highest deviation of focal plane position, which shifts up from 3.3778 to $3.7972~\mu m$, while the lowest focal plane position, $3.3778~\mu m$, is set by the ideal (zero error) supercell geometry.

The square electric field, E^2 , of the wave has the highest increase, from 337.764 to 359.6580 MV²/m² when the error varies from 0 to -4 nm. Its highest decrease occurs when the geometry error is +8 nm, which lowers the square electric field from 337.764 to 316.3773 MV²/m².

CONCLUSIONS AND FUTURE WORKS

CONCLUSIONS

A literature review about metamaterials and metasurfaces was presented in chapter 2, enlisting the first and the modern applications for these devices. A brief citation of the development of all-dielectric metasurfaces through references from 2007 was pointed. The generalized equations for refraction and reflection, which include the phase profile (or the phase gradient), were discussed. All-dielectric metasurfaces constitute a tendency for substituting plasmonic metasurfaces whenever possible and high efficiency represents a critical demand for certain application.

This work presented three all-dielectric models of metasurfaces based on anomalous refraction and reflection through their generalized equations. The utilized numeric method for the simulations was finite elements to compose the proper mesh within the geometry, considering the devices and their surrounding air boxes. The utilized software was Comsol Multiphysics 5.2. The models presented good attendance to the criteria of global phase control in the range from $-\pi$ to π plus the high absolute value for their respective coefficients.

The developed models, planned for optical infrared wavelength of 1550 nm, utilized ABA type of unit cells, with inner square blocks of varied widths, from 20 to 230 nm, to approximate their practical phase profile to the ideally expected.

The anomalous refractor obtained over 0.9 for the absolute value of the transmission coefficient for the reached transmission angle of 24.17° when $\lambda_0 = 1.55 \,\mu m$. The two highest deviations to this angle (related to the operation wavelength) in increment and decrement, respectively, occurred at $\lambda_0 = 1.7 \,\mu m$, which generated a difference of +2.43°, and at $\lambda_0 = 1.4 \,\mu m$, that yielded an angle of 21.71°, which implies the difference of -2.46°. See section 4.2 for considerations involving the inclusion of geometry errors.

The anomalous reflector presented over 0.94 of absolute value for the reflection coefficient, performing as a perfect mirror for the designed angle of 17.17°. In practice,

it reached an angle of 17.62° without taking in consideration the geometry errors. Furthermore, the highest deviations around the referred practical reflection angle occurred at $\lambda_0 = 1.6 \,\mu m$ and $\lambda_0 = 1.4 \,\mu m$, with the respective increment and decrement of 0.62° and -1.61° . See section 4.3 for considerations involving the inclusion of geometry errors.

The metalens presented satisfactory performance in focusing the electric field, with focal plane expected to be of $3.5\lambda_0$. This means a focal plane in y=5425 nm, while the simulated practical value occurred in y=4550 nm, which means a deviation of approximately 16.1% for the operation wavelength, of $\lambda_0=1.55$ μ m. The highest increment and decrement, respectively, on the position y of the focal plane, related to the practical case (y=4550 nm) occurred at $\lambda_0=1.4$ μ m, of 0.682 μ m, and $\lambda_0=1.7$ μ m, of 0.8365 μ m. See section 4.4 for considerations involving the inclusion of geometry errors.

PURPOSES FOR FUTURE WORKS

- Developing models that employ different dielectric materials with contrasting refractive indexes;
- Simulate the metasurfaces for different geometries, such as circles or ellipses instead of the inner squares;
- Simulations that include not only normal incidence, but a range of incident angles;
- Simulate an all-dielectric power divider metasurface;
- Optimization of the devices with the use of bio-inspired optimization algorithms;

REFERENCES:

- [1] S. Walia, C. M. Shah, P. Gutruf, H. Nili, D. R. ChowdHury, W. Withayachumnankul, M. Bhaskaran, S. Sriram, "Flexible metasurfaces and metamaterials: A review of materials and fabrication processes at micro- and nanoscales", Appl. Phys. Vol. 2 (1), 011303, 2015.
- [2] T. J. Cui, W. X. Tang, X. M. Yang, Z. L. Mei, W. X. Jiang, "Metamaterials: Beyond Crystals, Noncrystals, and Quasicrystals" 1st ed., J. Nanjing, P.R. of China, Ed. CRC Press, 2016.
- [3] S. M. Kamali, E. Arbabi, A. Arbabi and A. Faraon, "A review of dielectric optical metasurfaces for wavefront control", Nanophotonics 7 (6), 1041–1068, 2018.
- [4] J. A. Schuller, R. Zia, T. Taubner, and M. L. Brongersma. "Dielectric metamaterials based on electric and magnetic resonances of silicon carbide particles". Phys. Rev. Lett. **99**, 107401, 2007.
- [5] X. Huang, Y. Lai, Z. H. Hang, H. Zheng, and C. T. Chan. "Dirac cones induced by accidental degeneracy in photonic crystals and zero-refractive-index materials." Nature Mater. 10, 582–586, 2011.
- [6] P. Moitra et al. "Realization of an all-dielectric zero-index optical metamaterial", Nature Photon. 7, 791–795, 2013.
- [7] D. Lin, P. Fan, E. Hasman, and M. L. Brongersma. "Dielectric gradient metasurface optical elements". Science **345** (6194), 298–302, 2014.
- [8] I. Staude, "Active tuning of all-dielectric metasurfaces", Proceedings Volume 11031, Integrated Optics: Design, Devices, Systems, and Applications V; 1103108, 2019.
- [9] A. S. Kupriianov, Y. Xu, A. Sayanskiy, V. Dmitriev, Y. S. Kivshar, and V. R. Tuz, "Metasurface Engineering through Bound States in the Continuum", Phys. Rev. Applied, 12, 014024, 2019.
- [10] S. Gao, C-S. Park, S-S. Lee, and D-Y. Choi, "All-dielectric metasurfaces for simultaneously realizing polarization rotation and wavefront shaping of visible light", Nanoscale, 11, pp. 4083-4090, 2019.
- [11] F. Ding, A. Pors, and S. I. Bozhevolnyi, "Gradient metasurfaces: a review of fundamentals and applications", Rep. Prog. Phys. 81 (2), 026401, 2018.

- [12] S. Chang, X. Guo, X. Ni, "Optical Metasurfaces: Progress and Applications", Annual Review of Materials Research, Vol. 48, pp. 279-302, 2018.
- [13] S. A. Maier (ed.), (World Scientific series in nanoscience and nanotechnology 16)
 -World Scientific Handbook of Metamaterials and Plasmonics in 4 Volumes World Scientific, 2018.
- [14] V. G. Veselago, "The electrodynamics of substances with simultaneously negative values of ε and μ ", Sov. Phys. Usp. **10** pp. 509–514, 1968.
- [15] J. B. Pendry, "Negative Refraction Makes a Perfect Lens", Phys. Rev. Lett. **85** pp. 3966–9, 2000.
- [16] R. A. Shelby, D. R. Smith, and S. Schultz, B "Experimental verification of a negative index of refraction", Science, vol. **292** (5514), pp. 77–79, Apr. 6, 2001.
- [17] Xingcun C. Tong, (Springer Series in Materials Science 262) "Functional metamaterials and metadevices" 1st ed., Springer, 2018.
- [18] Hou-Tong Cheng et al, "A review of metasurfaces: physics and applications", Rep. Prog. Phys. **79**, 076401, 2016.
- [19] N. F. Yu, P. Genevet, M. A. Kats, F. Aieta, J. P. Tetienne, F. Capasso and Z. Gaburro, "Light propagation with phase discontinuities: generalized laws of reflection and refraction" Science **334** (6054), 333–337, 2011.
- [20] F. Ding, Y. Chen, and S. I. Bozhevolnyi, "Metasurface-Based Polarimeters", Appl. Sci. 8, 594, 2018.
- [21] H. He, M. E. J. Friese, N. R. Heckenberg, and H. Rubinsztein-Dunlop, "Direct Observation of Transfer of Angular Momentum to Absorptive Particles from a Laser Beam with a Phase Singularity", Phys. Rev. Lett. 75, 826, 1995.
- [22] G. Gibson et al, "Free-space information transfer using light beams carrying orbital angular momentum", Opt Express 12, 5448, 2004.
- [23] W. D. Callister, D. G. Rethwisch, "Materials Science and Engineering: An Introduction", 9th ed., J. Nanjing, P.R. of China, Ed. Wiley, 2013.
- [24] S. O'Brien and J. B. Pendry, "Photonic band-gap effects and magnetic activity in dielectric composites", Journal of Physics: Condensed Matter **14** 4035 ISSN 0953-8984, 2002.
- [25] R. A. Vieira, T. F. S. de Castro, and V. F. Rodriguez-Esquerre, "Anomalous refraction of infrared waves through ultrathin all dielectric metasurfaces". SPIE 2017,

- Metamaterials, Metadevices, and Metasystems 2017, San Diego. Metamaterials, Metadevices, and Metasystems 2017, p. 118.
- [26] R. A. Vieira, T. F. S. de Castro, and V. F. Rodriguez-Esquerre, "Refração Anômala em Metasuperficies Totalmente Dielétricas", Encontro Anual do Iecom em Comunicações, Redes e Criptografia, São Luís/MA, p. 27-28, 2017.
- [27] T. F. Simões de Castro, R. A. Vieira, and V. F. Rodriguez-Esquerre, "*Ultrathin all-dielectric Metasurface for Infrared Waves Focusing*", Latin America Optics and Photonics Conference, Lima, p. Th2A.2, 2018.
- [28] F. Monticone, N. M. Estakhri and A. Alù, "Full control of nanoscale optical transmission with a composite metascreen", Phys. Rev. Lett., vol. 110, no. 20, 203903, May 2013.
- [29] J. Cheng, S. Inampudi and H. Mosallaei, "Optimization-based Dielectric Metasurfaces for Angle-Selective Multifunctional Beam Deflection". Scientific Reports 7, sep. 2017.
- [30] B. Slovick, Z. G. Yu, M. Berding, and S. Krishnamurthy, "Perfect dielectric-metamaterial reflector", Phys. Rev. B, vol. 88, issue 16, 165114, oct. 2013.
- [31] P. Moitra, B. A. Slovick, Z. G. Yu, and S. Krishnamurthy, and J. Valentine, "Experimental demonstration of a broadband all-dielectric metamaterial perfect reflector", Appl. Phys. Lett. **104**, 171102, 2014.
- [32] P. Moritra, B. A. Slovick, W. Li, I. Kravchencko, D. P. Briggs, S. Krishnamurthy, and J. Valentine, "Large-scale all-dielectric metamaterial perfect reflectors", ACS Photon. 2, 692–698, 2015.
- [33] Q. Zhang, C. Liu, G. Gan and X. Cui", "Visible perfect reflectors realized with all-dielectric metasurface", Optics Communications Vol. **402** (1), pp. 226-230, 1 Nov. 2017.
- [34] Y. Huang, H. Xu, Y. Lu, and Y. Chen, "All-Dielectric Metasurface for Achieving Perfect Reflection at Visible Wavelengths", J. Phys. Chem. C, 122, 2990–2996, 2018.
- [35] A. S. Schwanecke, V. A. Fedotov, V. V. Khardikov, S. L. Prosvirnin, Y. Chen, N. I. Zheludev, "Optical magnetic mirrors", J. Opt. A Pure Appl. Opt. 9, L1–L2, Nov. 2006.

- [36] S. Liu, M. B. Sinclair, T. S. Mahony, Y. C. Jun, S. Campione, J. Ginn, D. A. Bender, J. R. Wendt, J. F. Ihlefeld, P. G. Clem, J. B. Wright, and I. Brener, "Optical magnetic mirrors without metals", Optica 1(4), 250, 2014.
- [37] Z. Ma, S. M. Hanham, P. Albella, B. Ng, H. T. Lu, Y. Gong, S. A. Maier, and M. Hong, "*Terahertz All-Dielectric Magnetic Mirror Metasurfaces*", ACS Photonics **3**, pp. 1010–1018, 2016.
- [38] T. Shibanuma, S. A. Maier and P. Albella, "Polarization control of high transmission/reflection switching by all-dielectric metasurfaces", Appl. Phys. Lett. 112, 063103, 2018.
- [39] A. Karvounis, B. Gholipour, K. F. MacDonald and N. I. Zheludev, "*All-dielectric phase-change reconfigurable metasurface*", Appl. Phys. Lett. **109**, 051103, Aug.2016.
- [40] M. Khorasaninejad and F. Capasso, "Metalenses: Versatile multifunctional photonic components," Science **358** (6367), eaam8100, 2017.
- [41] P. R. West, J. L. Stewart, A. V. Kildishev, V. M. Shalaev, V. V. Shkunov, F. Strohkendl, Y. A. Zakharenkov, R. K. Dodds, and R. Byren, "All-dielectric subwavelength metasurface focusing lens", Opt. Express 22, pp. 26212–26221, 2014.
- [42] Y. Shen and X. Luo, "Efficient bending and focusing of light beam with all-dielectric subwavelength structures", Opt. Commun. **366** pp. 174–178, 2016.
- [43] A. Arbabi, R. M. Briggs, Y. Horie, M. Bagheri, and A. Faraon, "Efficient dielectric metasurface collimating lenses for mid-infrared quantum cascade lasers.", Opt Express, Vol. 23 (26), pp. 33310–33317, Dec. 2015.
- [44] A. Y. Zhu et al., "Ultra-compact visible chiral spectrometer with meta-lenses", APL Photonics 2, 036103 (2017).
- [45] E. Arbabi, A. Arbabi, S. M. Kamali, Y. Horie, and A. Faraon, "Multiwavelength polarization-insensitive lenses based on dielectric metasurfaces with meta-molecules", Optica vol. 3, issue 6, pp. 628-633, 2016.
- [46] A. Dourado-Sisnando, V. F. Rodriguez-Esquerre, C. E. Rubio-Mercedes, L. da F. Vieira, and I. M. T. Ruffini, "Power Coupling Optimization in 2D Waveguides by Evolutionary Algorithms", Photonics Technology Letters IEEE, vol. 27, no. 14, pp. 1561-1564, Jul. 2015.
- [47] G. C. Marques, Tema 06 Formulações da Óptica Geométrica | Aula 04 Princípio de Fermat (2016), (available at https://www.youtube.com/watch?v=lPwTDn 3TCk).
- [48] F. A. Jenkins, H. E. White, "Fundamentals of Optics", 4th ed., McGraw-Hill, pp. 10-11, 1976.
- [49] H. Sayginel, Introduction to Fermat's Principle and mathematical derivation of the Snell's Law (2018), (available at https://www.youtube.com/watch?v=bItZbUxrgww).

APPENDIX

APPENDIX A – PUBLICATIONS OF ACADEMIC PAPERS

A.1 ACADEMIC PAPERS RELATED TO THE PROJECT

The research done in this dissertation work made possible the publication in international congresses.

A.1.1 PUBLICATION IN INTERNATIONAL CONGRESS

• SPIE 2017 (San Diego, USA)
Title of the periodic: Anomalous refraction of infrared waves through ultrathin all dielectric metasurfaces.

Authors: Rafael Andrade Vieira*, Tulio Freitas Simões de Castro*, Vitaly Felix Rodriguez-Esquerre*.

- * Universidade Federal da Bahia (UFBA).
- ENCOM 2017 (São Luís/MA, Brasil)
 Title of the periodic: Refração Anômala em Metasuperfícies Totalmente Dielétricas.

Authors: Rafael Andrade Vieira*, Tulio Freitas Simões de Castro*, Vitaly Felix Rodriguez-Esquerre*.

* Universidade Federal da Bahia (UFBA).

• LAOP 2018 (Lima, Peru)
Title of the periodic: Ultrathin all-dielectric Metasurface for Infrared Waves Focusing.

Authors: Tulio Freitas Simões de Castro*, Rafael Andrade Vieira*, Vitaly Felix Rodriguez-Esquerre*.

* Universidade Federal da Bahia (UFBA).

APPENDIX

APPENDIX B – FERMAT'S PRINCIPLE AND THE CLASSIC LAWS OF REFRACTION AND REFLECTION

B1 CONSEQUENCE OF FERMAT'S PRINCIPLE WHEN THE LIGHT IS MOVING THROUGH THE SAME MEDIA [47]

Given two points in the XY plane, A and B, the possibilities of ways between both are infinite, at first, as the Figure B1 suggests:

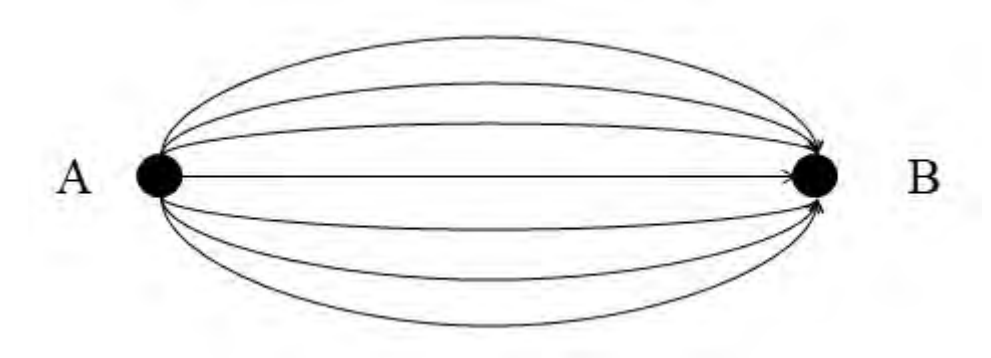


Figure B1 – Example of many of infinite paths that the light can travel between two points A and B.

Fermat's principle states that the light travels from point A to point B in such way that it takes the smallest possible time to do so. As it remains moving through the same media, the path between two points corresponds to a straight line that crosses both points. When light crosses different media, however, it goes through a straight line while in the first media until it reaches the interface between the two media, where it is bended in two ways: partially reflected back to the first media and part of it is transmitted to the second media through another straight light, where the path is such that the travel time is as smallest as possible, which will be discussed as it follows.

Let the velocity, in the XY plane, be given by $v = \frac{ds}{dt}$, where ds is the incremental change of the displacement with respect to the time t. That considered, the derivative of time can be written as:

$$dt = \frac{ds}{v} \tag{B1}$$

Where:

$$ds = \sqrt{x^2 + y^2} \tag{B2}$$

If the displacement is relative to the wavelength, λ , then:

$$\frac{ds}{d\lambda} = \sqrt{\left(\frac{dx}{d\lambda}\right)^2 + \left(\frac{dy}{d\lambda}\right)^2} d\lambda \tag{B3}$$

Considering v = c/n, where c is the speed of light in free space and n = n(x, y) is the refractive index of the media, which changes with each point of the path, it yields:

$$dt = \frac{ds}{v} = \frac{ds}{c/n} \tag{B4}$$

$$dt = -\frac{n}{c}ds \tag{B5}$$

Starting from this formulation of equation B5, it is possible to sum the displacements that the light suffers by integrating the referred equation, which yields:

$$\int dt = \int \frac{n}{c} ds \tag{B6}$$

Since c is a constant term, it can stand behind the integral. Now, considering the points A and B which the light passes through implies to consider that the integration limits on the left side as t_A and t_B , while limits on the right side of equation B6 will be λ_A and λ_B , for the displacement s is function of the wavelength λ , and then the referred equation becomes:

$$\int_{t_A}^{t_B} dx = \frac{1}{c} \int_{\lambda_A}^{\lambda_B} n \cdot ds \tag{B7}$$

The n.ds term inside the integral on the right side of equation B7 is the called **Optical Path Length** (OPL) [48], which is stated, by Fermat's principle, to be the minimum between two points. It is noticeable that, considering one same media to contain the points A and B, the value of n is constant, and can be taken as constant, n_o in this discussion, which makes equation 7 become as follows:

$$t_B - t_A = \frac{n_o}{c} \int_{\lambda_A}^{\lambda_B} ds \tag{B8}$$

For the particular case when the light traverses one single media, the refractive index is constant. This means that the minimum Optical Path Length is directly associated with the minimum displacement s, a straight line, according to equation B8, in its turn related to the minimum time. That satisfies the Fermat's principle for this case.

B2 FERMAT'S PRINCIPLE ON THE CLASSIC REFLECTION OF LIGHT

Let A be a point [49] through which passes an incident electromagnetic radiation until it reaches the point P of a perfect mirror, initially unknown, and leaves it reflected in direction of the point B, according to Figure B2:

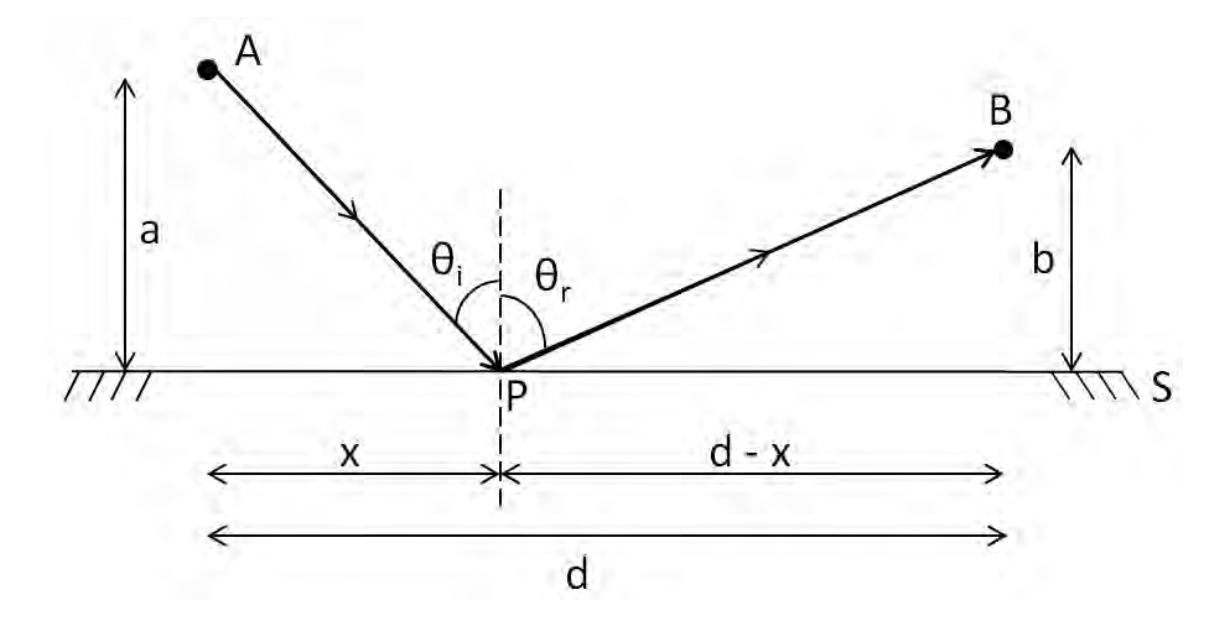


Figure B2 – Generic example of classic reflection of a light beam.

From Figure B2, the points A and B have a horizontal distance d from each other. The horizontal distance of from point A to point P is given by x, while that of P to point B is (d-x). The vertical distance from point A to the mirror is given by a, while from point B to the mirror is b. The incident light makes an angle of θ_i with the axis that is normal to the mirror, while the reflected light makes an angle of θ_r with respect to the same axis. The path taken by the light from the point A to the point B is given by Δz , which is the sum of the individual straight segments AP and PB.

Reflected light keeps propagating within the same media from which it came from, implying that, when reflected, the light remains with the same constant speed of when it was coinciding directed to the mirror, that is:

$$v = \frac{\Delta z}{\Delta t} \tag{B9}$$

Where:

$$\Delta z = \overline{AP} + \overline{PB} \tag{B10}$$

A careful look at equation B10 and Figure B2 as a triangle allows one to observe that:

$$\Delta z = \sqrt{x^2 + a^2} + \sqrt{(d - x)^2 + b^2}$$
 (B11)

Returning to Fermat's principle, the point P will be located on a horizontal distance x from point A, such that the time that the light takes to pass through point B is minimal. It is, then, formed a minimization problem of the interval Δt taken by the light between the referred points A and B. If, in equation B9, the Δz term is substituted by the one of equation B11 and the result is solved for Δt , then it yields:

$$\frac{\Delta z}{\Delta t} = \frac{\sqrt{x^2 + a^2} + \sqrt{(d - x)^2 + b^2}}{\Delta t}$$
 (B12)

$$\Delta t = \frac{\sqrt{x^2 + a^2} + \sqrt{(d - x)^2 + b^2}}{v}$$
 (B13)

Equation B13 has the distance x as the only variable. The problem of minimizing Δt is solved, then, by differentiating equation B13 with respect to x and making it equal to zero, according to the following steps:

$$\frac{d(\Delta t)}{dx} = \frac{1}{v} \left\{ \frac{1}{2} (x^2 + a^2)^{-1/2} \cdot 2x + \frac{1}{2} [(d - x)^2 + b^2]^{-\frac{1}{2}} \cdot 2 \cdot (d - x) \cdot (-1) \right\}$$
 (B14)

Equation B14 is, then, equalized to zero in order to minimize the travel time, which can be significantly simplified as it follows:

$$\frac{x}{\sqrt{x^2 + a^2}} - \frac{d - x}{\sqrt{(d - x)^2 + b^2}} = 0$$
(B15)

By comparing Figure B2 with equation B15, one can notice that the first term corresponds to $\sin(\theta_i)$, while the second term of the left side coincides with $\sin(\theta_r)$. Substituting equation B15 by its corresponding sinusoidal terms, it yields:

$$\sin(\theta_i) - \sin(\theta_r) = 0 \tag{B16}$$

$$\sin(\theta_i) = \sin(\theta_r) \tag{B17}$$

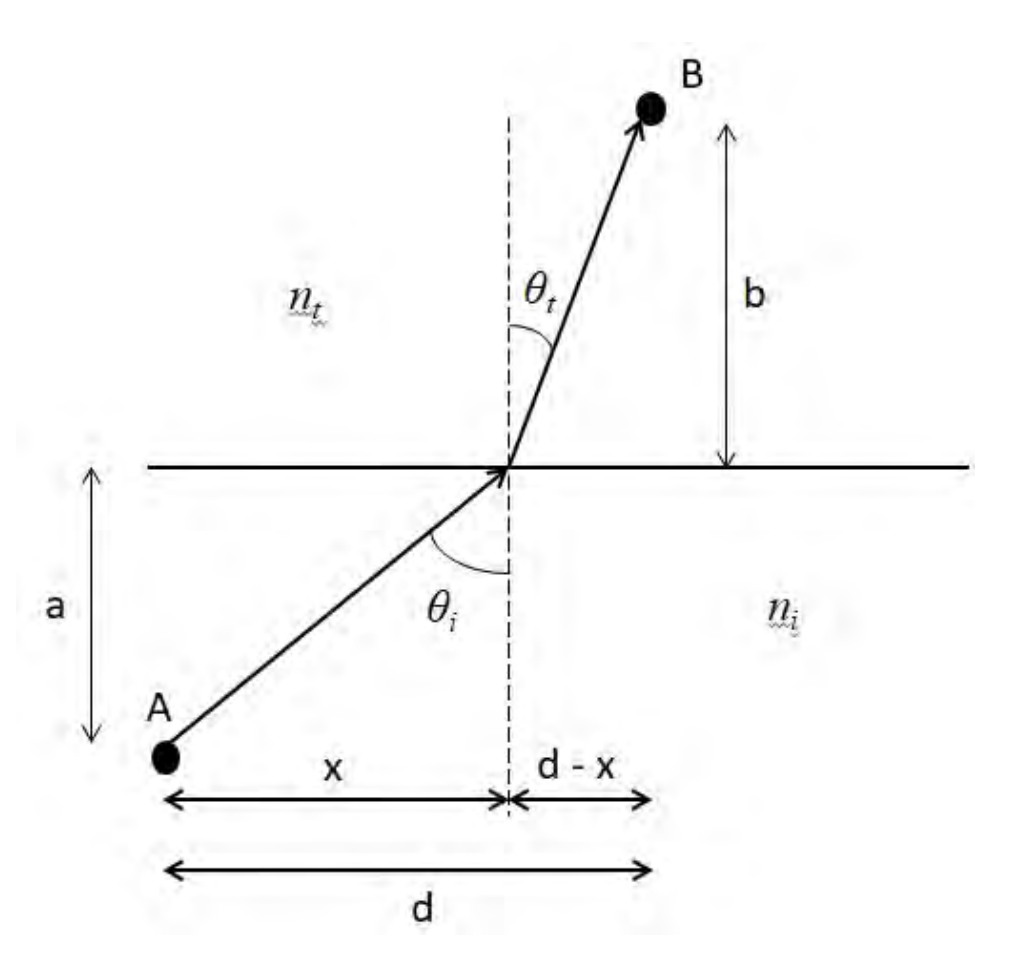
The necessary condition to both sinusoidal terms of equation B17 be equal is that the arguments on both sides is the same, then:

$$\theta_i = \theta_r \tag{B18}$$

The conclusion of applying Fermat's principle to the classic law of reflection is in equation B18, which shows that the angle of incidence must be equal to the angle of reflection of the light.

B3 FERMAT'S PRINCIPLE APPLIED TO THE CLASSIC REFRACTION OF LIGHT

The "principle of least time" can also be applied to derive the classic Snell's Law [49]. This will be explained based on Figure B3, where light travels from one media to another, and considering $n_t > n_i$.



 $Figure \ B3-Generic\ example\ of\ classic\ refraction\ of\ a\ light\ beam.$

Consider a beam of light traversing from point A to point B, which horizontal distance is d. An horizontal line determines an interface between media 1 (which refractive index is n_i) and media 2 (which refractive index is n_r). x is the horizontal distance between the point A and the perpendicular line where the light crosses from one media to another. It can be observed, then, that the distance between the dashed and the point B is given by (d - x). Same as it was for section B2, θ_i is the angle that the beam makes with the imaginary axis that is normal to the mirror, while the transmitted light makes an angle of θ_t with respect to the same axis. Just as in section B2, the vertical distance from point A to the interface is given by a, while the vertical distance from point B to the interface is given by b.

The time taken for the light to leave point A and hit the interface will be given by t_A , while the time taken from the interface to point B will be considered to be t_B . Classic Snell's law can be obtained, as it follows, by calculating both different trajectories show in Figure B3, each time and then, according to Fermat's principle, minimizing the obtained times t_A and t_B .

By observing Figure B3, one can comprehend, through basic geometry, that the respective propagation paths \overline{AP} and \overline{PB} , from the starting point A to point P of the interface and then from point P to the destination point B, are given by:

The propagation time of light through paths \overline{AP} and \overline{PB} are given, respectively, by $t_{\overline{AP}} = \overline{AP} / v_i$ and $t_{\overline{PB}} \overline{PB} / v_t$, which yields:

$$\overline{AP} = \sqrt{x^2 + a^2} \tag{B19}$$

$$\overline{PB} = \sqrt{(d-x)^2 + b^2} \tag{B20}$$

$$t_{\overline{AP}} = \frac{\sqrt{x^2 + a^2}}{v_i} \tag{B21}$$

$$t_{\overline{PB}} = \frac{\sqrt{(d-x)^2 + b^2}}{v_t} \tag{B22}$$

The total time is given by adding both equation 21 and equation 22:

$$t_{Total} = \frac{\sqrt{x^2 + a^2}}{v_i} + \frac{\sqrt{(d - x)^2 + b^2}}{v_t}$$
 (B23)

Since Fermat's principle is about the minimum propagation time, it is fit for this application application to assume that:

$$\frac{dt}{dx} = \frac{2x}{2v_i\sqrt{x^2 + a^2}} - \frac{2x}{2v_t\sqrt{(d-x)^2 + b^2}}$$
 (B24)

The minimization process requires that equation B24 is equal to zero and by observing the triangles of Figure B3, it yields:

$$\frac{1}{v_i} \frac{x}{\sqrt{x^2 + a^2}} - \frac{1}{v_i} \frac{x}{\sqrt{(d - x)^2 + b^2}} = 0$$
 (B25)

$$\frac{1}{v_i} \frac{x}{\sqrt{x^2 + a^2}} = \frac{1}{v_i} \frac{x}{\sqrt{(d - x)^2 + b^2}}$$
 (B26)

One can compare equation 25 with Figure B3 and carefully observe the sinusoidal relations:

$$\sin \theta_i = \frac{x}{\sqrt{x^2 + a^2}} \tag{B27}$$

$$\sin \theta_t = \frac{x}{\sqrt{(d-x)^2 + b^2}} \tag{B28}$$

Substituting in equation B26 the results obtained from equation B27 and equation B28, then it becomes:

$$\frac{\sin \theta_i}{v_i} = \frac{\sin \theta_t}{v_t} \tag{B29}$$

Since the refractive index is defined as n = c/v, the velocities which light will propagate over the two homogeneous media can be given in terms of the refractive index as it follows:

$$\frac{\sin \theta_i}{\frac{\epsilon}{n_i}} = \frac{\sin \theta_t}{\frac{\epsilon}{n_t}} \tag{B30}$$

Finally, by manipulating equation B30, Snell's classic law is, then, appropriately obtained:

$$n_i \sin \theta_i = n_t \sin \theta_t \tag{B31}$$